Galaxies and their environment

Ankit Singh

A thesis submitted for the partial fulfillment of

the degree of Doctor of Philosophy

Department of Physical Sciences,

Indian Institute of Science Education and Research Mohali

Knowledge city, Sector 81, SAS Nagar, Manauli PO, Mohali 140306,Punjab, India.

March, 2020

Dedication

This thesis is dedicated to my parents Ms. Lila Singh and Mr. Ravinder Singh. They could not earn any degree but raised two sons who went on to pursue a doctoral degree. Their sacrifices and love has helped maintain my motivation and quest for knowledge.

I dedicate this thesis to my elder brother Dr. Amit Singh for guiding me throughout my career. His experience and advice has always helped me in making the right decisions.

This work is dedicated to all my mentors and teachers who have taught and guided me throughout my education.

Declaration

The work presented in this thesis has been carried out by me under the guidance of Prof. Jasjeet Singh Bagla at the Indian Institute of Science Education and Research Mohali. This work has not been submitted in part or in full for a degree, a diploma, or a fellowship to any other university or institute. Whenever contributions of others are involved, every effort is made to indicate this clearly, with due acknowledgment of collaborative research and discussions. This thesis is a bonafide record of original work done by me and all sources listed within have been detailed in the bibliography.

Ankit Singh

In my capacity as the supervisor of the candidate's thesis work, I certify that the above statements by the candidate are true to the best of my knowledge.

Prof. Jasjeet Singh Bagla

Acknowledgment

I want to thank and express my sincere gratitude to my thesis supervisor, Prof. Jasjeet Singh Bagla. The thing I admire most about him is the freedom he gives one as a researcher to collaborate with others and explore ideas on your own. He has given me full support in whatever decisions I have made professionally. It is often possible in research to be overwhelmed by codes, algorithms and analysis, but he has taught me not to stop thinking about the physics of the problem in hand. He has taught me how to shape an idea into an interesting problem and pursue it as a research project.

I thank Dr. Smriti Mahajan for her guidance and support. She is not my supervisor technically, but she has not been anything less than a supervisor. She is amazing and is an inspiration for a young researcher like me. She is a hard-working collaborator and always pushes you to go that extra mile to make your work stand out. I am more thankful to her for being so friendly and listening to every stupid idea that I have thrown her way with the same zeal. She has taught me not to hesitate from asking hard questions in your research. I have learnt a lot from her personally and professionally.

I would also like to thank my doctoral committee, Dr. Abhishek Chaudhuri and Dr. Harvinder Kaur Jassal, for supporting my entire time in IISER Mohali. I thank Dr. Chaudhuri for teaching me fluid mechanics, and his constant feedback on my research approach enabled me to strive for explaining my research in comprehensive simplest form. I thank Dr. Jassal for her suggestions on my presentations and her insights in my research. I express my gratitude towards Dr. Jaokim Rosdahl from CRAL, France, for teaching me how to run a hydrodynamical simulation. He was kind enough to sit with me for hours during a conference and discuss my project. He is a very helpful, humble and selfless researcher who has provided me with his insights on the project. I thank Dr. Mamta Gulati for her help and guidance in one of the projects. I want to thank Prof. K.P. Singh for his encouragement and support during my interactions with him. I want to thank Dr. Dipanjan Charaborty and Dr. Satyajit Jena for their help and motivation during my interactions with them. I would like to thank my senior in the astrophysics group, Dr. Sandeep Rana, for his support, encouragement and help with python. I acknowledge the assistance and discussions from some of the past and present members of the astrophysics group: Dr. Kinjalk, Dr. Aru Beri, Ranbir, Ashish, Manvendra, Swati, Juhi and Prashansa.

I acknowledge the funding support I have received from IISER Mohali for carrying out my research. I acknowledge the International Astronomical Union (IAU) for giving me travel support for attending a conference at Osaka University, Japan. I acknowledge the travel support I received from the University of New South Wales (UNSW) and Legacy Survey of Space and Time (LSST) corporation for a conference in UNSW, Sydney. The work I have done in this period is computationally intensive, and I thank Ms. Garima, Mr. Sunny and computational facilities at IISER Mohali for providing me constant help during my research. I would like to acknowledge Inter University Center for Astronomy and Astrophysics (IUCAA) for thier computational fascility.

PhD is a long stressful journey, but it becomes enjoyable if you are surrounded by the people who love you and believe in you. I am blessed to have met someone so amazing that I can write a separate thesis on her altogether, Ms. Pooja Munjal. She has lived the experience of my PhD with me, and this thesis may bear my name,

but the personal and emotional efforts it has taken to complete it are shared with her. It isn't very easy to express in words what you feel towards the people who have lived around you for about one-third of your life. I will mention the names, but you already know how much each one of you means to me. My oldest friends Anil Nara and Rahul Jain, for sticking with me for so long. A big thanks to my gang from college days Vaibhav Jain, Poonam, Megha Rajoria, Naman Jain, Vivek Agrawal, Anvi Khandelwal and Ritu Jain.

During my PhD. I have come across so many amazing people, and I would like to acknowledge the support of a few awesome friends I have made here. My closest friends with whom I have had unforgettable fun Avinash, Arnob, Sudhanshu, Shailesh, Yogesh, Satyam, Swagatam, Priyanka Madhu and Ayushi. They have made each day here more enjoyable. Playing and chatting with them acted like a relaxing therapy which provided me with energy to sustain my enthusiasm over all these years. I have also had the pleasure of being friends with Navketan, Deepak, Anirban, Ramu, Shekhar, Jyotsna, Amit, Shubhendu, Samriddhi, Karishma, Hema, Dahlia, Nupur, Yogesh Mishra, Sudipto and Vishavdeep.

Finally, I would like to thank my parents for never stopping me from following my dreams. I thank my brother for always being there for me. He has always been the first one I have turned to over the years for advice, and he has helped me make the right decisions. My family has always been small in size, but it has never taught me to dream small. Their support and love is the fuel that burns in the torch I use to guide my way through life.

Abstract

The environment of galaxies is crucial to their evolution. Galaxies in the nearby Universe are observed to have a lower star formation rate when compared to galaxies at redshift ∼1-2. Observations have shown that galaxy properties are related to its large-scale environment. In order to understand the effects of these environments on galaxy evolution one needs to not only understand the physical processes that are at play in these environments but also how properties of galaxies evolve from one environment to another.

In this thesis, we use a variety of tools: analytical models, multi-wavelength observations and hydrodynamical simulations, to probe the effects of the large-scale environment on galaxy properties. We focus on two processes that affect the galaxy properties, namely, ram pressure stripping and mergers. We also study the effects of large-scale filament environment in observations as well as simulations. The following sections describe the work in more detail.

Ram pressure stripping: An analytical approach

To differentiate between various quenching mechanisms in action along with ram pressure, one needs models for ram pressure stripping. We propose an analytical model to study ram pressure stripping as a mechanism of gas removal from a galaxy disc in the absence of other processes.

We vary parameters related to the ambient medium and galaxy to get a quantitative idea of their effects on the amount of gas that remains in a stripped galaxy. A galaxy with a certain mass is assumed to be free-falling from a distance of $2R_{\rm vir}$, where $R_{\rm vir}$ is the virial radius of the central object. We divide galaxy disc into annuli: if ram pressure is more than the restoring force per unit area; the gas in the annulus is stripped.

In each case, we model the worst-case scenario (i.e., the maximum effect due to ram pressure). We show that there is little variation in the worst-case scenario with redshift. We find that gas discs in galaxies with a higher spin parameter get stripped sooner than galaxies with a smaller spin parameter. Galaxies in cluster halos get stripped of gas more efficiently as compared to group and galaxy halos. We comment on the limitations of our model and situations where a significant amount of gas may be retained in the galaxy disc, also giving illustrations for the same. We also discuss the star formation in these galaxies as they fall into a halo.

Study of large-scale filament environment in the Coma supercluster

In the current picture of the Universe, a large-scale filament environment is an intermediate stage between the void and cluster environments. Galaxies spend a significant fraction of time in filaments compared to clusters and void. The story of galaxy evolution is incomplete if the impact of this environment on observable properties of galaxies are not studied. We studied galaxies in different environments in the Coma supercluster. The Coma supercluster is ~ 500 square degree on the sky. It comprises of two clusters, a network of filaments comprising galaxies and relatively

isolated void galaxies. We focus on the effects of the filaments. Intrafilamentary gas is not directly observable. We try to capture its effect on galaxies passing through it using the information available in UV and optical properties of galaxies.

We primarily use data from the Sloan Digital Sky Survey (SDSS) and the *GALEX* mission. We use luminosities in different optical bands u, g and r along with $H\alpha$ emission-line data from the SDSS. $H\alpha$ probes recent star formation over a time-scale of $\lesssim 20$ Myr. The UV luminosity measures star formation over a time-scale of ~ 100 Myr. We identify different components of the cosmic-web: large-scale filaments and voids using the Discrete Persistent Structures Extractor, and groups and clusters using the Hierarchical Density-based spatial clustering of applications with noise, respectively.

We find that in the Coma supercluster, the median emission in $H\alpha$ increases, while the $g-r$ and $FUV-NUV$ colours of galaxies become bluer moving further away from the spine of the filaments out to a radius of ~ 1 Mpc. On the other hand, the opposite trend is observed as the distance between the galaxy and centre of the nearest cluster or group decreases. Our analysis supports the hypothesis that properties of galaxies are not just defined by its stellar mass and large-scale galaxy density, but also by the environmental processes modulated by the intra-filament medium, whose role in accelerating galaxy transformations is yet to be investigated thoroughly.

Study of effects of large-scale filament environment in simulations

The EAGLE (Evolution and Assembly of GaLaxies in their Environment; Schaye et al. (2015)) suite of simulation uses Gadget-3 SPH code to run cosmological simulations of various box sizes and physical parameters. Since there is more information available in simulations compared to observations, in this project, we expect to gain a deeper insight into the large-scale filament environment and factors which contribute most to the quenching of star formation.

We use the largest available box in the EAGLE simulation of 100 h^{-1} Mpc. Using similar technique as used in Mahajan et al. (2018), we categorise the large-scale environment and perform a stacked analysis of various mock observations. We take combinations of the identified clusters and cut a slice from the simulation box. A slice of a co-moving width of 60 Mpc is chosen with the normal to the line joining the clusters. The galaxies projected on a 2D plane in the slice in O' are used for classifying the environment. To find the galaxies inside the slices, we use the EAGLE catalog and identify the friends-of-friends (FOF; Einasto et al. (1984)) groups containing more than four galaxies and having total mass $\geq 10^{12.5}$ $M_\odot$. The large-scale filaments are identified using the DisPerSE (Sousbie et al., 2011). This procedure allows us to have 36 ($^9C_2$) observation in a single snapshot and enables us to perform stacking analysis to study properties of galaxies on filaments.

We compare and contrast our results with Mahajan et al. (2018) as well other observations. Our results show that observable properties of galaxies change in the filament environment in the EAGLE simulation. We also discuss how the galaxies in the filament environment compare with their counterparts in other environments.

Hydrodynamical simulations of galaxy merger to study effects on star formation

Galactic interactions in the form of collisions or 'fly-by', structurally transform and accelerate the evolutionary processes in galaxies. It is one of the main mechanisms for the quenching of star formation. The evolution of interstellar gas and star formation rate are dictated by the kinematics of the interactions. Mergers of galaxies of similar masses are called *major mergers*, and for galaxies with one galaxy much more massive than the other, like in the case of a spiral and dwarf galaxy, they are called *minor mergers*. The observational signatures of minor mergers are much weaker than those of major mergers, so observational comparisons are harder. For a minor merger to have a significant impact on the central galaxy, the mass ratio should be more than 0.01. A galaxy merger is complicated by various processes with quenching depending upon various parameters related to the trajectory and parameters intrinsic to both the galaxies.

We perform hydrodynamical simulations using the `RAMSES` code (Teyssier, 2002a). This work focuses on merger between a massive central galaxy ($M \sim 10^{12}$ $M_\odot$) and a dwarf galaxy ($M \sim 10^{9}$ $M_\odot$), therefore, we concern ourself with minor mergers. We use Kennicutt-Schmidt law (Kennicutt, 1989) to check the feedback required for the simulation. We have used delayed cooling (Teyssier et al., 2013) as the feedback mechanism. We perform merger simulations in various parameter settings: varying pericentric distances, spin-parameters, gas fractions, and orientation of the spin axis of the dwarf galaxy.

Our results show the effects on the star formation of different parameters related to the dwarf galaxy in a merging scenario. We also discuss how the fraction of gas that remains in the disk is affected by variation in different parameters. The results could have an implication for "missing satellite" problem.

Summary and future work

This thesis is focussed on the effects of the environment on galaxy properties. We explored processes like ram pressure stripping and galaxy-galaxy mergers using analytical models and hydrodynamical simulations, respectively. The other half of the thesis focuses on the galaxies in the different environments. The main conclusions of this thesis for the four projects are:

- Using the analytical model for ram pressure stripping, we find that galaxies high spin parameters get stripped off their gas more, and galaxies in clusters lose their gas more efficiently than in groups and galactic environments.
- Our analysis using multi-wavelength data for Coma supercluster and EAGLE simulations support the hypothesis that properties of galaxies are affected by the environmental processes resulting due to the intrafilamentary gas.
- Hydrodynamical simulations of minor merger suggests that effects on the star formation properties and the gas that remains in the disk of the dwarf galaxy depends upon its various intrinsic and kinematic properties.

Publications

This thesis is mainly based on the following publications:

- **Singh, A.**, Mahajan, S. and Bagla, J. S. "Study of galaxies in large-scale filament environment in EAGLE simulation", under review in MNRAS since January, 2020.
- **Singh, A.**, Gulati, M. and Bagla, J. S. "Ram pressure stripping: An analytical approach", 2019, *MNRAS, 489, 5582*
- Mahajan, S., **Singh, A.** and Shobhana, D. "Ultraviolet and optical view of galaxies in the Coma supercluster", 2018, *MNRAS, 478, 4336*
- **Singh, A.**, Mahajan, S. and Shobhana, D. "Caught in the web: Tale of filament galaxies", 2018 (accepted for publication in IAU proceedings, *Proceedings IAU Symposium No. 341*

Contents

List of Figures

List of Tables

Chapter 1

Introduction

The mysteries of the Universe have always puzzled humans. Galaxies are the appropriate units for studying the Universe at the largest scales which makes galaxy evolution an active field of research. We have come very far from cataloging the galaxies according to their diffused emission by Messier William and John Herschel to understanding their evolution in multiple wavelengths. Observations, both wide and deep, have been used to develop a model of the Universe called Λ cold dark matter (ΛCDM). In this preferred model Universe consists of approximately 30 % matter (5% baryonic matter + 25% dark matter) and 70% dark energy. Galaxies are formed in dark matter halos, and these galaxies are the building blocks for what we called as the large-scale structure of the Universe.

Some of the earliest studies on galaxies were their classification, according to morphology. Hubble (1936) and later de Vaucouleurs (1959) classified galaxies based on features like spiral arms, ring, and bar. The classification categorized galaxies broadly into ellipticals and spirals, with spirals subclassified based on the presence of bars. It was believed that smooth "feature-less" elliptical galaxies must have interacted to give rise to "complicated" spiral galaxies. Therefore, the elliptical galaxies were called early-type galaxies, and spiral galaxies were called late-type galaxies. It was later observed that elliptical galaxies have little star formation, and disc-like spiral galaxies had active star formation.

The distribution of galaxies in the Universe on large-scales has a web-like structure, as shown in Figure 1.1. There are low-density (voids) and high-density regions (clusters and groups). Clusters and groups are connected by intermediate density filaments. It is observed that the star formation rate density peaks at a redshift of 1-2 (Madau et al., 1998; Hopkins, 2004; Bouwens et al., 2009; Behroozi et al., 2013) and decreases by a factor of more than 10 to the present time (Figure 1.2). The quenching of star formation has been extensively studied in recent years. Quenching of star formation has been found to be closely related to the large-scale environment of galaxies. Galaxies in groups and clusters on an average have a low star formation rate compared to galaxies in low-density void environments. Environmental processes like galaxy-galaxy interaction, harassment, strangulation, and ram pressure stripping play a crucial role in quenching star formation. For a complete understanding of quenching of star formation, the mechanisms and their impact in different environments needs to be studied.

In recent years, multi-wavelength observations have been successfully used to understand many aspects of the quenching of star formation in galaxies. Using

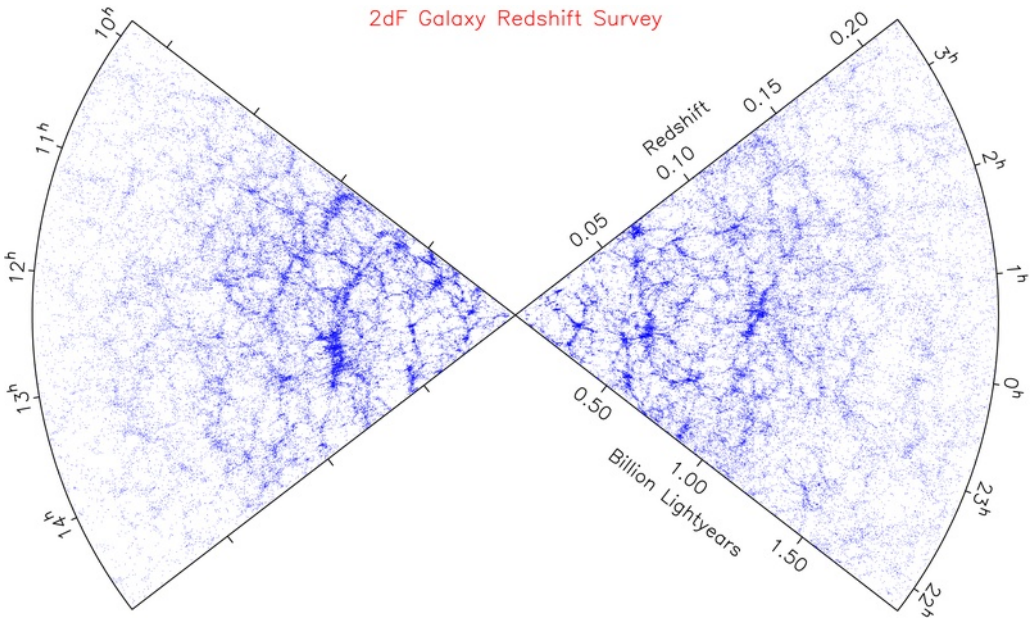

Figure 1.1: Large-scale structure of the Universe. Each dot represents a galaxy and color represents galaxy density. Image Credit: 2dFS

information from different wavelengths helps to trace star formation activity on different timescales in the galaxies. With the advent of observations wide to capture all environments, it has become easier to comprehend the effects and mechanisms responsible for quenching. Hydrodynamical simulations have been able to reproduce some of the trends observed successfully (Somerville & Davé, 2015). Due to recent advances in technology, one is now better able to simulate scales and processes that play a crucial role in shaping the properties of galaxies. They also allow us to generate mock observations and perform studies with large enough statistical samples, which is not yet possible in observations with current telescopes. Using both multi-wavelength observations and simulations, one is able to study the statistical effects as well as the mechanisms responsible for the quenching of star formation.

In this chapter, we will discuss the growth and formation of structure in the ΛCDM Model. We will discuss our current understanding of galaxy formation and of some processes that lead to quenching of star formation in galaxies residing in large-scale environments. We will also briefly discuss two different types of hydrodynamical techniques used to simulate astrophysical processes. We end this introduction by discussing the goals and outline of this thesis.

1.1 The ΛCDM Model

General theory of relativity (GTR) describes gravity as curvature in four-dimentional space-time. The theory predicts that the Universe is not static. According to Cosmological principle Universe is homogeneous and isotropic at large scales ($\sim$ 100 Mpc h^{-1}). For such a Universe, metric of space-time can be explained by the Friedmann-Lemaître-Robertson-Walker (FLRW) metric, given by:

$$ds^2 = -c^2dt^2 + a^2(t)\left(\frac{dr^2}{1-Kr^2} + r^2d\Omega^2\right) \tag{1.1}$$

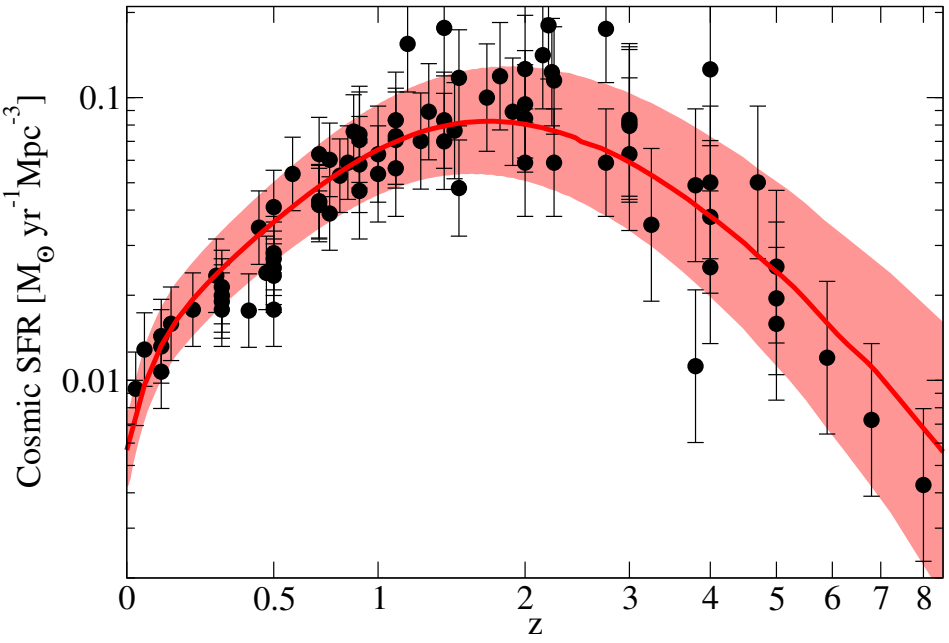

Figure 1.2: Star formation rate density history of the Universe with redshift.(Image credit: Behroozi et al. (2013))

where K is called *curvature*. $K = 0$ for Euclidean geometry, $K = 1$ for the positive curvature and $K = -1$ for negative curvature. The time coordinate here is *cosmic time* and the spatial coordinates are called *comoving coordinates*. $a(t)$ gives information about how distance between two points scales with time, therefore, it is called *scale factor*.
In GTR gravity is described by the Einstein equation:

$$G_{\mu\nu} = \frac{8\pi G}{c^4} T_{\mu\nu} \tag{1.2}$$

where $G_{\mu\nu}$ is the *Einstein tensor* which depends on the metric of space-time, and $T_{\mu\nu}$ is the energy-momentum tensor which describes the matter content. Putting this metric in the Einstein's equation gives the *Friedmann Equations*:

$$H^2 \equiv \left(\frac{\dot{a}}{a}\right)^2 = \frac{8\pi G}{3}\rho + \frac{\Lambda c^2}{3} - \frac{Kc^2}{a^2} \tag{1.3}$$

while the acceleration equation is:

$$\frac{\ddot{a}}{a} = -\frac{4\pi G}{3}\left(\rho + \frac{3P}{c^2}\right) + \frac{\Lambda c^2}{3} \tag{1.4}$$

where H is the *Hubble parameter*.

The dot denotes derivative with respect to cosmic time. G is the Gravitational constant, Λ is the cosmological constant, ρ is the energy density, and $P(t)$ is the pressure.

1.1.1 Cosmological Expansion

Expansion of the Universe is described by Hubble parameter (euqation (1.3)). The present value of the Hubble parameter is called the *Hubble constant*. It is often parameterized in the form of a dimensionless factor "h" in units of 100 h km s^{-1} Mpc^{-1}. As Universe expands, the photons released from a source are red-shifted before it reaches an observer. This shift in wavelength is directly proportional to the expansion factor at the time of emission from the source ($a(t_{em})$) and its value when it reached the observer ($a(t_{obs})$). The redshift of the object observed at present is given by:

$$1 + z = \frac{1}{a(t)} \tag{1.5}$$

Here $a(t)$ is the expansion factor of the Universe when the photon was emitted. We have assumed that the present value of the expansion factor is unity.

1.2 Constituents of the Universe

Equation (1.3) showed that the expansion of the Universe depends upon density (ρ) and curvature (K) of the Universe. Instead of expressing the exact values of density of different constituents, they are conveniently expressed in terms of the critical density of the Universe given by:

$$\rho_c \equiv \frac{3H^2}{8\pi G} \tag{1.6}$$

which is the density required to keep the Universe flat ($K = 0$). Its present value estimated by the Planck Collaboration (2016) is:

$$\rho_{c,0} = 1.878\ h^2 \times 10^{-29}\ g\ cm^{-3} \tag{1.7}$$

It is observed that the present density of the Universe (ρ_0) is very close to ρ_{c0}, so that our Universe is consistent with spatially flat ($K = 0$). Such fine-tuning in K is surprising and is called the *flatness problem*.

The fractions, called density parameter (Ω), contributed by each component are calculated as:

$$\Omega \equiv \frac{\rho}{\rho_c} \tag{1.8}$$

The Friedmann Equation (1.3) is expressed with different Ω's and separating contribution to ρ by collision-less particles which do not interact electromagnetic radiation called the *cold dark matter* (Ω_{c0}), baryons (Ω_{b0}), curvature (Ω_{K0}) and radiation (Ω_{r0}):

$$\frac{H^2}{H_0^2} = \Omega_\Lambda + \frac{\Omega_{c0}}{a^3} + \frac{\Omega_{b0}}{a^3} + \frac{\Omega_{r0}}{a^4} + \frac{\Omega_{K0}}{a^2} \tag{1.9}$$

Planck Collaboration (2016) for ΛCDM model found values:

$$\Omega_\Lambda = 0.685 \pm 0.0013 \qquad \Omega_{m0} = 0.315 \pm 0.0013 \tag{1.10}$$

at 68% confidence level,

Here, $\Omega_{m0} = \Omega_{c0} + \Omega_{b0}$, i.e. it includes both CDM and baryons, which have same dynamics at large scales (since both are cold). It is possible to measure their individual contribution and one observes:

$$\Omega_{b0}h^2 = 0.02222 \pm 0.00023 \qquad \Omega_{c0}h^2 = 0.1197 \pm 0.0022 \tag{1.11}$$

also at 68% confidence level.

Planck Collaboration (2016) found the value of Hubble constant to be:

$$H_0 = (67.8 \pm 0.9)\ km\ s^{-1}Mpc^{-1} \tag{1.12}$$

i.e., $h \cong 0.68$. Since $\Omega_c \gg \Omega_m$, the non-baryonic dark matter dominates the gravitational collapse. It accounts for $\approx 26\%$ of the energy budget of the Universe. The main component of the Universe (69%) is what is called *"Dark Energy"* (Ω_Λ). One certain thing we know about this component is that it has negative pressure, and it is because of this component that the Universe is undergoing accelerated expansion. Before the dark energy begins to dominate, structure formation can proceed at a faster pace. Observable baryonic matter contributes close to 5%.

1.3 Structure growth in ΛCDM

We observe large-scale structures in the Universe. Considering the hierarchical structure formation scenario, these structures form from small perturbations. Cosmic microwave observations suggest that the Universe started with perturbations in the background density field of the order 10^{-5} at the epoch of reionisation when the Universe was about 300000 years old. These perturbations grow by gravitational instability. Eventually, these perturbations grow enough to form halos of dark matter. Baryons were confined inside these dark matter halos and later cool to form discs to conserve angular momentum acquired in the process of halo formation. There have been many theoretical studies to understand this using various techniques. In what follows we briefly describe the model of structure formation (Zel'Dovich, 1970; Peebles, 1974, 1980; Mo et al., 2010a).

Perturbations in density field can be expressed in terms of overdensity. If the density of matter at location $\vec{r}$ is $\rho(\vec{r})$ then, an overdensity is given by:

$$\delta(\vec{r}) = \frac{\rho(\vec{r}) - \bar{\rho}}{\bar{\rho}} \tag{1.13}$$

where $\bar{\rho}$ is the average density, Fourier component $\delta(\vec{r})$ is described by:

$$\delta_{|k|} = \frac{1}{V}\int \delta(\vec{r})e^{-i\vec{k}\cdot\vec{r}} \tag{1.14}$$

The evolution of perturbations can be categorized into two regimes: Linear with $|\delta| \ll 1$ and non-Linear with $|\delta| \gtrsim 1$. When the Universe is 300,000 years old with a temperature of around 3000 K, protons and electrons combine to form atoms. This epoch is referred to as the recombination epoch. After recombination epoch photons are decoupled from baryons. Baryons behave as an 'ideal gas' (i.e., a fluid). Dark matter is (assumed to be) a collision-less fluid. With these assumptions, we can describe $\delta(t)$ using fluid equations which holds true for baryons as frequent

collisions between the particles allow them to establish a local thermal equilibrium making the mean free path of particles much smaller than scales of interest. For dark matter the velocity dispersion of the particles is sufficiently small such that diffusion can be neglected on the scale of interest.

In the following subsections, we will first describe linear structure formation arising from small perturbations in the initial phase of the Universe. In the following section, we describe how these initial perturbations are described.

1.3.1 Linear structure formation

Let $\rho(\vec{r},t)$,$\vec{u}(\vec{r},t)$, and $P(\vec{r},t)$ describe the density, velocity, and pressure of a fluid at location $\vec{r}$, at t, with $\phi(\vec{r},t)$ being the corresponding gravitational potential.

$$\textit{continuity equation}: \quad \frac{\partial \rho}{\partial t} + \vec{\nabla}_r \cdot (\rho\, \vec{u}) = 0 \tag{1.15}$$

$$\textit{Euler equation}: \quad \frac{\partial \vec{u}}{\partial t} + \left(\vec{u}\cdot\vec{\nabla}_r\right)\vec{u} + \frac{\vec{\nabla}_r P}{\rho} + \vec{\nabla}_r \phi = 0 \tag{1.16}$$

$$\textit{Poisson equation}: \quad \nabla_r^2 \phi = 4\pi G\rho \tag{1.17}$$

We can rewrite $\vec{r} = a(t)\vec{x}$, where $\vec{x}$ is the position vector in the comoving coordinates. The proper velocity $\vec{u} = \dot{\vec{r}}$ can be written as:

$$\vec{u} = \dot{a}(t)\vec{x} + \vec{v}, \quad \vec{v} \equiv a\dot{\vec{x}} \tag{1.18}$$

where dot means a derivative with respect to time and $\vec{v}$ is the peculiar velocity in the comoving frame. The time and space derivatives can be rewritten in terms of

$$\vec{\nabla}_r \to \frac{1}{a}\vec{\nabla}_x \equiv \frac{1}{a}\vec{\nabla}; \quad \frac{\partial}{\partial t} \to \frac{\partial}{\partial t} - \frac{\dot{a}}{a}\vec{x}\cdot\vec{\nabla}_x \equiv \frac{\partial}{\partial t} - \frac{\dot{a}}{a}\vec{x}\cdot\vec{\nabla} \tag{1.19}$$

Using the above transformations in equations 1.15 – 1.17 we can write:

$$\frac{\partial \delta}{\partial t} + \frac{1}{a}\vec{\nabla}\cdot((1+\delta)\,\vec{v}) = 0 \tag{1.20}$$

$$\frac{\partial \vec{v}}{\partial t} + \frac{\dot{a}}{a}\vec{v} + \frac{1}{a}\left(\vec{v}\cdot\vec{\nabla}\right)\vec{v} + \frac{\vec{\nabla} P}{a\bar{\rho}(1+\delta)} + \frac{\vec{\nabla}\Phi}{a} = 0 \tag{1.21}$$

$$\nabla^2\Phi = 4\pi G\bar{\rho}a^2\delta \tag{1.22}$$

where $\vec{v}$ is peculiar velocity in comoving coordinate system. We also define the modified gravitational potential, $\Phi = \phi + a\ddot{a}x^2/2$, which is sourced by density perturbation $\rho - \bar{\rho}$ only.

Once we have defined our cosmology (by fixing $a(t)$) and chosen an equation of state (EOS) $P(\rho, S) = P(\rho, S)$, where S is entropy, these equations can be solved. Assuming the EOS to be that of an ideal fluid:

$$P = \frac{k_{\rm B}T}{\mu m_{\rm p}}\rho \tag{1.23}$$

Here $k_{\rm B}$ is Boltzmann constant, μ is mean molecular mass, $m_{\rm p}$ is mass of the proton, and T is temperature.

If we assume that evolution is adiabatic ($dS/dt = 0$), using the laws of thermodynamics for a monoatomic gas, equation of state becomes:

$$P = \rho^{5/3} \exp\left(\frac{2}{3}\frac{\mu m_{\rm p}}{k_{\rm B} S}\right) \tag{1.24}$$

Substituting this in the Euler equation we get the following set of equations:

$$\frac{\partial \delta}{\partial t} + \frac{1}{a}\vec{\nabla} \cdot ((1+\delta)\,\vec{v}) = 0 \tag{1.25}$$

$$\frac{\partial \vec{v}}{\partial t} + \frac{\dot{a}}{a}\vec{v} + \frac{1}{a}\left(\vec{v}\cdot\vec{\nabla}\right)\vec{v} = -\frac{\vec{\nabla}\Phi}{a} - \frac{c_{\rm s}^2}{a}\frac{\vec{\nabla}\delta}{(1+\delta)} - \frac{2T}{3a}\vec{\nabla}S \tag{1.26}$$

$$\nabla^2\Phi = 4\pi G\bar{\rho}a^2\delta \tag{1.27}$$

The next step is to linearise the fluid equations. Assuming perturbations in ρ and v to be very small we neglect all the higher order terms. Further assuming $T = \bar{T} + \delta T$, ignoring the perturbation terms containing δT and differentiating equation (1.2) with respect to t and using Euler and Poisson equations we get:

$$\boxed{\frac{\partial^2\delta}{\partial t^2} + 2\frac{\dot{a}}{a}\frac{\partial\delta}{\partial t} = 4\pi G\bar{\rho}\delta + \frac{c_{\rm s}^2}{a^2}\vec{\nabla}^2\delta + \frac{2\bar{T}}{3a^2}\vec{\nabla}^2 S} \tag{1.28}$$

where

$$c_{\rm s} = \left(\frac{\partial P}{\partial \rho}\right)_{\rm S}^{1/2} \tag{1.29}$$

is the adiabatic speed of sound. Equation (1.28) describes the evolution of perturbations in a non-relativistic fluid in linear regime ($\delta \ll 1$). It is convenient to work in Fourier space as all the modes evolve independently of each other in this linear regime. Defining $\delta(\vec{r},t) = \sum_k \delta_{\vec{k}(t)} e^{i\vec{k}\cdot\vec{r}}$ and $\delta_{\rm S} = \frac{S(\vec{r})-\bar{S}}{\bar{S}} = \sum_k S_{\vec{k}}(t) e^{i\vec{k}\cdot\vec{r}}$ equation (1.28) in Fourier space for each mode becomes:

$$\boxed{\frac{d^2\delta_{\vec{k}}}{dt^2} + 2\frac{\dot{a}}{a}\frac{d\delta_{\vec{k}}}{dt} = [4\pi G\bar{\rho} - \frac{c_{\rm s}^2 k^2}{a^2}]\delta_{\vec{k}} - \frac{2\bar{T}}{3a^2}k^2 S_k} \tag{1.30}$$

It can be seen that there can be two types of perturbations. Both density and entropy can seed structure formation.

$$\begin{aligned} \textit{Isentropic Perturbations}: &\quad \delta_{\rm S} = 0 \\ \textit{Isocurvature Perturbations}: &\quad \delta = 0 \end{aligned}$$

Isoentropic and Isocurvature perturbations are both orthogonal to each other, and any generic perturbation can be re-written as a linear combination of both.

In what follows we are interested in structure formation after the recombination of electrons with protons to form atoms. At this stage baryonic matter becomes a pressureless fluid and thus $c_{\rm s} = 0$. We also focus on isoentropic perturbations ($\delta_{\rm S} = 0$) evolving adiabatically. In this epoch the Universe is dominated by matter

therefore, radiation can also be ignored. Putting all of this in equation (1.28) we get:

$$\frac{d^2\delta_{\vec{k}}}{dt^2} + 2\frac{\dot{a}}{a}\frac{d\delta_{\vec{k}}}{dt} = 4\pi G\bar{\rho}_{\rm m}\delta_{\vec{k}} \tag{1.31}$$

where $\rho_{\rm m}$ is the matter density of the Universe.

There are two solutions to equation (1.31) identified as decaying and growing modes:

$$Decaying\ Mode: \qquad \delta_- \propto H(t) \tag{1.32}$$

$$Growing\ Mode: \quad \delta_+ \propto H(t)\int_0^t \frac{dt'}{a^2(t')H^2(t')} \tag{1.33}$$

General solution of equation (1.31) is a linear combination of growing and decaying mode as:

$$\delta(t) = C_1\delta_+ + C_2\delta_- \tag{1.34}$$

where C_1 and C_2 are constants. Since decaying mode decays rapidly as the Universe expands we can write $\delta(t) \propto \delta_+$ at late times. We can rewrite $\delta_+ \propto D(z) \propto \frac{g(z)}{1+z}$, where $D(z)$ is called the *linear growth rate*. Carroll et al. (1992) gave an approximation for $g(z)$ as:

$$g(z) \simeq \frac{5}{2}\Omega_{\rm m}(z)\left[\Omega_{\rm m}^{4/7}(z) - \Omega_\Lambda(z) + \left(1+\frac{\Omega_{\rm m}(z)}{2}\right)\left(1+\frac{\Omega_\Lambda}{70}\right)\right]^{-1} \tag{1.35}$$

For an Einstein-de Sitter (EdS) cosmology we know that $\Omega_{\rm m,0} = 1$ and $\Omega_{\Lambda,0} = 0$. Putting these into equation (1.35) we get a simple solution:

$$g(z) = 1 \tag{1.36}$$

$$\delta_+ \propto a \propto t^{2/3} \tag{1.37}$$

$$\delta_- \propto t^{-1} \tag{1.38}$$

We also know that perturbations will grow at a faster rate in EdS than in a Universe with $\Omega_{\rm m,0} < 1$. Also, If we have a non-zero cosmological constant the perturbations will grow slowly as the expansion rate of Universe will be more than the EdS Universe.

1.3.2 Growth History

In the early phases of structure formation the Universe is matter dominated ($\Omega_{\rm m} \sim 1$), hence follows a growth identical to the EdS Universe. The growth factor goes as:

$$D(t) \propto a(t) \propto t^{2/3} \tag{1.39}$$

As it evolves, an open Universe becomes relatively empty at expansion factor:

$$a_{\rm f} = \frac{1}{1/\Omega_0 - 1} \tag{1.40}$$

at which the expansion factor is:

$$a(t) = H_0 t \tag{1.41}$$

which halts the formation of structure at large-scale because gravity is not able to overcome the cosmic expansion. At this time, growth factor is:

$$D(t) = constant \tag{1.42}$$

An important epoch in Λ-dominated Universe is when dark-energy takes over the dynamics and starts accelerating the Universe. This epoch occurs at the expansion factor of:

$$a_{\rm m,\Lambda} = \left(\frac{\Omega_{\rm m}}{2\Omega_\Lambda}\right)^{1/3} \tag{1.43}$$

Perturbations continue to grow at smaller scales where gravity can overcome the expansion. The regions like clusters and filaments still witness the flow of mass onto them.

1.3.3 Gaussian Random Fields

We would like to specify the characteristics of density contrast in the Universe ($\delta(\vec{r}, t)$) without calculating its value at every position in space-time coordinates. Assuming $\delta(\vec{r}, t)$ to be the outcome of a random process in the early Universe, one just has to specify the probability distribution:

$$P(\delta_1, \delta_2, \delta_3, \delta_4 ...) d\delta_1 d\delta_2 d\delta_3 d\delta_4 ... \tag{1.44}$$

where $\delta_1 = \delta(\vec{x_1}, t)$, etc. If the density fluctuations are Gaussian in nature then field values at an arbitrary set of N points is an N-variate Gaussian:

$$\boxed{P(\delta_1, \delta_2, \delta_3, \delta_4 ...) = \frac{1}{(2\pi)^N} \frac{exp(-Q)}{[det(C)]^{1/2}}} \tag{1.45}$$

$$with,\ Q = \frac{1}{2} \sum_{i,j} \delta_i (C^{-1})_{i,j} \delta_j \tag{1.46}$$

$$C_{i,j} = \langle \delta_i \delta_j \rangle = \xi(r_{12}) \tag{1.47}$$

Here $\xi(r_{12})$ is the *two-point correlation function*, which is the second moment of a Gaussian random field. Hence, using the equation (1.45) above can completely specify it.

As mentioned before it is advantageous to work in Fourier space. We describe matter field in Fourier space as:

$$\delta(\vec{r}) = \sum_k \delta_{\vec{k}} e^{i\vec{k}\cdot\vec{r}} \quad with \quad \delta_{\vec{k}} = \frac{1}{V} \int \delta(\vec{r}) e^{-i\vec{k}\cdot\vec{r}} d^3\vec{r} \tag{1.48}$$

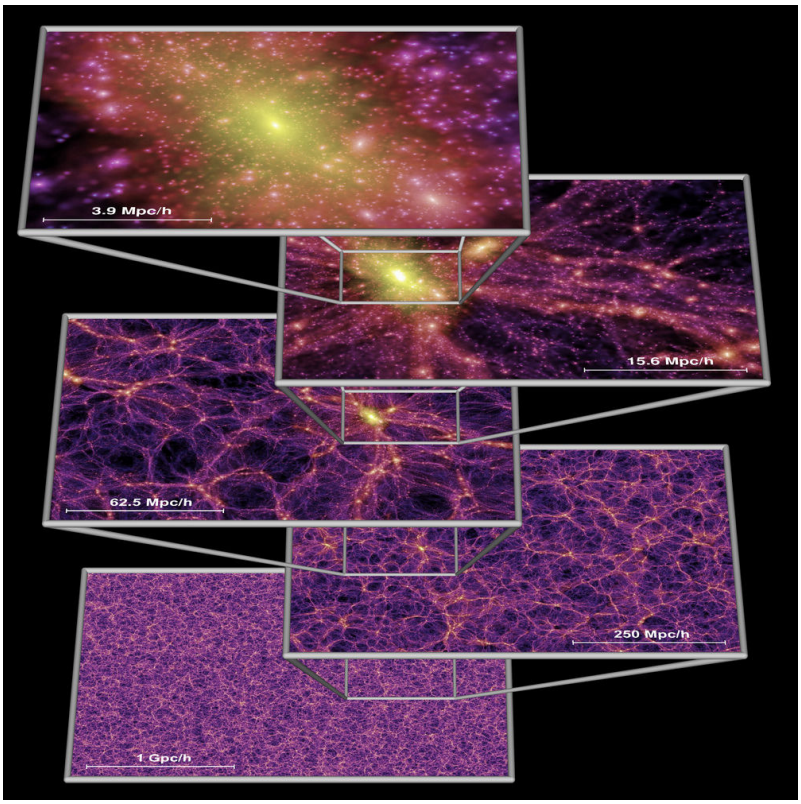

Figure 1.3: Structure formation is depicted at various scales using images from the millennium simulation. (Springel, 2005)

Note, V is the volume over which we assume the Universe to be periodic and thus we consider only finite values of k (known as "modes"). We also note that $\delta_{\vec{k}}$ is not equal to the Fourier transform of $\delta(\vec{r})$ which is $\delta(\vec{k})$, it is only in the case of infinite number of modes that one has $\delta(\vec{k}) = V\delta_{\vec{k}}$. Equation (1.48) shows that the perturbed density field can be written as superposition of plane waves with wavenumber k. Fourier transform of two-point correlation function is known as the *power spectrum*:

$$P(\vec{k}) = V\left\langle|\delta_{\vec{k}}|^2\right\rangle \tag{1.49}$$

which plays an identical role to two-point correlation function of completely specifying Gaussian random field.

Now the evolution of Gaussian random fields can be done by studying the evolution of Power Spectrum. Since all the modes evolve independently of each other in the linear regime, one can solve equation (1.28) for each mode independently. One can write the equation of the evolution of the power spectrum as:

$$P(k,t) = P_{\rm i}(k)T^2(k)D^2(t) \tag{1.50}$$

where, $P_{\rm i}(k)$ is the initial Power Spectrum, $T^2(k)$ is called the *transfer function* and $D(t)$ is the *linear growth rate*. The processes from which the primordial density fluctuations originate defined the initial shape of the power spectrum which can be

written as:

$$P_{\rm i}(k) = k^n \tag{1.51}$$

where n is called the *spectral index*. The case where $n \sim 1$ is called the *Harrison-Zeldovich spectrum* (Harrison, 1970).

Using Freedmann Equations (1.3-1.4) one can show that all the cosmologies behave like EdS at early times as $\lim_{a\to 0} \Omega_{\rm m}(a) = 1$. For a scale factor $a_{\rm m} > a_{\rm rec}$ where $a_{\rm rec}$ is the scale factor at recombination and assuming the Universe to be still in EdS state. One can define the transfer function as:

$$T(k) = \frac{\Phi_{\vec{k}}\left(a_{\rm m}\right)}{\Phi_{\vec{k}}\left(a_{\rm i}\right)} \tag{1.52}$$

where $\Phi_{\vec{k}}$ is Fourier component of gravitational potential, $a_{\rm i}$ is the expansion factor at the initial epoch. Therefore, in order to calculate $T(k)$ one needs to evolve different modes from some initial epoch to the matter dominated era. Accurate calculations involve solving Boltzmann equation in a perturbed FRW metric (Mo et al., 2010b) are used for computing $T(k)$.

1.3.4 Non-Linear structure formation

As the density fluctuations grow further ($\delta \gg 1$), perturbation theory is no longer valid, and growth enters the non-linear regime. In non-linear regime, modes couple with each other, and no analytical solutions exist as one can no longer describe the evolution of the perturbations using a simple growth rate. Hence, the assumption of the Gaussian random field is no longer valid due to mode-coupling. Higher-order moments are required to specify the density field completely.

Structure formation is hierarchical in nature, i.e., large structures build-up by merging of smaller structures (see Figure 1.3). Fluctuations at smaller scales collapse to form halos that merge to form large objects. We briefly describe the formalism of structure formation in the non-linear regime and refer the reader to Mo et al. (2010a) for details.

Top-Hat Spherical Collapse

To better understand non-linear collapse, let us consider an idealised case of top-hat spherical collapse (SC). We start with the assumption that the Universe is homogeneous, except for a single spherical perturbation having constant overdensity (top-hat). We assume the Universe to be in a matter-dominated phase. We treat dark matter as a collisionless fluid. For most of what follows in this section we assume an Einstein-de Sitter (EdS) cosmology as it is a good approximation in the matter dominated era:

$$\begin{aligned} \Omega(t) = 1, \quad & H(t)\cdot t = 2/3 \\ \bar{\rho} = \frac{1}{6\pi G t^2}, \quad & D(a) = a \propto t^{2/3} \end{aligned}$$

We can think of overdensity as a spherical shell which because of the collisionless nature of dark matter collapses without any pressure force. At some initial time $t_{\rm i}$,

the radius of some mass shell is denoted by r_i and let δ_i denote the back-ground density and $\bar{\rho}_\mathrm{i}$ denote the top-hat overdensity at this initial time.

Mass enclosed in the shell is:

$$M(r < r_\mathrm{i}) = \frac{4\pi}{3}\pi r^3(t)\bar{\rho}[1 + \delta(t)] \tag{1.53}$$

By integrating equation of motion one gets:

$$\frac{1}{2}\left(\frac{dr}{dt}\right)^2 - \frac{GM}{r} = E \tag{1.54}$$

For a bound object we have $E < 0$ which gives solutions:

$$r = A(1 - \cos(\theta)) \tag{1.55}$$

$$t = B(\theta - \sin(\theta)) \tag{1.56}$$

$$A = \frac{GM}{2|E|} \; ; \; A^3 = GMB^2 \tag{1.57}$$

where $\theta \in [0, 2\pi]$. The shell reaches maximum radius called the *turn-around radius* (r_max) at $\theta = \pi$, corresponding time is called *turn-around time* $t_\mathrm{ta} = t_\mathrm{max}$, which defines *virialisation time* ($t_\mathrm{vir} = 2t_\mathrm{max}$).

By applying conservation of energy one can show that:

$$\frac{r_\mathrm{max}}{r_\mathrm{i}} = \frac{1 + \delta_\mathrm{i}}{\delta_\mathrm{i}} \simeq \delta_\mathrm{i}^{-1} \tag{1.58}$$

Hence, we note that the turn-around radius (r_max) is not dependent on mass enclosed by the shell but only upon initial overdensity (δ_i). It is clear from equation (1.58) that smaller the perturbation, larger turn-around radius it has which also means that it will turnaround/collapse later. Using equations mentioned above one can show that overdensity evolution in top-hat spherical perturbation model is:

$$1 + \delta = \frac{\rho}{\bar{\rho}} = \frac{9}{2}\frac{(\theta - sin(\theta))^2}{(1 - cos(\theta))^3} \tag{1.59}$$

In the limit of $\theta \ll 1$ one can expand $\sin(\theta)$ and $\cos(\theta)$ to get the overdensity at time t_i as:

$$\delta_\mathrm{i} = \frac{6}{20}(6\pi)^{2/3}\left(\frac{t_\mathrm{i}}{t_\mathrm{max}}\right)^{2/3} \tag{1.60}$$

By linear theory, using equation (1.36) one gets the linearly extrapolated density contrast:

$$\delta_\mathrm{lin} = \frac{6}{20}(6\pi)^{2/3}\left(\frac{t}{t_\mathrm{max}}\right)^{2/3} \tag{1.61}$$

Comparing this (equation (1.61)) with the overdensity given by top-hat spherical collapse model (equation (1.59)) at turn-around ($t_\mathrm{ta}, \theta = \pi$) one gets:

$$SC\ Model: \quad 1 + \delta(t_\mathrm{ta}) \simeq 5.55, \tag{1.62}$$

$$Linear\ extrapolated: \quad \delta_\mathrm{lin}(t_\mathrm{ta}) \simeq 1.062 \tag{1.63}$$

At $t = t_{\rm vir}$ we have:

$$SC\ Model: \quad \delta(t_{\rm vir}) = \infty \tag{1.64}$$

$$Linear\ extrapolated: \quad \delta_{\rm lin}(t_{\rm vir}) \simeq 1.686 \tag{1.65}$$

Therefore, the regions with $\delta_{\rm lin} > 1.686$ in the linearly extrapolated density field should collapse to form halos according to the linear theory. This is called the *"critical overdensity for collapse"* ($\delta_{\rm c}$).

It is clear that the SC model discussed above is valid up till shell crossing. After shell-crossing M(r) is no longer a conserved quantity. Instead of forming a singularity like suggested by equation (1.64), individual oscillating shells interact gravitationally with each other, exchange energy (virialize) resulting in a virialized dark matter halo. If the system is in virial equilibrium:

$$2K_{\rm f} + W_{\rm f} = 0 \tag{1.66}$$

Energy conservation in spherical collapse gives:

$$E_{\rm f} = K_{\rm f} + W_{\rm f} = E_{\rm i} = E_{\rm ta} \tag{1.67}$$

where $E_{\rm i}$ is initial energy, $E_{\rm f}$ is final energy, $E_{\rm ta}$ is energy at turn-around, $K_{\rm f}$ is final kinetic energy, $W_{\rm f}$ is final potential energy. Using these equations one gets:

$$\boxed{r_{\rm vir} = r_{\rm ta}/2} \tag{1.68}$$

Here $r_{\rm vir}$ is *virial radius* and $r_{\rm ta}$ is the turn-around radius. One can calculate the average overdensity for EdS cosmology:

$$1 + \Delta_{\rm vir} = \frac{\rho(t_{\rm col})}{\bar{\rho}} \simeq 18\pi^2 \simeq 178 \tag{1.69}$$

Hence, in the SC model, a virialized halo has density 178 times the background density. This number of 178 changes once one takes into account realistic cosmology and other factors.

Zel'dovich Approximation

In the Eulerian ('grid') description, considered in the discussion above, perturbations grow or decay in amplitude at a fixed (comoving) position. This description is not valid as structure formation enters into the non-linear regime.

As overdensities ($\delta_{\rm i} > 0$) grow and become of order unity, the underdensities ($\delta_{\rm i} < 0$) would grow to $\delta < -1$, which is unphysical. In the Lagrangian description of fluid motion, we follow the motion of individual particles. Unlike Eulerian description, it continues to be fairly accurate even in mildly non-linear regime.

One of the most intuitive descriptions of non-linear collapse using the Lagrangian description was given by Zel'Dovich (1970). It is based on a simple assumption known as *"Zel'dovich Approximation"* (ZA): *particles continue to move in the direction of their initial displacement* with the velocity expected in linear perturbation theory. This assumption is exact in case of a planar perturbation.

$$\vec{r}(t) = \vec{r}_{\rm i} - c(t) \cdot \vec{f}(\vec{r}) \tag{1.70}$$

where $\vec{r}_{\rm i}$ is initial (Lagrangian), comoving coordinates, $c(t)$ is function of time and $\vec{f}(\vec{r})$ is a vector function of initial coordinates, it specifies direction of velocity.

Mass conservation for a perturbation, as long as the mapping is one to one gives:

$$\rho(\vec{r},t)a^3(t) = \rho_{\rm i}(\vec{r}_{\rm i})d^3\vec{r}_{\rm i} \tag{1.71}$$

where $a(t)$ is the expansion-factor normalized to unity at the time $t_{\rm i}$. Since we are working in the comoving coordinates, scaling with respect to $a^3(t)$ is required.

Conservation of mass is valid till orbit crossing takes place, for any type of geometry, there is no requirement of assumption of spherical geometry. Using simple algebra, we get:

$$\rho(\vec{r},t) = \rho(\vec{r}_{\rm i}) \left\| \frac{d\vec{r}}{d\vec{r}_{\rm i}} \right\|^{-1} \tag{1.72}$$

where $\|A\| = |det(A)| = |\prod A_i|$, with A_i being the eigenvalues of matrix A. We can write:

$$\left(\frac{d\vec{r}}{d\vec{r}_{\rm i}}\right)_{jk} = \delta_{jk} - c(t)\frac{\partial f_j}{\partial r_k} \tag{1.73}$$

where δ_{jk} is Kronecker delta. Using equation (1.73) in equation (1.72) we get:

$$\rho(\vec{r},t) = \rho(\vec{r}_{\rm i})\frac{1}{|(1-c\lambda_1)(1-c\lambda_2)(1-c\lambda_3)|} \tag{1.74}$$

where $\lambda_1 \geq \lambda_2 \geq \lambda_3$ are eigenvalues of the deformation tensor $\dfrac{\partial f_j}{\partial x_k}$. Using the fact that $\rho_{\rm i}(\vec{r}_{\rm i}) = \bar{\rho}_{\rm i}\left[1+\delta_{\rm i}(\vec{r}_{\rm i})\right] \simeq \bar{\rho}_{\rm i}$ and $\bar{\rho}(t)a^3 = \bar{\rho}_{\rm i}a_{\rm i}^3$ we can rewrite equation (1.74) as:

$$1+\delta(\vec{r},t) = \frac{\rho(\vec{r},t)}{\bar{\rho}(t)} = \frac{1}{(1-c\lambda_1)\,(1-c\lambda_2)\,(1-c\lambda_3)} \tag{1.75}$$

Equation (1.75) enables us to understand structure formation in simpler terms:

- If $\lambda_i > 0$ means collapse will take place in the direction of the $i^{\rm th}$ eigenvector.
- If $\lambda_i < 0$ means expansion will take place in the direction of the $i^{\rm th}$ eigenvector.
- If $c(t) = 1/\lambda_i$ implies that 'shell crossing' will happen in the direction of the $i^{\rm th}$ eigenvector.
- If $c\lambda_1 \ll 1$ the perturbation growth is in the linear regime.

We can linearise equation (1.75) to get:

$$1+\delta(\vec{r},t) = \frac{1}{1-c\,(\lambda_1+\lambda_2+\lambda_3)} \simeq 1+c\,(\lambda_1+\lambda_2+\lambda_3) \tag{1.76}$$

This means that in linear regime we have

$$\delta(\vec{r},t) = c(t)Tr\left(\partial f_{\rm i}/\partial x_j\right) = c(t)\vec{\nabla}\cdot\vec{f} = c(t)(\lambda_1+\lambda_2+\lambda_3) \tag{1.77}$$

λ_1	λ_2	λ_3	Structure
+	-	-	pancake
+	+	-	filament
+	+	+	clump

Table 1.1: Configurations in collapse: depending on eigenvalues collapse results in pancake, filament or clump (cluster)

If we compare this with the equation $\delta(\vec{r},t) = D(t)\delta_{\rm i}$ we get that:

$$\boxed{c(t) = D(t) \text{ and } \vec{\nabla}\cdot\vec{f} = \delta_{\rm i}} \tag{1.78}$$

where $D(t)$ has been normalised such that $D(t_{\rm i}) = 1$. Using Poisson equation $\delta_{\rm i} = \nabla^2\Phi_{\rm i}/4\pi G\vec{\rho}_{\rm i}$ and that $\nabla^2 = \nabla\cdot\nabla$ we get:

$$\boxed{\vec{f} = \vec{\nabla}\Phi_{\rm i}/4\pi G\vec{\rho}_{\rm i}} \tag{1.79}$$

We can use the equation (1.78) and equation (1.79) in equation (1.70) to give:

$$\boxed{\vec{r}(t) = \vec{r}_{\rm i} - \frac{D(a)}{4\pi G\vec{\rho}_{\rm i}}\vec{\nabla}\Phi_{\rm i}} \tag{1.80}$$

Apart from not assuming spherical geometry, Zel'dovich Approximation has the advantage of being valid even in the quasi-linear regime although it breaks down when the structure formation becomes extremely non-linear with $\delta \gg 1$.

We summarize the conclusions of ZA in Table 1.1. It is clear looking at equation (1.75) that collapse first happens along the axis with the largest eigenvalue, leading to the formation of flattened structures which are called *Zel'dovich Pancakes*. This, in turn, compliments the assumption becoming exact. This is the reason ZA approximation works really well in explaining quasi-linear structure formation.

Press-Schechter Theory

We have shown in spherical collapse model that at time t, regions with $\delta(\vec{r},t) > \delta_{\rm c} \simeq 1.686$ would have collapsed to form dark matter halos. According to linear theory we have $\delta(\vec{r},t) = D(t)\delta_0(\vec{r})$ we can rewrite this as: regions with $\delta_0(\vec{r}) > \delta_{\rm c}/D(t)$ will have collapsed to form dark matter halos by time t. For what follows we keep this picture with a moving barrier in mind.

We will discuss a formalism given by *Press & Schechter* (**??**; hereafter, PS) for calculating the average number of objects that have collapsed starting from the primordial Gaussian density field. They assumed that the dense objects that can be seen at present result from the collapse of peaks in the initial density field. Those small perturbations have collapsed spherically under gravity to form these bound virialized objects.

Let $\delta_{\rm M}$ be the linear density field smoothed over a mass scale M,

$$\delta_{\rm M} = \delta(\vec{r};R) \tag{1.81}$$

where $M = \gamma_{\rm f}\bar{\rho}R^3$, then locations with $\delta_{\rm M} = \delta_{\rm c}(t)$ are the locations where, at t a halo of mass M will form out of this density field when evolved.

They postulated that: *The probability that $\delta_{\rm M} > \delta_{\rm c}(t)$ is the same as the mass fraction that resides in halos with mass greater than M at time t.*

The probability that a given point resides inside a region having overdensity above critical density is given by:

$$\mathcal{P}\left(\delta_{\rm M} > \delta_{\rm c}\right) = \frac{1}{\sqrt{2\pi}\sigma_{\rm M}} \int_{\delta_{\rm c}}^{\infty} \exp\left[-\frac{\delta_{\rm M}^2}{2\sigma_{\rm M}^2}\right] {\rm d}\delta_{\rm M} = \frac{1}{2}\,{\rm erfc}\left[\frac{\delta_{\rm c}}{2\sigma_{\rm M}}\right] \tag{1.82}$$

where $\sigma_{\rm M}$ is the variance of the density field smoothed on the scale R, ${\rm erfc}(x) = 1-{\rm erf}(x)$ is the complimentary error function, and we note that $\delta_{\rm c} = \delta_{\rm c}(t)$. According to the PS postulate, we thus have fraction of matter in collapsed halos with mass greater than M as:

$$F(>M,t) = \frac{1}{2}\,{\rm erfc}\left[\frac{\delta_{\rm c}}{2\sigma_{\rm M}}\right] \tag{1.83}$$

We observe, as $M \to 0$, $\sigma_{\rm M} = \infty$ and ${\rm erfc}(0) = 1$ PS postulate accounts for only $1/2$ of all matter in the Universe gets locked-up in halos. PS argued that it may be possible for an underdense region to be in a larger overdensity, therefore, they introduced a "fudge factor" of 2 making equation (1.83) :

$$F(>M,t) = 2\mathcal{P}\left[\delta_{\rm M} > \delta_{\rm c}(t)\right] \tag{1.84}$$

Let $n(M,t){\rm d}M$, be mass function, which is defined as the number of halos with mass-range $[M, M+{\rm d}M]$ per (comoving) volume:

$$n(M,t) = \frac{dn}{dM} = M\frac{dn}{d\ln M} \tag{1.85}$$

Fraction of mass that is locked up inside halos with mass-range $[M, M+{\rm d}M]$ is given by:

$$\frac{\partial F(>M)}{\partial M}{\rm d}M \tag{1.86}$$

Multiplying this equation with $\bar{\rho}/M$ gives us the halo mass function. Therefore we have:

$$n(M,t)dM = \frac{\bar{\rho}}{M}\frac{\partial F(>M)}{\partial M}dM \tag{1.87}$$

We can re-write $\partial\mathcal{P}/\partial M$ as:

$$\partial\mathcal{P}/\partial M = \partial\mathcal{P}/\partial\sigma_{\rm M} \times |{\rm d}\sigma_{\rm M}/{\rm d}M| \tag{1.88}$$

Finally, using PS postulate, and putting equation (1.84), equation (1.88) in equation (1.87) gives us:

$$n(M,t)dM = 2\frac{\bar{\rho}}{M}\frac{\partial\mathcal{P}\left(>\delta_{\rm c}\right)}{\partial M}dM = \sqrt{\frac{2}{\pi}}\frac{\bar{\rho}}{M^2}\frac{\delta_{\rm c}}{\sigma_{\rm M}}\exp\left(-\frac{\delta_{\rm c}^2}{2\sigma_{\rm M}^2}\right)\left|\frac{d\ln\sigma_{\rm M}}{d\ln M}\right|dM \tag{1.89}$$

In literature we find a rather compact form to represent equation (1.89). If we define a parameter $\nu \equiv \delta_c(t)/\sigma(M)$ we can rewrite PS mass function as:

$$\boxed{n(M,t)dM = \frac{\bar{\rho}}{M^2} f_{\rm PS}(\nu) \left| \frac{d\ln\nu}{d\ln M} \right| dM \quad \text{where} \quad f_{\rm PS}(\nu) = \sqrt{\frac{2}{\pi}} \nu e^{-\nu^2/2}} \tag{1.90}$$

This form scales out the dependence on the form of the matter power spectrum and the cosmology. It brings out the universal aspects of the formation.

Looking at this equation one can define a quantity called *characteristic mass*, M^*, by:

$$\sigma\left(M^*\right) = \delta_c(t) \left(\text{ i.e., by } \nu\left(M^*\right) = 1\right) \tag{1.91}$$

We note that that the characteristic halo mass will grow with time since $\delta_c(t)$ decreases with time. This leads to formation of more and more massive halos with time. If we assume a Power-law power spectrum we have:

$$\sigma^2(M) \propto \int^{R^{-1}} dk k^{n+2} \propto R^{-(n+3)} \propto M^{-(n+3)/3} \tag{1.92}$$

We can rewrite equation (1.90) as:

$$M^2 n(M) = \mathcal{N} M^{(n+3)/6} \exp\left(-\nu^2/2\right), \tag{1.93}$$

$$n(M) = \mathcal{N} M^{(n-9)/6} \exp\left(-\nu^2/2\right) \tag{1.94}$$

where $\mathcal{N}$ is a constant. As $\sigma(M)$ becomes smaller for large masses ν becomes larger. When $\nu \ll 1 (M \ll M^*)$, i.e., for low masses, we have a power-law slope. For $M \gg M^*$, the abundance of halos is exponentially suppressed.

1.4 Galaxies in the local Universe

Baryons follow dark matter, and they are pulled into gravitational potential created by dark matter halos. These dark matter halos acquire angular momentum while going through the gravitational collapse. Gas inherits this angular momentum, but since it can cool by emitting radiation, it cools to form a disc, conserving the angular momentum (Fall & Efstathiou, 1980). This disc then fragments and gives rise to features like spiral arms. The gas forms stars wherever it becomes dense and cool.

For quantifying the properties of galaxies, one requires different types of observations. For studying the distribution of light, one needs photometric measurements. To obtain the distribution of mass, one relies on kinematical measurements.

As different components of galaxies tend to emit energy in different wavebands; multi-wavelength measurements are needed to study the relative distributions and interplay between them. The stars emit in visible/near-IR, cold gas emits in sub-mm and radio, dust emits in far-IR, and hot gas emits in X-rays. For Chemical composition, star formation activity we need high resolution spectroscopy

Different processes are responsible for the evolution of the galaxy. Figure 1.4 shows all the known processes that affect the evolution of galaxies in the local Universe. The processes have been divided into fast (top) and slow (bottom). The fast

processes happen at free-fall time-scale $t_{\rm dyn} \sim (G\rho)^{-1/2}$ where G is the gravitational constant and ρ is the density of the object. Slow processes take much longer and have a timescale of the order of several rotational periods. These processes can further be divided based on whether they are internal to the galaxy (left) or are driven by the factors which are related to the environment of the galaxy (right). We will discuss some of the external processes responsible for galaxy evolution in section 1.5.

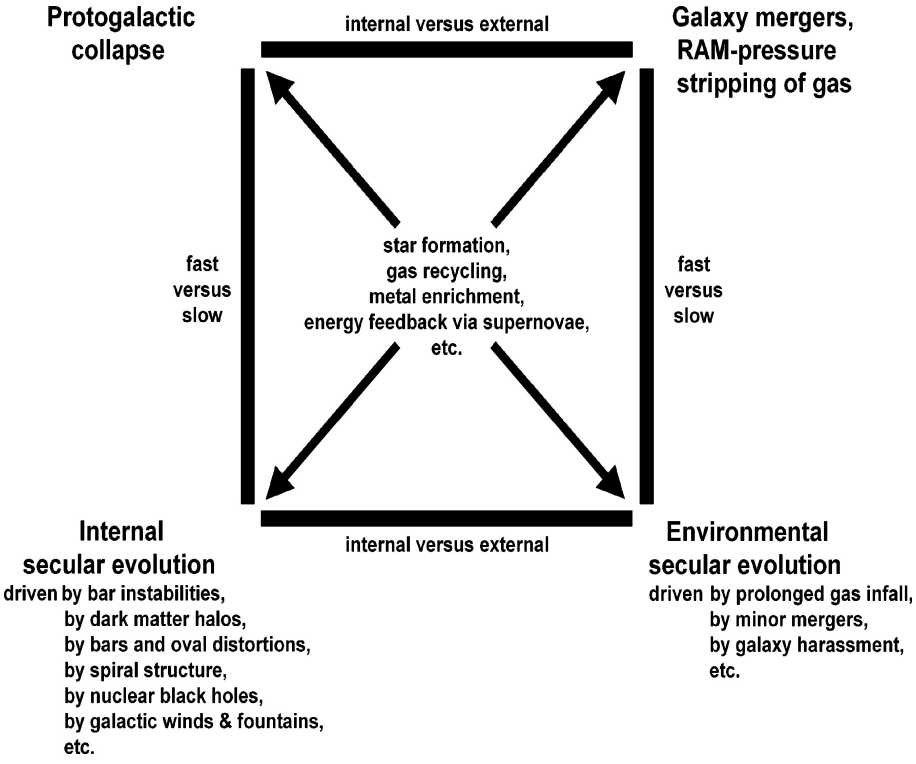

Figure 1.4: Morphological Box: Processes affecting galaxy evolution are divided into fast (top) and slow (bottom). The fast processes have a timescale of free-fall time, and slow processes take several galactic rotation periods. The processes are further divided into internal to the galaxy (left) and caused by environment processes (right). Image source: Kormendy & Kennicutt (2004)

1.4.1 Classification of galaxies

Hubble (1936) classified galaxies into the early-type galaxy or late-type galaxies. Early type galaxies lacked disc and were more elliptical. Late-type galaxies had discs and were further classified into with-bar and without a bar (Figure 1.5). At that time, it was thought that early-type galaxies with smoothed out and less complicated structures evolve to form more complex-looking spiral galaxies.

Late types are actively forming stars, have a prominent disc component and cold HI gas and comparatively less massive than the early-type galaxies. They have a young stellar population that has their emission in visible light dominated by the blue part of the spectrum. Early type galaxies have stopped forming stars and are ellipsoidal. They contain little cold gas. These galaxies appear red, as their emission is dominated by the old stellar population (Humason, 1936; Strateva et. al. et al., 2001).

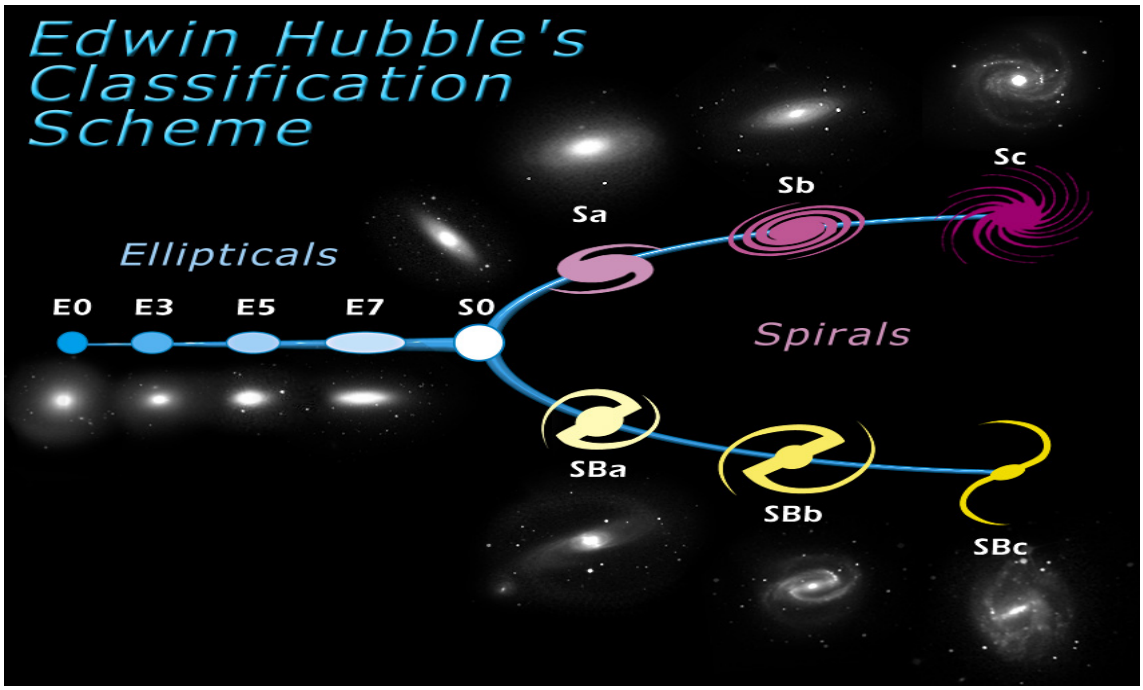

Figure 1.5: Hubble tuning fork diagram: Galaxies were classified based on their morphology. Figure Credit: SDSS

Ellipticals are classified by the apparent ellipticity. Spirals are classified by the prominence of the spiral arms, and the presence of bars. Transition class between ellipticals and spirals are the S0 galaxies, also called lenticulars.

1.4.2 Star formation in galaxies

Star formation takes place in molecular clouds, which are dense and cold gas clouds found mostly in the inner parts of galactic discs such as spiral arms (Heyer & Terebey, 1998). These regions are called Giant Molecular Clouds (GMCs). They have masses in the range $10^4 - 10^6$ $M_\odot$ with a typical size ranging from $5 - 200$ pc (Murray, 2011). Densities in GMC are such that it shields the center of the cloud from UV photons, shielding molecules from photodissociation. This process is called *self-shielding*. Therefore, GMCs are very rich in molecular hydrogen, CO and HCN molecules at the temperature of order $\sim 10 - 100$ K.

Inside each cloud, star formation takes place in a very structured way. New stars originate inside pre-stellar cores of size ~ 0.05 pc and $n_{H_2} \sim 10^5$ cm^{-3}. They are embedded into dense cores of size ~ 0.1 pc and $n_{H_2} \sim 10^4$ cm^{-3} (Bergin & Tafalla, 2007). The dense cores reside in a molecular cloud that can be part of a GMC. When their gas density reach is high enough, pre-stellar cores give rise to new stars of mass following an *Initial Mass Function (IMF)* (e.g. Salpeter, 1955; Kroupa, 2001; Chabrier, 2003).

OB stars have a very strong UV radiation that dissociates molecules, preventing the formation of other stars in their vicinity. Around 10% mass of stars created in the pre-stellar core resides in stars having mass more than 10 $M_\odot$. These stars are short-lived and explode in a supernova within ~ 10 Myr, re-injecting metals and energy ($E \sim 10^{51}$ ergs) back into the ISM. A fraction of this energy is radiated away while a significant amount of kinetic energy is released into the ISM, maintaining a

level of turbulence (de Avillez & Breitschwerdt, 2007) and cause the galactic winds and formation of superbubbles (Springel & Hernquist, 2003; Dubois & Teyssier, 2008). The cooling rate of ISM to from stars depends strongly on the abundance of metals in the ISM.

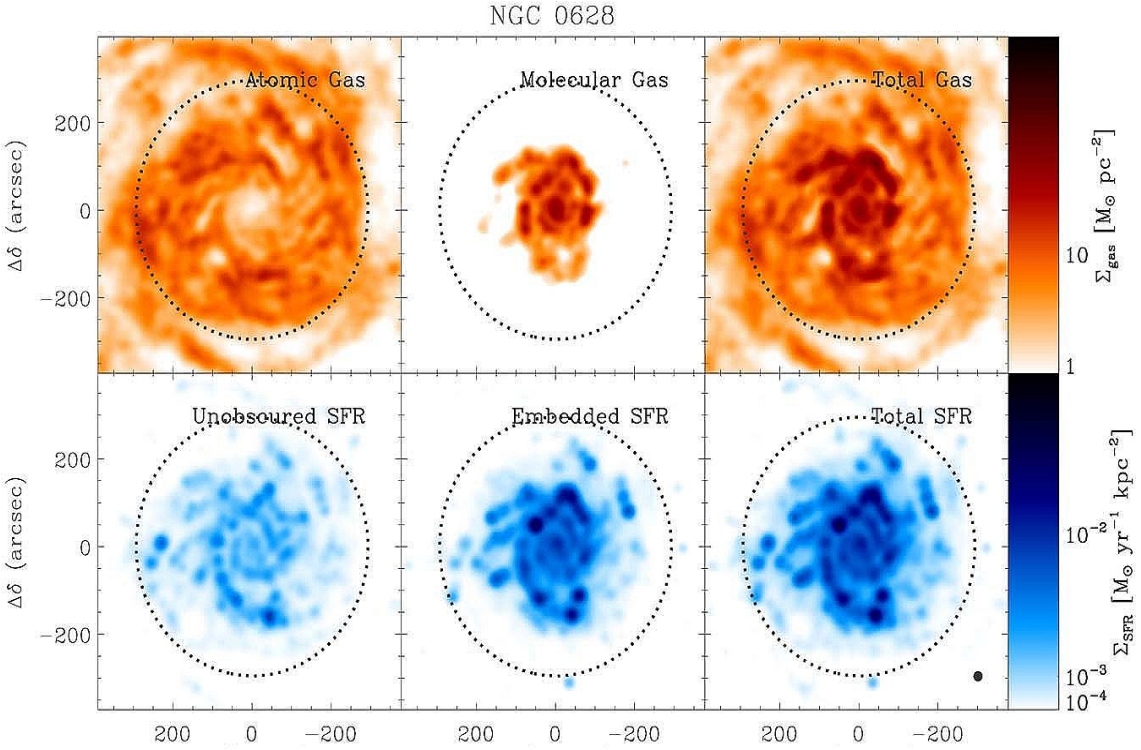

Figure 1.6: Observed maps of atomic, molecular and total gas (top-row) and derived star-formation rate (bottom row) for galaxy NGC0628. The star formation rate strongly follows molecular gas distribution. Image source: Leroy et al. (2008)

Star formation at galactic scales

Schmidt (1959) observed a scaling relation between the star formation rate and the density of gas. Based on observations Kennicutt (1989, 1998a) gave the so-called Kennicutt-Schmidt relation, linking the total (atomic and molecular) gas surface density with the star formation rate surface density:

$$\Sigma_{\rm SFR} = (2.5 \pm 0.7) \times 10^{-4} \left(\frac{\Sigma_{\rm gas}}{1\ M_\odot\ pc^{-2}} \right)^{(1.4 \pm 0.15)} M_\odot\ yr^{-1}\ kpc^{-2} \qquad (1.95)$$

As expected the star formation rate surface density seems more correlated with molecular gas surface density (Bergin & Tafalla (2007) and Figure 1.6).

1.4.3 Effects of the environment on galaxy properties

In Section 1.3.4, we saw that the large-scale environment consists of field, filaments, and clusters. Simplest measurable properties of galaxies for an optical survey like the SDSS are, the absolute magnitude M_r, the $g - r$ colour of galaxies, and the

physical half-light radius r_{50} (also called the "effective radius"). These properties reveal a variety of correlations, most known for many years, but now quantified much more precisely.

The effect of a galaxy's environment on its properties was revealed by a few key observations. In early observations of a cluster of galaxies, it was realised that these clusters of galaxies contain thousands of galaxies and center of clusters, and groups have massive elliptical galaxies surrounded by lenticular galaxies (Zwicky, 1938, 1951; Oemler, 1974; Dressler, 1980; Postman & Geller, 1984). Butcher & Oemler (1978a,b) found that the fraction of blue galaxies in two rich clusters at intermediate redshift was significantly higher than in a similar sample of low redshift clusters.

Studies of clusters and groups at $z \sim 0$ have shown that outskirts of groups and clusters (Zabludoff & Mulchaey, 1998; Rines et al., 2005; Wang et al., 2004; Cortese et al., 2007; Tran et al., 2009; Gavazzi et al., 2010; Smith et al., 2010; Sun et al., 2010; Coppin et al., 2011; Mahajan et al., 2012a; Verdugo et al., 2012; Mahajan, 2013) and filaments of galaxies (Porter & Raychaudhury, 2007a; Boué et al., 2008; Fadda et al., 2008a; Porter et al., 2008a; Edwards et al., 2010a; Biviano et al., 2011) are favourable sites for galaxy transformations.

Most studies in early years of development of photography of galaxy environments were mixing several effects. Later studies showed that stellar mass functions of galaxy clusters are different than the field (Balogh et al., 2001; Lin et al., 2004, 2017). It was also found that the morphology of galaxies had a trend with the stellar mass regardless of the environment (Allen et al., 2006; Bamford et al., 2009). Therefore, if one compares morphologies as a function of environmental density without removing the stellar mass difference, it leads to a correlation.

We can summarize some of the important results relating to the properties of galaxies in a large-scale environment in the following points:

- At low redshift, morphology at fixed stellar mass does show density dependence (Bamford et al., 2009; van der Wel et al., 2010; Cibinel et al., 2013; Erfanianfar et. al., 2014; Allen et al., 2016). Morphology is difficult to study at higher redshifts, but it indicates weaker trends with stellar mass.

- Red fraction or passive fraction, at fixed stellar mass increases from low-density field environment to high-density groups and clusters environments at low redshift (Weinmann et al., 2006a; Baldry et al., 2006; Kimm et al., 2009; Tinker et al., 2013; Hennig et. al., 2017; Wen & Han, 2018). At higher redshifts ($z \sim 1$) this trend continues, but the difference between the environments becomes smaller.

- The population of galaxies in groups at low redshift has early-type galaxies and passive fractions between those of clusters and field environments (Hansen et al., 2009; Kimm et al., 2009; Wen & Han, 2018).

1.5 Physical Processes in large-scale environments

We discussed in the previous section, the effects of the large-scale environment on the properties of galaxies. To understand these findings, one has to know that physical processes that are at play in these dense environments. We briefly describe some of the processes known to influence galaxy evolution in such environments.

1.5.1 Galaxy interactions

The formation of the large-scale structures proceeds via hierarchical structure formation, galaxies merge with each other. However, much of the understanding of timescales involved in these processes and the transformation of properties of merging galaxies are drawn from numerical simulations. Early N-body simulations showed that the merging of two late-type spiral galaxies produces early-type galaxies (Toomre & Toomre, 1972; Barnes & Hernquist, 1992; Rodriguez-Gomez et al., 2017; Martin et al., 2018).

The stars and dark matter are essentially collisionless because the mean distances between them are large compared to their cross-section. The relative speeds when galaxies merge are supersonic, causing shock waves (Mihos & Hernquist, 1996; Barnes & Hernquist, 1996). These shocks undergo a burst of star formation, which may lead to fueling the central AGN, triggering the "quasar" mode and quenching future star formation (Kauffmann & Haehnelt, 2000; Hopkins et al., 2006).

If mergers are responsible for trends we observe, then there is an expected increase in the merger rate in high-density environments. Numerical simulations and recent observations have shown that in such environments, galaxies have a highly active merger history (Gottlöber et al., 2001b; Fakhouri & Ma, 2009; Kampczyk et. al. , 2013). However, according to semi-analytical models merger rates in galaxy groups and clusters are not enough to explain environmental correlations (Bundy et al., 2009).

The importance of mergers in shaping galaxy properties is complicated by the simulation results that gas-rich mergers can lead to spiral galaxies (Hopkins et al., 2009; Stewart et al., 2009). In a dense environment like a cluster, galaxy mergers become ineffective when the velocity of the approach of the colliding galaxies becomes larger than their internal velocity dispersions.

1.5.2 Galaxy harassment

If the galaxies are moving towards each other at high speeds, they may not end up merging. This interaction can heat the gas and disturb orbits of stars, a mechanism which is known as *galaxy harassment* (Moore et al., 1996). Such events occurring repeatedly can lead to a modification in the morphology of disc galaxies into spheroidal in shape (Moore et al., 1998).

If we assume the perturbing mass ($m_{\rm perturb}$), after using impulse approximation, the energy imparted during galaxy harassment is given by (Spitzer, 1958):

$$\xi_{\rm harass} \propto \rho_{\rm gal} m_{\rm perturb}^2 \tag{1.96}$$

Assuming that mass of the perturber, $m_{\rm perturb}$, is tidally limited than the mass varies linearly with the radius of cluster ($m_{\rm perturb} \propto r_{\rm cluster}$). Galaxy density scales as $\rho_{\rm gal} \propto r_{\rm cluster}^{-2}$. Putting this in equation (1.96), we get that the efficiency of harassment should be independent of cluster centric radius. Observations, on the other hand, suggest that the effect of the environment has a radial variation (Balogh et al., 2000; Ellingson et al., 2001; Hansen et al., 2009; Allen et al., 2016; Woo et al., 2017).

1.5.3 Ram Pressure Stripping

As we had discussed earlier, baryons follow the dark matter in structure formation. When gas starts falling inside dark matter halos, it gets heated up. For smaller halos, this temperature is not very high, and the gas can cool down in what is known as *hot mode accretion* on to a disc and starts forming stars. In massive halos, this gas is so hot that it can not cool, and thus it resides as a hot dense gas which emits in X-ray wavelengths (Forman et al., 1972; Cavaliere & Fusco-Femiano, 1976; Pacaud et. al., 2016). A galaxy that is moving inside the cluster interacts with this gas and experiences a drag force on it (Gunn & Gott, 1972). If this drag force can overcome the gravitational pull, then cold gas from the disc of the galaxy gets stripped, quenching the star formation. This is known as *ram pressure stripping*.

Recent observations of galaxies falling into the clusters like Virgo and Coma support this as a dominant mechanism. Galaxies inside these clusters appear to have truncated HI gas discs while stellar discs remain undisturbed (Kenney & Koopmann, 1999a; Vollmer et al., 2004; Bösch et al., 2013). Using satellite galaxies in SDSS catalog Pasquali et al. (2019) found that star formation in them quenches at a fast rate (pointing to ram pressure stripping) or is pre-processed in a cluster environment.

We will discuss this in detail in chapter 2, where we try to propose an analytical model to study this mechanism and its effect on galaxy evolution.

1.5.4 Strangulation

Star formation in galaxies takes place when gas fragments and collapses under gravity. As discussed in the previous section, hot gas slowly collapses onto the disc. This hot gas acts like a reservoir that fuels star formation in the galaxies (White & Rees, 1978; White & Frenk, 1991). This reservoir gets replenished by gas that is ejected from the disc by feedback processes like a supernova. If this gas is removed, star formation in the galaxy can continue only for a short span (Kennicutt, 1998a). In a group environment, ram pressure may not be strong enough to strip gas out of the galactic disc. However, there may occur a scenario that the hot gas is removed by some mechanism. This process it is known as *strangulation*.

There have been many semi-analytical studies that used strangulation as the standard technique to account for environmental effects (Larson et al., 1980a; Balogh et al., 2000; White & Frenk, 1991). Bahé & McCarthy (2015) analysed 2000 galaxies in the GIMIC cosmological hydrodynamical simulations. They found that stripping causes at most half the loss of gas halos surrounding our simulated satellites. This suggests stripping as the main process and not the strangulation. However, recently, Hahn et al. (2017) in a semi-analytical study found that compared to satellite galaxies, central galaxies take ~ 2 Gyr longer to quench star formation. For the central galaxy, quenching timescale compares well with the timescale of strangulation in a group environment.

1.6 Filament as an environment

The role of the large-scale environment in modulating the evolution of galaxies has been well established in the literature (Dressler et al., 1997; Binggeli et al., 1988; Kauffmann et al., 2004; Weinmann et al., 2009; Peng et al., 2012; Boselli et al.,

2016). While interactions with the ambient hot gas in dense environments such as clusters and groups can lead to a loss of cold gas from galaxies through ram-pressure stripping (Gunn & Gott, 1972), gravitational interactions between galaxies (Kewley et al., 2006; Sobral et al., 2015; Stroe et al., 2015), or harassment of low-mass satellite galaxies by a more massive counterpart (Moore et al., 1996) can quench formation of stars in intermediate and low-density environments.

Galaxies form and evolve on the cosmic-web: a complex network of intricately woven filaments and sheets of matter which intersect at the nodes, aka the clusters of galaxies (Bond et al., 1996). In section 1.3.4, we showed that the distribution of all matter on such a web-like structure is expected from the theory of structure formation (Zeldovich et al., 1982) even before it was observed. However, the impact of the cosmic-web on the properties of galaxies through their interactions with the large-scale environment is yet to be understood fully.

Simulations have confirmed that compared to clusters, a large fraction of all galaxies reside on large-scale filaments (e.g. see table 2 of Libeskind et al., 2018). So in order to understand the role played by the cosmic-web in the evolution of galaxies, it becomes critical to study the large-scale filaments and their influence on the properties of galaxies. The intra-filament medium (IFM) is expected to be at $10^5 - 10^7$ K, and over-dense by a factor of ~ 20 relative to the mean of the Universe (e.g. Cen & Ostriker, 1999; Croft et al., 2001). Hydrodynamical simulations show that the Bremsstrahlung brightness in the cosmic-web reaches at most 10^{-16} erg s^{-1} cm^{-2} $arcmin^{-2}$ (Dolag et al., 2006). Hence, while we overcome the technical challenges to observe the IFM directly, it is essential to study its impact on the galaxies residing therein by studying their properties.

Recent observations have revealed that baryons in galaxies add up to 10 % , another ∼10 % remains in the circumgalactic and intracluster medium (Persic & Salucci, 1992; Fukugita & Peebles, 2004; Shull et al., 2012). The rest of the baryons are expected to be residing in filaments as warm/hot intra-filamentary gas. Filament as a large-scale environment is poorly understood and is capable of accelerating galaxy transformation (Porter et al., 2008a; Haines et al., 2011a; Alpaslan et al., 2016a; Martínez et al., 2016; Kuutma et al., 2017). Studies at high redshift (Fadda et al., 2008a; Geach et al., 2011; Coppin et al., 2012; Darvish et al., 2014) as well as $z \sim 0$ (e.g. Porter et al., 2008a; Mahajan et al., 2010; Haines et al., 2011a; Alpaslan et al., 2016a; Kim et al., 2016; Kleiner et al., 2017; Kuutma et al., 2017) have now shown that the intermediate density environment prevalent in filaments do not just bridge the gap between the dense interior of clusters and 'voids' devoid of galaxies, but play a rather important role in modulating galaxy observables. Owing to the highly coherent flow of galaxies along the filaments (González & Padilla, 2009), they have not just been observed at all wavelengths from ultraviolet (UV) (Gallazzi et al., 2009; Geach et al., 2011; Coppin et al., 2012) to infrared (Fadda et al., 2008a; Haines et al., 2008) by direct methods such as quantifying the distribution of galaxies, thermal Sunyaev-Ze'ldovich (tSZ) effect (Bonjean et al., 2018) and weak gravitational lensing (Dietrich et al., 2012; Jauzac et al., 2012), but also indirectly using a bent double lobe radio source (Edwards et al., 2010b).

Recently, filaments, in particular, the warm-hot intergalactic medium (WHIM) in filaments has been the focus of several studies. Using emission in the soft x-ray bands, such studies estimate the WHIM temperature in filaments to be ∼0.3–0.8 keV (Eckert et al., 2015; Akamatsu et al., 2017; Parekh et al., 2017; Tanimura

et al., 2019). Furthermore, the cosmic microwave background map from the Planck together with the Canada France Hawaii Telescope Lensing Survey, as well as the Two-Micron All-Sky Redshift Survey of galaxies suggest that at least half of the missing baryons in the Universe may reside as WHIM in large-scale filaments tracing the dark matter distribution (Van Waerbeke et al., 2014; Génova-Santos et al., 2015).

1.7 Hydrodynamical simulations

We discussed the Euler's equations for adiabatic case in equation (1.15) and equation (1.16). They describe the evolution of quantities in at some fix location, say $\vec{r}$. This approach for description of a fluid is called *Eulerian* and the derivative $\frac{\partial}{\partial t}$ tells us changes occurring at position $\vec{r}$ as fluid passes through it. Another approach for description of fluid motion is what is traditionally called *Lagrangian*. In this approach we employ the moving coordinates of a fluid element defined by the instantaneous coordinates of its radius vector $\vec{r}$. Lagrangian derivative $\frac{d}{dt}$ tells us about variation in the quantities pertaining to a fluid element as it moves in space. Using these definitions one can easily show that:

$$\frac{d}{dt} = \frac{\partial}{\partial t} + v_j \frac{\partial}{\partial r_j} \tag{1.97}$$

Hydrodynamical simulations in recent years have contributed extensively to our understanding of the Universe. They use both kinds of descriptions to study tough problems dealing with high dynamic ranges of density and various physical processes at play at the sub-grid level.

In this thesis work, we have directly or indirectly made use of two codes `RAMSES` (Eulerian code), which will be discussed further in chapter 5 and Gadget-3 (Lagrangian code, used for running EAGLE simulation) which we will very briefly discuss in chapter 4. In the following section, we briefly touch upon the differences in the two approaches and their advantages.

1.7.1 Smooth Particle Hydrodynamics

At microscopic level in fluids, atoms and molecules collide with each continuously frustrating the ballistic trajectories of particles in a space and time dependent gravitational field. At the macroscopic level, all of this chaotic motion leads to a force on each *fluid particle* (collection of many molecules) that is proportional to the sum of the local pressure gradient and the gradient of the potential. For a fluid particle the equations that describe its motion are:

$$\frac{d\vec{r_i}}{dt} = \vec{v_i} \tag{1.98}$$

$$\frac{d\vec{v_i}}{dt} = -\frac{\vec{\nabla} P_i}{\rho_i} - \vec{\nabla}\Phi_i \tag{1.99}$$

Here, P_i, Φ_i, ρ_i and $\vec{v_i}$ are the pressure, gravitational potential, density and velocity respectively at position $\vec{r_i}$.

Equations (1.98) and (1.99) can be solved numerically but one has to figure out how to calculate $-\frac{\vec{\nabla}P_i}{\rho_i}$, which poses the question of representing gradient of pressure at a single point. The main idea behind smooth particle hydrodynamics is to describe thermodynamic properties by a weighted average over neighbours:

$$\rho_j(\vec{r}) = m_j W\left(|\vec{r} - \vec{r}_j|\,; h\right) \tag{1.100}$$

Here ρ_j is the contribution to the density at $\vec{r}$ due to the particle j at $\vec{r_j}$ and W is called the *smoothing kernel* that is used to compute the weighted average. For visualization purposes one can use Gaussian (spherically symmetric) kernel:

$$W\left(|\vec{r} - \vec{r}_j|\,; h\right) = \frac{1}{h^3\pi^{3/2}} \exp\left[-\left(|\vec{r} - \vec{r}_j|\,/h\right)^2\right] \tag{1.101}$$

Here half width h associated with kernel is known as *smoothing length* which gives kernel a dimension of $(\text{volume})^{-1}$. Density at a point therefore, is calculated by summing up the contribution from all the particles (N) at $\vec{r}$ or at the position of another particle at i:

$$\rho(\vec{r}) = \sum_{j=1}^{N} \rho_j(\vec{r}) \tag{1.102}$$

As one can see the contribution to density at a position will be from nearby particles. The kernel are chosen such that they must satisfy:

$$\int_0^\infty W\left(|\vec{r_j} - \vec{r}|\,; h\right) d\vec{r} = 1 \tag{1.103}$$

and

$$\lim(h \to 0) W\left(|\vec{r} - \vec{r}_j|\,; h\right) = \delta_{\mathrm{D}}\left(\vec{r} - \vec{r}_j\right) \tag{1.104}$$

Here δ_{D} is dirac delta. This equation maintains the normalization of equation (1.103).
Other physical quantities (A) like pressure and temperature are calculated using weighted average of known values for the particles as:

$$A(\vec{r}) = \sum_{j=1}^{N} m_j \frac{A_j}{\rho_j} W\left(|\vec{r} - \vec{r}_j|\,, h\right) \tag{1.105}$$

As previously pointed we still require $\vec{\nabla}P_i$ which demands that we must be able to calculate derivatives in SPH approach. Hernquist & Katz (1989) showed that derivatives of physical quantities can be calculated using derivatives of kernel itself. Therefore, $\vec{\nabla}P_i$ can be calculated as:

$$\vec{\nabla}P(\vec{r}) = \sum_{j=1}^{N} m_j \frac{P_j}{\rho_j} \vec{\nabla} W\left(|\vec{r} - \vec{r}_j|\,, h\right) \tag{1.106}$$

Here derivative is calculated at $\vec{r}$.

The sum in principle needs to be carried out for all the particles, but to minimise computational cost, the kernel shape is chosen to limit this sum to finite neighbours.

We will discuss this further in section 1.7.1. Using all the machinery discussed above, one can write down the basic elements of an SPH hydro-code:

- Initial condition must provide positions, velocities and masses from which density is assigned using equation (1.102).
- A method should be in place for calculating P_i and $\vec{\nabla} P_i$.
- An equation of state relating P_i and ρ_i.
- A time integration scheme for updating positions and velocities using equation (1.98) and (1.99).
- A method for calculating smoothing length h. It scales as:

$$h = \frac{h_0}{< \rho >^{1/3}} \tag{1.107}$$

  Here h_0 is a constant and $< \rho >$ is average density:

$$< \rho >= \frac{1}{N} \sum_{i=1}^{N} \rho_i \tag{1.108}$$

In the simplest SPH codes, these can be addressed using simple techniques. h is the same for particles and h_0 is chosen such that a reasonable number of particles reside inside a smoothening length. The codes proceed in two steps: first density is calculated, and then other properties like pressure gradient and gravitational force, new position, and velocities are calculated. What we have discussed so far is a very rudimentary implementation and many optimisations have been proposed and used, we will briefly describe some of these improvements in what follows.

Kernels

If we assign a spherically symmetric kernel with infinite support at every point, each particle contributes to density at every point. The computation of quantities is computationally expensive as one has to sum over all the particles. One can thus work with a kernel that has a finite support. One such kernel was proposed by Monaghan & Lattanzio (1985), given by:

$$\begin{aligned} W(r,h) &= \frac{1}{\pi h^3}\left[1 - \frac{3}{2}(r/h)^2 + \frac{3}{4}(r/h)^3\right] \quad 0 \le r/h \le 1 \\ W(r,h) &= \frac{1}{4\pi h^3}[2 - (r/h)]^3 \quad 1 \le r/h \le 2 \\ W(r,h) &= 0 \quad r/h \ge 2 \end{aligned} \tag{1.109}$$

Here $r = |\vec{r} - \vec{r_j}|$. This kernel goes to 0 at a distance of $2h$.

Combining SPH with Tree Code

Dark matter and stars in hydrodynamical codes used in cosmology are treated as collision-less particles. Their dynamics are well studied using what are called TreePM Methods (Bagla, 2002; Khandai & Bagla, 2009; Ishiyama et al., 2009). These codes use division of space into different octants to approximate gravitational potential with reasonable accuracies. The gravitational potential is softened by a parameter called *softening length*(ϵ), which is not the same as the smoothing length.

One can use the same structure for SPH particles as collision-less particles as these are fully Lagrangian as well. It is best to use $\epsilon = h$, which makes sure that numerical resolution of both gravity and pressure remains the same. Thus, one takes advantage of flagging the SPH particles inside $2h$ while traversing the tree for computing gravitational potential. The tree is combined with SPH, mostly with variable smoothing length.

Variable smoothing length

In most astrophysical applications, there is a huge range of density in the system of interest. Having a constant smoothing length thus creates a problem. It is convenient to use a variable smoothing length with each particle given its own smoothing length (h_i) that contains the same number of neighbours ($N_{\rm target} \sim 50$).

What we have discussed so far is the simplest case with a barotropic equation of state ($P = P(\rho)$), but in general, the equation is a function of both density and internal energy per unit mass. Therefore, in addition to Euler's equation, one has an energy equation. In addition to this, one has different heating and cooling processes at play in a modern SPH code like Gadget-3, used for running the simulation used in chapter 4.

1.7.2 Eulerian Approach

Hydrodynamical processes in Eulerian approach are governed by the Euler equations. A compressible inviscid self-gravitating flows can be modeled as an ideal fluid which is insensitive to heat transfer. Flow of such a fluid is given by following conservation equations:

$$\text{mass}: \quad \frac{\partial \rho}{\partial t} + \vec{\nabla} \cdot (\rho \vec{v}) = s_{\rm m} \tag{1.110a}$$

$$\text{momentum}: \quad \frac{\partial (\rho \vec{v})}{\partial t} + \vec{\nabla} \cdot (\rho \vec{v} \otimes \vec{v}) + \vec{\nabla} P = -\rho \vec{\nabla} \Phi + \vec{s_{\vec{p}}} \tag{1.110b}$$

$$\text{energy}: \quad \frac{\partial (\rho e)}{\partial t} + \vec{\nabla} \cdot ((\rho e + P) \vec{v}) = -\rho \vec{v} \cdot \vec{\nabla} \Phi + s_{\rm e} \tag{1.110c}$$

Here ρ is density, Φ is the gravitational potential, P is the pressure , $\vec{v}$ is local fluid velocity calculated with respect to fixed grid (Eulerian velocity)and energy density e can be calculated using:

$$e = \left(\frac{1}{2} |\vec{v}|^2 + u \right) \tag{1.111}$$

Here u is local internal energy density.

To solve the set of equation one needs equation of state (EOS) given by:

$$P = \frac{\rho k_{\rm B} T}{\mu m_{\rm H}} = \rho(\gamma - 1)u \tag{1.112}$$

Here γ is $C_{\rm p}/C_{\rm v}$, μ is mean molecular mass, adiabatic constant of gas, $m_{\rm H}$ is mass of Hydrogen atom and $k_{\rm B}$ is Boltzmann constant.

If one assumes vanishing sources equations (1.110a)-(1.110c) can be written in the form:

$$\frac{\partial \mathbf{U}}{\partial t} + \nabla \cdot \mathbf{F}(\mathbf{U}) = 0 \tag{1.113}$$

Here $\mathbf{U} = (\rho, \rho\vec{v}, \rho e)$ is a vector with conserved quantities and $\mathrm{F} = (\rho\vec{v}, \rho\vec{v} \otimes \vec{v} + P, (\rho e + P)\vec{v})$ is the variable fluxes at boundaries of cells. One can use finite-volume method for finding solution to this conservation equation. We call finite volume in 1-D space: $[x_i, x_{i+1}]$ as cell. Cell boundaries are denoted by $x_{i+1/2}$. Equation (1.113) when written in 1-D space x_i becomes:

$$\frac{\mathbf{U}_i^{n+1} - \mathbf{U}_i^n}{\Delta t} + \frac{\mathbf{F}_{i+1/2}^{n+1/2} - \mathbf{F}_{i-1/2}^{n+1/2}}{\Delta x} = 0 \tag{1.114}$$

Here $\mathbf{U}_i$ is average value of $\mathbf{U}(x,t)$ in the . It is given by:

$$\mathbf{U}_i(t) = \frac{1}{\Delta x} \int_{x_{i-1/2}}^{x_{i+1/2}} \mathbf{U}(t_n, x) dx \tag{1.115}$$

Now the problem reduces to finding the values of the fluxes $\mathbf{F}_{i-1/2}$ and $\mathbf{F}_{i+1/2}$ at the edges of the cell i. Using Godunov scheme for solving such a system of equation, one needs to solve the Riemann problem (discontinuity) at each cell edge. If at the start each edge separates a left state $\mathbf{U}_{i+1/2}^L = \mathbf{U}_i$ and a right state $\mathbf{U}_{i+1/2}^R = \mathbf{U}_{i+1}$. We can write intermediate state $\mathbf{U}_{i+1/2}^*(x/t)$ and Flux can be written as:

$$\begin{aligned} \mathbf{U}_{i+1/2}^*(x/t) &= \mathcal{RP}\left[\mathbf{U}_i^n \mathbf{U}_{i+1}^n\right] \\ \mathbf{F}_{i+1/2}^{n+1/2} &= \mathbf{F}\left(\mathbf{U}_{i+1/2}^*(0)\right) \end{aligned} \tag{1.116}$$

This leads to Godunov Flux, defined by:

$$\mathbf{F}_{i+1/2}^{n+1/2} = \mathbf{F}^*\left(\mathbf{U}_i^n, \mathbf{U}_{i+1}^n\right) \tag{1.117}$$

One has to calculate the initial states at the interface. Godunov (1959) proposed first order spacial interpolation method. This method is more diffusive and does not resolve shocks really well. Higher-order reconstruction of $U(x,t)$ within the cell called *MUSCL (Monotone Upstream-centered Schemes for Conservation Laws)* scheme was introduced by van Leer (1979), in which piecewise-linear interpolation (Piecewise Linear Method) was proposed. This method had second order accuracy in space, much less diffusive but depended on *slope limiter* for avoiding artificial oscillations in the solutions. Colella & Woodward (1984) gave a scheme called Piecewise Parabolic Method (PPM) which was third order accurate in space.

1.8 Goals and outline of the thesis

In this thesis, we present the study of the effects of the large-scale environment on galaxy properties. We utilise different techniques from analytical models, multi-wavelength data from large surveys, and hydrodynamical simulations to explore the dependence of galaxy properties on its environment.

In chapter 2, we present an analytical model to study ram pressure stripping in different environments. We vary various parameters related to the in-falling galaxy and environment to study their effects on stripping of gas from the disc of the galaxies.

In chapter 3 we present study of large-scale filament environment in Coma-supercluster. We classify the environment into the field, filament and group, and cluster environments. We use ultraviolet and optical data to do a statistical study of star formation galaxies in different environments.

In chapter 4 we extend the methodology developed in chapter 3 to study properties of galaxies in EAGLE simulation. We try to compare our results with previous works and observations.

In chapter 5 we perform a hydrodynamical simulation of the merger of two galaxies and study evolution of star formation and quenching.

We conclude this thesis in chapter 6 and also discuss the future works using the studies done in this thesis.

Chapter 2

Ram Pressure: An analytical approach

This chapter is based on Singh, A., Gulati, M. and Bagla, J. S. "Ram pressure stripping: An analytical approach", 2019, *MNRAS, 489, 5582*

2.1 Introduction

Observations point to a lack of gas-rich galaxies in clusters. To explain the absence of gas-rich galaxies in the clusters, Gunn & Gott (1972) proposed the mechanism of ram pressure stripping (RPS). A galaxy falling in a cluster experiences a wind as it moves through the Intra-Cluster Medium (ICM). If the gravitational force between the stellar and gas disc is less than the force due to the wind, then the gas will be stripped. The condition for gas loss is given by:

$$\rho_{\rm ICM} V_{\rm in}^2 > 2\pi G \Sigma_s \Sigma_g \tag{2.1}$$

Here, the right-hand side is a gravitational restoring pressure with $\Sigma_{\rm s}$ being the surface density of stars and $\Sigma_{\rm g}$ is the surface density of the gas, the density of ICM is $\rho_{\rm ICM}$, and the in-fall velocity of the galaxy is given by $V_{\rm in}$. This condition, on putting numbers for spirals galaxies, led them to conclude that a spiral galaxy should lose its gas disc while passing through the centre of a cluster.

It is observed (Gómez et al., 2003a; Hogg et al., 2003; Goto et al., 2006; Verdugo et al., 2008; Park & Hwang, 2009; von der Linden et al., 2010; Wetzel et al., 2012; Fillingham et al., 2016) that cluster centres contain galaxies with early-type morphologies and have star formation rates that are much lower than that of field galaxies with a similar luminosity. Low star formation rates (SFR) is due to deficiency of cold gas in these galaxies (Gavazzi et al., 2006). Observations of different clusters (Giovanelli & Haynes, 1983; Bravo-Alfaro et al., 2000; Solanes et al., 2001; Chengalur et al., 2001) have shown the presence of lenticulars and HI deficient spirals. Solanes et al. (2001) and Lah et al. (2009) observed an increase in deficiency with decreasing distance from the cluster centre and that the galaxies which are HI deficient tend to have highly eccentric orbits.

Cayatte et al. (1994) observed signatures of gas stripping in galaxies in Virgo cluster. The inner discs of the galaxies have normal gas densities but are sharply

truncated when compared to field galaxies of similar morphology. In a study of more Virgo spirals, Kenney & Koopmann (1999b) and Kenney et al. (2004a) observed NGC4522 to have heavily truncated HI disc with one side containing extraplanar Hα and HI, but the stellar disc is undisturbed. Kenney et al. (2004b) observed IC3392, NGC4402, NGC4388 and NGC4419 to have a truncated HI disc. An undisturbed optical disc with an extraplanar gas component in these galaxies indicates the interaction of galaxy with the ICM. Interestingly one finds a positive correlation between the star formation of the central galaxy and its satellite for the regions extending far beyond virial radius (Weinmann et al., 2006b; Ann et al., 2008), a phenomenon known as 'galactic conformity'. Brown et al. (2017) performed a multi-wavelength study taking data from Sloan Digital Sky-Survey (SDSS) and Arecibo Legacy Fast ALFA (ALFALFA) survey. They observed that gas suppression in a high-density environment begins at the group level. They conclude that the amount of gas suppression cannot be because of a slow process like starvation or strangulation (Larson et al., 1980b), and a fast process like ram pressure stripping is needed to explain the observations. Recently, Treyer et al. (2018) have shown that the low star formation activity in the group environment at low redshift owing to the environmental quenching processes. It is believed that the stripping acts at two levels in the group environment. First, the dwarf galaxies with lower mass having lower restoring force may be stripped. Second, the massive spirals may lose outer parts of their gas discs as the restoring force is low in these regions.

Boselli et al. (2018) observed star-forming regions up to 20 kpc outside the optical disc of the galaxy NGC4285. These regions are located along with a tail of HI gas stripped from the disc of the galaxy. Such galaxies are called jellyfish galaxies. Jaffé et al. (2018), in a recent compilation of jellyfish galaxies in low-redshift clusters from the WINGS and OmegaWINGS surveys, and follow-up MUSE observations from the GASP MUSE programme investigated the orbital histories of jellyfish galaxies in clusters and reconstructed their stripping history. They found that the jellyfish galaxies seen in clusters likely formed via fast, incremental, outside-in ram-pressure stripping during first infall into the cluster in highly radial orbits. On-going ram pressure stripping in three new intermediate-mass irregular galaxies in the north-west outskirts of the nearby cluster of galaxies Abell 1656 (Coma cluster) is shown by Gavazzi et al. (2018).

Systems with a galaxy passing through the medium have been simulated to confirm the Gunn and Gott condition for gas stripping. Simulations studying ram pressure have been done in broadly three types of settings: wind tunnel (Gisler, 1976; Balsara et al., 1994; Quilis et al., 2000; Tonnesen & Bryan, 2009; Close et al., 2013; Weinberg, 2014; Bischko et al., 2015), simple systems (Roediger & Brüggen, 2007; Kapferer et al., 2008, 2009) and cosmological simulations (Vollmer et al., 2001; Tonnesen et al., 2007; Simpson et al., 2018). Roediger & Hensler (2005) in their simulation with lower ram pressure observed that large and medium-sized model spirals have their outer HI disc stripped. Marcolini et al. (2003) in their simulation of a dwarf-like galaxy in the group environment found that it will be stripped of its gas. The observational evidence of such a system is circumstantial. In the case of local group dwarfs Blitz & Robishaw (2000) observed that the star formation history correlates well with their distances from the dominant spirals.

Morphological transformation of galaxies due to ram pressure is seen in simulations, though studies indicate that this in itself is not adequate to explain the

observations (Abadi et al., 1999). The process of stripping is also found to have two stages. The first stage is rapid stripping due to the ram pressure and in the second stage the rest of the gas is slowly stripped viscously (Quilis et al., 2000; Schulz & Struck, 2001; Marcolini et al., 2003; Roediger & Hensler, 2005). Roediger & Hensler (2005) performed simulations to study the dependence of the stripping radius on the speed of ICM wind velocity and vertical structure of the galaxy. Their results confirm that the most important factors are the surface density of the disc and the ram pressure. The vertical structure of the disc and Mach number have a little role to play in stripping. The Gunn and Gott condition predicts the stripping radius fairly well.

While both simulations and observations seem to strongly suggest that ram pressure stripping is a key quenching mechanism in the cluster environment, along with few relevant studies for groups, its role in the group and galactic environments are still not clear. Although there is strong evidence for the presence of ram pressure stripping, the observations also seem to suggest that the observed relation of morphology and the environment may be contaminated by the presence of other processes as well. Since the galaxies residing in the high-density environments formed earlier than their field counterpart having same luminosity, they are expected to be redder and have a lower star formation. Moreover, galaxies in high-density environments are more prone to mergers (Gottlöber et al., 2001a) therefore, other quenching processes like harassment could also play a role. Another process that can be at play in these environments is strangulation, as there is no availability of the fresh gas and the halo gas of these galaxies gets stripped by heating up (Larson et al., 1980b). Thermal evaporation (Cowie & Songaila, 1977) may also be present along with these processes.

Ram pressure is expected to depend upon various parameters related to the infalling galaxy and environment. To identify the importance of ram pressure stripping as a quenching mechanism one needs analytical models where we may study the effects of various parameters on the amount of gas that gets stripped (Hester, 2006; Zinger et al., 2018). The basic aim of this work is to study the efficiency of ram pressure to remove the gas from a galaxy passing through an environment (cluster, group, and galactic) and its variation with galaxy and ambient medium parameters. Köppen et al. (2018) have recently given analytical treatment for ram pressure stripping based on pure kinematics of the system. However, they restrict there analysis to only cluster environment, and a detailed dependence of stripping on the system parameters is missing. Luo et al. (2016) have also studied the stripping of cold gas in satellite galaxies only in a cluster, though their model does not allow for gas fall back or accretion.

A simplistic approach of a face-on disc galaxy passing through a spherically symmetric medium is considered here. The properties of the environment and the galaxy passing through it will be discussed in details in section 2.2.1 and section 2.2.2. We begin with a galaxy modelled as a thin axisymmetric disc, passing through a spherically symmetric cloud of gas. In the first part, we assume the galaxy to have a radial trajectory and the infalling velocity profile, '$V(R_c)$' is explained in section 2.2.3. Non-radial trajectories for the infalling galaxies are also considered, details of which are discussed in section 2.2.3. We discuss the results of our numerical solutions for the model in section 2.3 for both radially infalling galaxies (section 2.3.1) and non-radial profiles for infalling galaxies (section 2.3.2). In section 2.3.3 we breifly

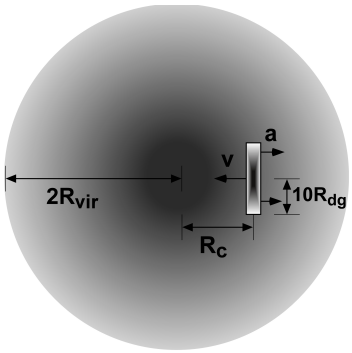

Figure 2.1: Schematic of our model. The background or the ambient medium is a spherically symmetric sphere of radius $2 \times R_{\rm vir}$, where $R_{\rm vir}$ is the virial radius as defined in equation 2.7. The galaxy at radius R_c in the medium is moving with velocity V, entering the medium face-on. The directions of velocity and acceleration, a (defined in equation 2.4) are as indicated in the figure. $R_{\rm dg}$ is the disc scale length of the galaxy (equation 2.14)

consider the effect of inhomogeneities in the infalling galaxy on the amount of gas stripped due to ram pressure. Conclusions and discussion is presented in section 2.4.

2.2 Our Model

A schematic of our model is shown in Figure 2.1, which we describe here. The galactic disc is divided in annuli of equal thickness and the force acting on each annulus while passing through the medium due to ram pressure is calculated at each instant. Prescription for ram pressure used in this work is similar to what is used by Gunn & Gott (1972):

$$F_{\rm ram}(R_c) = \rho(R_c)V^2(R_c) \tag{2.2}$$

where $\rho(R_c)$ is the matter density of the medium from which the galaxy is passing and $V(R_c)$ is the velocity of the galaxy relative to the medium, both measured as a function of the radius of the cloud. This force acts on the gas component of a given annulus at radius R, of the razor-thin disc, pushing it out. Ram pressure is countered by a restoring force per unit area due to the stellar component of the galaxy given by:

$$F_{\rm res}(R) = 2\pi G\Sigma_{\rm g}(R)\Sigma_{\rm s}(R) \tag{2.3}$$

where $\Sigma_{\rm g}$ and $\Sigma_{\rm s}$ are the surface densities of gaseous and stellar components of the disc, respectively as defined in section 2.2.2 where we give the properties of infalling galaxy. G is the gravitational constant. Thus the acceleration experienced by the gas per unit area is given by:

$$a(R_c, R) = \frac{F_{\rm ram}(R_c) - F_{\rm res}(R)}{\Sigma_{\rm g}(R)} \tag{2.4}$$

The acceleration on the disc annuli acts in the opposite direction w.r.t. the velocity of the galactic disc as shown in Figure 2.1 . If ram pressure dominates then the

Part I: Ambient medium			
Environment ↓	M (in $M_\odot$)	z	δ
Cluster	2×10^{15}	$0, 0.5, 1$	1.0
Group	$2 \times 10^{13.5}$	$0, 0.5, 1$	$1.0, 0.5$
Galactic	10^{12}	$0, 0.5, 1$	$0.1, 0.3$
Part II: Infalling galaxy			
Environment ↓	$M_{\rm gal}$ (in $M_\odot$)	λ	$V_{\rm in}/V_{\rm vir}$
Cluster	10^9to10^{13}	0.02, 0.04, 0.08	0, 0.5, 1.0
Group	10^6to10^{12}	0.02, 0.04, 0.08	0, 0.5, 1.0
Galaxy	10^6to10^{10}	0.02, 0.04, 0.08	0, 0.5, 1.0

Table 2.1: The table contains two parts. Top one are the values of parameters used in the study on which the background environment depends in all three cases: Cluster, Group, and Galactic. The second part contains the values the model parameters on which the infalling galaxy depends and there values used in different environments.

acceleration is positive, the gas component of the annulus is pushed out of the galactic plane. If a gas annulus has travelled more than one vertical scale height (z_d) above the disc plane, then it is considered as removed from the disc. Gas once removed from the disc is removed from the system, and we ignore the fall back of gas, the case of gas accretion to the galaxy.

Though our model allows for calculating the fall back of gas, the case of gas accretion to the galaxy, this happens when acceleration becomes negative. We do not calculate it here because once the stripped gas travels a distance more than z_d away from the disc it is sufficiently outside the galaxies gravitational pull to be accreted by the galaxy[1].

As the galaxy passes through the medium, the gas begins to strip, and the radius up to which the gas is stripped at a given R_c is noted and is called $R_{\rm strip}$ (which is a function of R_c).

2.2.1 Environment

This section contains a brief account of the properties of the background or the environment through which the galaxies pass. We consider three classes of the environment in the present study: cluster, group, and galactic. The background is modelled as a spherically symmetric cloud of gas. The radial profiles of dark matter and baryons are assumed to be the same for all the three cases, but with different total mass. The mass, M used for the cluster, group and galactic environment are 10^{15} $M_\odot$, $2 \times 10^{13.5}$ $M_\odot$ and 10^{12} $M_\odot$, respectively. Dark matter follows the NFW profile (Navarro et al., 1996):

$$\rho_{\rm NFW}(R_c) = \frac{\delta_c \rho_c}{(R_c/R_s)\,(1 + R_c/R_s)^2} \tag{2.5}$$

[1]The only exception to this is an annulus that is stripped near a turning point in the trajectory of the galaxy through the medium.

and

$$\delta_c = \frac{200}{3} \frac{c^3}{ln(1+c) - c/(1+c)} \tag{2.6}$$

ρ_c is the critical density of the Universe at the time when the halo forms and is given by $\rho_c = 3H^2(z)/8\pi G$, and $R_s = R_{\rm vir}/c$ is the scale factor. The factor $H(z)$ is calculated using the Friedmann equations, see, e.g., Peebles (1993). We use ΛCDM cosmology with $\Omega_k = 0.0$, $\Omega_\Lambda = 0.6911$, $\Omega_m = 0.3089$, $H_0 = 67.8$ (Planck Collaboration, 2016). The virial radius $R_{\rm vir}$ and the concentration parameter 'c' for a virialized halo (Duffy et al., 2008) of mass M are calculated using;

$$R_{\rm vir} = 0.784 \left(\frac{M}{10^8 h^{-1}\ {\rm M}_\odot} \right)^{1/3} \left[\frac{\Omega_m^z 18\pi^2}{\Omega_m \Delta_c} \right]^{1/3} \left(\frac{1+z}{10h^{-1}} \right)^{-1} kpc \tag{2.7}$$

$$c = \frac{6.71}{(1+z)^{0.44}} \left(\frac{M}{2 \times 10^{12}\ h^{-1}\ {\rm M}_\odot} \right)^{-0.092} \tag{2.8}$$

$$\Omega_m^z = \frac{\Omega_m (1+z)^3}{\Omega_m (1+z)^3 + \Omega_k (1+z)^2 + \Omega_\Lambda} \tag{2.9}$$

where $\Delta_c = 18.0\pi^2 + 82d - 39d^2$, $d = \Omega_m^z - 1.0$ and 'z' is the redshift of the collapse which is assumed to same for both ambient medium and infalling galaxy.

The radial distribution of gas inside the dark matter halo are assumed to follow Beta profile (King, 1962):

$$\rho_\beta(R_c) = \frac{\rho_{\rm g0}}{\left[1 + (R_c/R_{\rm core})^2\right]^{3\beta/2}} \tag{2.10}$$

where $R_{\rm core}$ is the core radius which we take to be one-tenth of the virial radius and $\rho_{\rm g0}$ is the central density. We take $\rho(R_c)$ (density of the ambient medium used in equation (2.2)) to be equal to $\rho_\beta(R_c)$. Beta model serves as a test case, it being centrally concentrated is a reasonable approximation (Cavaliere & Fusco-Femiano, 1976; Sarazin, 1986).

To calculate the value of central density, we find the ratio of the total gas mass gas ($M_{\rm g}$, say) and total dark matter mass ($M_{\rm bg}$, say) inside $R_{\rm vir}$ which is expressed as:

$$\Delta = M_{\rm g}/M_{\rm bg} = f_{\rm uni}\, \delta \tag{2.11}$$

where $f_{\rm uni}$ is the universal mass fraction taken to be 0.158 (Planck Collaboration, 2016) and δ is a parameter in our analysis, the value of which depends upon the environment. This parameter encodes the fraction of baryons retained in the form of hot gas. The value of β for equation (2.10) is taken to be equal to 0.6 (Ota & Mitsuda, 2002). δ varies from 1.0 for the case of cluster, 1.0 & 0.5 for groups to, 0.3 & 0.1 for the case of galaxy environment. We have tended to err on the higher side for choosing values of δ to simulate the worst-case scenario (Sharma et al., 2012). For a given value of Δ we solve equation (2.11) to get the value of $\rho_{\rm g0}$. In the first part of Table 2.1, we tabulate values of various parameters pertaining to the ambient medium used for the present work.

2.2.2 Infalling Galaxy

We discuss the geometry and properties of the infalling galaxies in this section. We assume the galaxy to be a thin axisymmetric disc entering face-on in the ambient

medium. The force being a vector quantity acts differently if the projections are taken into account. If the inclination is larger, the effect on the gas is expected to be compression in the front and stripping from edges on the side. Here stripping mechanism lead to different effects and needs to be modelled differently. Our analysis is applicable for inclinations up to 30° in which case the force on the face-on side dominates than the edge-on. This also leads to enhanced effect of RPS in our model. Mass of the galaxy (baryons + dark matter) is $M_{\rm gal}$ and the mass residing in the disc (M_d) is taken as:

$$M_{\rm d} = f_{\rm d}\, f_{\rm uni}\, M_{\rm gal} \tag{2.12}$$

where $f_{\rm d}$ is the gas mass fraction in the galaxy disc and is a parameter in the present work. Two values of $f_{\rm d}$ that we consider are 0.1 and 0.3 (Sharma et al., 2012). Out of this mass $M_{\rm d}$, 10% is assumed to be in gas and rest is in stars (these numbers are taken considering the Milky Way as a model, Binney & Tremaine (2008)). Radial profile of mass surface density of the galactic disc (baryonic) is assumed to be an exponential with different scale lengths for the gas and stellar components and is given by:

$$\Sigma_{\rm d}(R) = \Sigma_0\, exp(-R/R_{\rm d}) \tag{2.13}$$

where $R_{\rm d}$ is the scale radius of the disc. In the following, the scale radius for the gaseous component is referred to as $R_{\rm dg}$ and $R_{\rm ds}$ for the case of the stellar disc. The corresponding surface densities are written as $\Sigma_{\rm dg}$ and $\Sigma_{\rm ds}$, respectively.

We assume an isothermal profile for the dark matter halo of the infalling galaxy. This is done for ease of computation and the disc scale radius of the galaxy in this case is given by:

$$R_{\rm dg} = \frac{\lambda}{\sqrt{2}} 0.784 \left(\frac{M_{\rm gal}}{10^8 h^{-1} M_\odot}\right)^{1/3} \left[\frac{\Omega_m^z 18.0\pi^2}{\Omega_m \Delta_c}\right]^{1/3} \times \\ \times \left(\frac{1+z}{10h^{-1}}\right) kpc \tag{2.14}$$

where λ is the spin parameter[2] of the dark matter halo and the baryonic matter is assumed to share the same spin parameter. λ is also a parameter for the present study, and it is varied from $0.02 - 0.08$. The radial extent of galactic disc, $R_{\rm out}$ is taken to be $10 \times R_{\rm dg}$. The stellar disc scale radius is obtained by (Binney & Tremaine, 2008):

$$R_{\rm ds} = \frac{1}{2} R_{\rm dg} \tag{2.15}$$

Vertical scale height, $z_{\rm d}$ of the disc is taken to be 300 pc, which is the same as that for the Galaxy (Binney & Tremaine, 2008). It is kept at the same value for the galaxies of different masses throughout the present work. However, the present formulation is such that the conclusions are not expected to change if we take scale height to be a function of mass, as $z_{\rm d} = 300$ pc is the number for approximately the most massive galaxy used in our analysis and $z_{\rm d}$ is expected to decrease slowly for lower mass galaxies. Hence, this gives a reasonable estimate for $R_{\rm strip}$ for all masses

[2]The spin parameter is a dimensionless representation of the angular momentum of the Halo and is given by $\lambda = {\rm J|E|^{1/2}G^{-1}M^{-5/2}}$ where E is the total energy of the halo, M is the total mass of the halo, J is the total angular momentum of the halo and G is the gravitational constant.

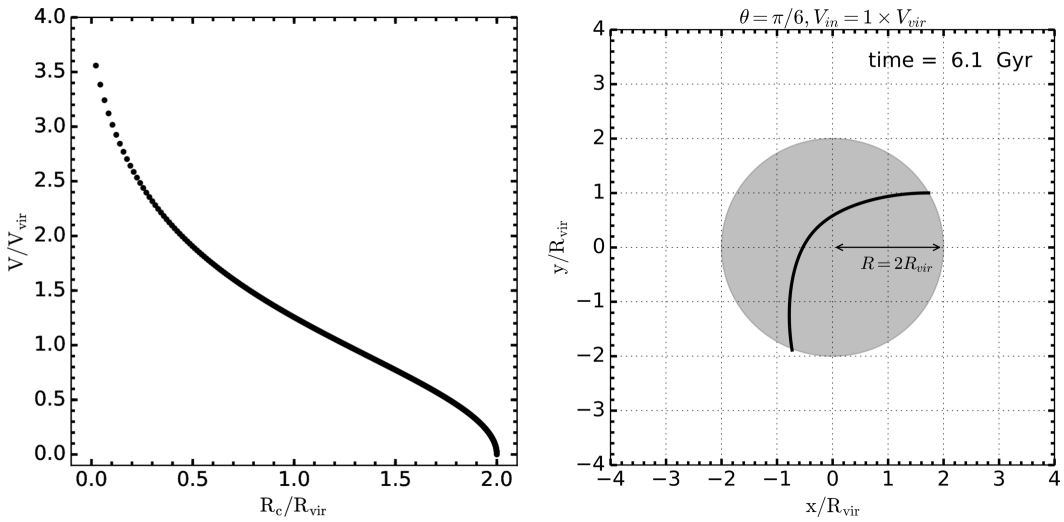

Figure 2.2: (left) Variation of velocity with R_c. The galaxy starts at zero velocity at $2 \times R_{\rm vir}$, which increases as it passes through the ambient medium. (right) The plot for the trajectory of an infalling galaxy for non-radial infall in the $x-y$ plane. The axis is normalised w.r.t. $R_{\rm vir}$ and all other parameters are given in the plot.

of infalling galaxies. To calculate Σ_0 for both gas and stellar disc we integrate their respective surface density profiles from zero to $R_{\rm out}$. This gives the total mass inside $R_{\rm out}$ and putting it equal to their respective masses we find the value of Σ_0 for both gas and stellar disc. These are referred to as Σ_{0g} and Σ_{0s}, respectively.

2.2.3 Velocity Profile

The infalling galaxy is first taken to be on a radial trajectory, entering face-on in the medium. The galaxy starts at rest at $2R_{\rm vir}$, and it accelerates during infall into the halo. The infalling velocity profile is shown in Figure 2.2(left). The $x-$axis is the ratio of $R_c/R_{\rm vir}$ and the $y-$axis is $V(R_c)/V_{\rm vir}$, where $V_{\rm vir}$ is the circular velocity at the virial radius and is given by

$$V_{\rm vir} = \left(\frac{M}{10^8 h^{-1} M_\odot}\right)^{1/3} \left[\frac{\Omega_m^z 18\pi^2}{\Omega_m \Delta_c}\right]^{1/6} \left(\frac{1+z}{10h^{-1}}\right)^{1/2} km\ s^{-1} \tag{2.16}$$

Where all the terms have their usual meanings and are discussed earlier in the text. We also vary the initial velocity $V_{\rm in}$ (i.e. the velocity of the infalling galaxy at $2R_{\rm vir}$) from zero to $V_{\rm vir}$. We have taken the galaxy to go all the way up to the centre of the halo along a radial orbit. This has been done to study the worst-case scenario. In a realistic scenario, galaxies enter halos on different types of orbits, and a large fraction of galaxies do not approach the centre in the first crossing. The range of all the parameters about the infalling galaxy is given in part-II of Table 2.1.

We also study the scenario where the infalling galaxy has a finite angular momentum and hence does not go to the centre of the halo. This facilitates comparison with observations even though in all other aspects we continue to work with the worst-case scenario. The galaxy enters the cluster with a finite impact parameter b w.r.t. the centre of the central halo. The impact parameter is converted to an angle (θ) subtended at the centre, which is a parameter in our analysis. The radial infall is $\theta = 0$, which corresponds to $b = 0$. As we increase b, θ can be calculated

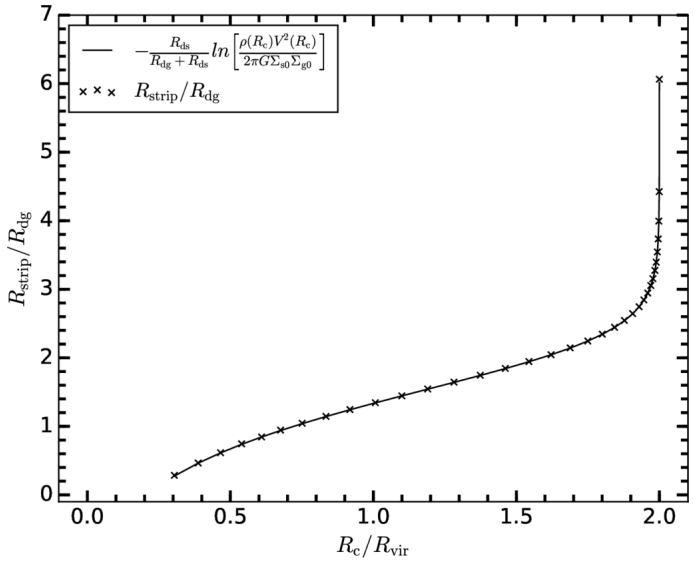

Figure 2.3: Stripping radius versus radius of the ambient medium for cluster environment at $z = 0$, for $M_{\rm gal} = 10^{12}$ $M_\odot$, $\lambda = 0.04$, $f_{\rm d} = 0.3$ and $\delta = 1.0$. The solid line is calculated using equation (2.18) and the dots are calculated using our model.

as $\sin(\theta) = b/2R_{\rm vir}$. The maximum value of θ is taken at $b = R_{\rm vir}$, and we get $\theta_{\rm max} = \pi/6$. An example of the trajectory, in the $x - y$ plane, which the infalling galaxy follow is shown in Figure 2.2(right).

2.3 Results

This section contains the results obtained by numerically solving the model proposed in the above section. We have worked with *ASTROPY* (Astropy Collaboration & Price-Whelan, 2018), which is a a package that allows working in dimensional units.

The quantity we are interested in, and we calculate, is the radius up to which the gas in the galactic disc is stripped, $R_{\rm strip}$ as the galaxy passes through the ambient medium. In all the results from here on we shall normalise the stripping radius with $R_{\rm dg}$ and R_c with the virial radius. Striping radius directly translates to the fraction of gas mass removed from the disc as:

$$M_{\rm removed} = \frac{1}{0.1M_{\rm d}} \int_{R_{\rm strip}}^{R_{\rm out}} 2\pi x \Sigma_{\rm dg}(x) {\rm d}x \tag{2.17}$$

To validate the numerical scheme used here we first reproduce the results of Gunn & Gott (1972). We also get an order of magnitude estimate of the stripping radius as a function of R_c, which can be done by solving the equation $a(R_c, R_{\rm strip}) = 0$ to get;

$$\frac{R_{\rm strip}}{R_{\rm dg}} = -\frac{R_{\rm ds}}{R_{\rm dg} + R_{\rm ds}} \ln\left[\frac{\rho(R_c)V^2(R_c)}{2\pi G\Sigma_{0g}\Sigma_{0s}}\right] \tag{2.18}$$

In Figure 2.3 we plot the stripping radius versus the radius of ambient medium calculated using equation (2.18) for cluster environment at $z = 0$, for $M_{\rm gal} = 10^{12}$ $M_\odot$, $\lambda = 0.04$, $f_d = 0.3$ and $\delta = 1.0$. Crosses on the plot show the values calculated from our model, for the same set of parameter values. The match is quite satisfactory, validating our numerical scheme.

We divide our results into three sections based on their respective environments and discuss the dependence of $R_{\rm strip}$ on various parameters separately. We further divide our results into two parts, the first one is for radially infalling galaxies, and the second one is for the galaxies falling with some impact parameter w.r.t. the central galaxies in clusters.

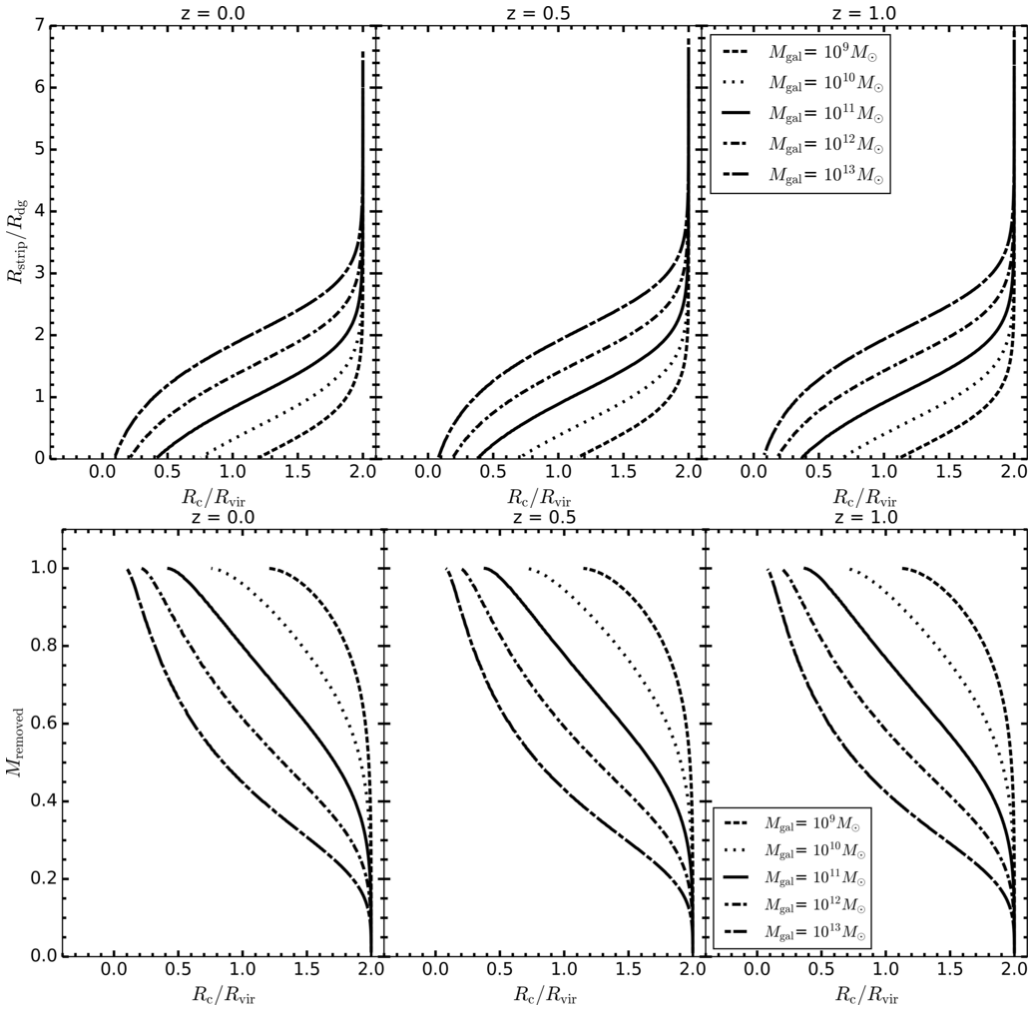

Figure 2.4: Top panel is the plot of cluster centric distance (R_c) versus stripping radius for the same parameters as that of Figure 2.3, for different values of z and $M_{\rm gal}$. Lower panel is the plot of $M_{\rm removed}$ calculated using equation (2.17).

2.3.1 Radial infall

Here we discuss the results for the case of radial infall of galaxies for all the background environments.

Cluster Environment

We start by studying the variation of stripping radius $R_{\rm strip}/R_{\rm dg}$ with mass of the infalling galaxy, $M_{\rm gal}$ in Figure 2.4. We show the results for different redshifts. The lower panel shows the mass stripped or removed due to ram pressure stripping as the infalling galaxy comes closer to the centre. Different line types refer to infalling

galaxies of different mass. We have used $\lambda = 0.04$, $f_d = 0.3$ and $\delta = 1.0$. We see that as the infalling galaxy goes closer to the centre of the cluster more and more gas gets stripped, eventually stripping the whole gas disc. The value of R_c at which the disc gets stripped is related to the mass of the infalling galaxy: lower mass galaxies lose the gas at larger R_c. It also follows that low mass galaxies get stripped in less time. We note that there is no variation with redshift, as can be seen by comparing the panels for $z = 0$, 0.5 and 1.0.

This result may appear counter-intuitive as both $\rho_\beta(R_c)$ and $V(R_c)$ both increase with z and hence the effect of ram pressure should be more prominent at higher redshift. However, a closer look at equation (2.18) shows that the z-variation in both numerator and denominator are same and get cancelled. This leaves $R_{\rm strip}/R_{\rm dg}$ independent of the redshift, which is what we observed in our numerical results. This cancellation requires that the infalling galaxy and the central halo form at the same redshift. If the infalling galaxy forms at a higher redshift then the disc has a higher surface density and can be expected to resist ram pressure stripping. We do not explore this variation as we are working with the worst-case scenario. We do not show the plots for $M_{\rm gal} < 10^9$ M$_\odot$ as the whole gas disc in those cases gets stripped at the periphery of the clusters. We shall discuss the implications of these observations in section 2.4.

Other parameters that we explore in the present study are the spin parameter λ, baryonic mass fraction of total mass residing in the infalling galaxy $f_{\rm d}$, and the initial velocity of the galaxy $V_{\rm in}$. In Figure 2.5 we give the plots for how does the stripping radius changes with variation in these parameters. The results are shown for $M_{\rm gal} = 10^{12}$ M$_\odot$. The top panel shows the results for different values of λ, for all z-values for galaxy starting at rest and $f_{\rm d} = 0.3$. The scaled radius of the infalling disc is directly proportional to λ as can be seen in equation (2.14). Hence, the larger the value of λ larger is the radial extension of the disc and smaller is the surface densities of both gas and stars implying that the restoring force on the gas disc will be lesser, making the ram pressure stripping more efficient. This distinction is clearly seen in the top panel of Figure 2.5. Note that we have assumed the same fraction for mass in gas and stars in the disc for all the value of the spin parameter. This may not be true, and this may affect the results. In particular, if the gas fraction is higher in galaxies with a higher spin parameter such that the product $\Sigma_{0g}\Sigma_{0s}$ takes on a higher value for the same disc mass, then the stripping will be less pronounced than in our model.

The middle panel is the variation with $f_{\rm d}$ at all the redshifts. For these plots, it is assumed that the galaxy starts with zero initial velocity at twice the virial radius and we use $\lambda = 0.04$. We observed that for higher values of $f_{\rm d}$ the gas disc can sustain itself against ram pressure for more time. The reason for this is that higher baryon density implies a higher surface density of the galactic disc, and hence higher is the restoring force, allowing the disc to stay intact for a longer time. The bottom panel gives the variation with $V_{\rm in}$ for $\lambda = 0.04$ and $f_{\rm d} = 0.3$. We see that as the galaxy enters the medium, the stripping is initially stronger for larger initial velocity but eventually the stripping radius becomes independent of the initial velocity and the radius at which the whole gas disc is stripped is the same for all the cases. Thus variation in surface density and spin parameter results in a stronger change in ram pressure stripping, whereas initial velocity does not affect the results significantly.

For all the three parameters that we explore in Figure 2.5, we have also shown

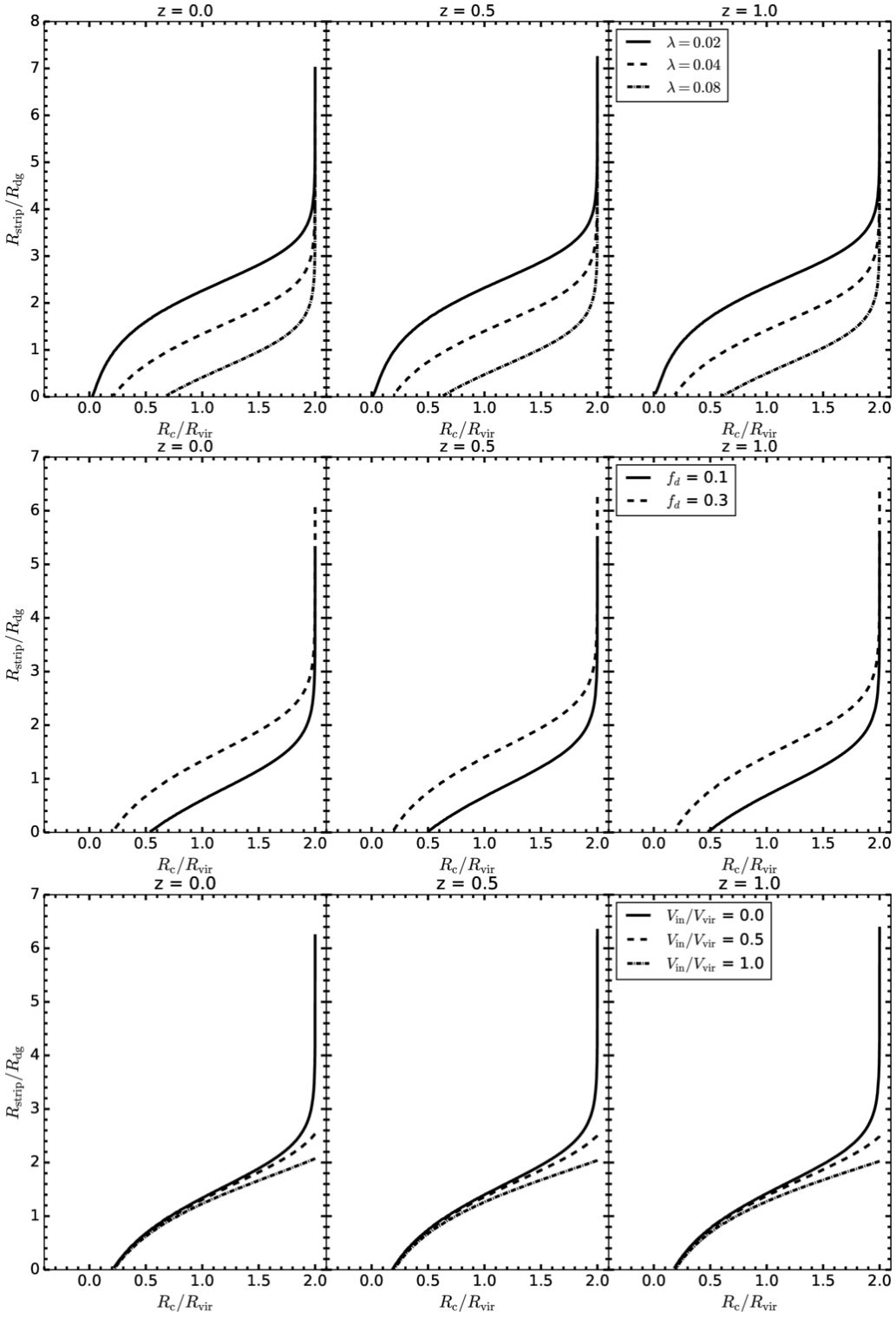

Figure 2.5: Variation of stripping radius with spin parameter, λ (top panel), baryonic mass fraction, $f_{\rm d}$ (middle panel) and infalling velocity lower panel. The infalling galaxy is taken to be 10^{12} $M_{\odot}$ in cluster environment.

the variation with redshift. Again, we do not see any variation with redshift, in agreement with arguments presented above.

Group Environment

We next describe ram pressure stripping in a group environment where the halo mass of the group is assumed to be $2 \times 10^{13.5}$ $M_\odot$. The density of the ambient medium decreases as we decrease the mass, suppressing the effect of ram pressure. The same is verified by our numerical results, which are plotted in Figure 2.6. For this plot we have taken the galaxy of mass 10^{12} $M_\odot$ to enter the medium at rest, at a redshift of zero, $\delta = 1.0$ and $\lambda = 0.04$. In this, we plot we show $R_{\rm strip}$ vs $R_{\rm c}$ for both clusters and groups at different redshifts. The thick, lower curves are for the cluster environment, and the upper set of curves are for the group environment. Striping in groups is slower as compared to clusters, and galaxies are able to reach closer to the centre without being stripped of gas. The z-variation is negligible, as discussed above.

Other parameters such as $M_{\rm gal}$, z, λ are also varied with ranges given in Table 2.1. The variation of stripping radius for all these follow the same trends, as was the case for the cluster environment. In Figure 2.9 we show the variation of stripping radius for different spin parameters and mass of the in-falling galaxy. The stripping radius is shifted to higher values for groups as compared to clusters, in consonance with the example shown in Figure 2.6.

Galaxy Environment

The third environment we study is the galaxy environment. In this case, the density of the ambient medium is lower than that for a group and cluster. This and the lower velocity of the infalling galaxy results in less efficient ram pressure stripping. The stripping radius for an infalling galaxy of mass $M_{\rm gal} = 10^{10}$ $M_\odot$ with zero initial velocity and other parameters same as that of the case of groups is plotted in Figure 2.7. Two different lines are for different values of δ, i.e. gas mass fraction in the ambient medium. Gas in the ambient medium is what is causing ram pressure stripping. Gas in the infalling galaxy strips faster for higher values of δ.

2.3.2 Non-radial infall

Galaxies fall into clusters on different types of orbits, with the generic orbit being non-radial. It implies that most galaxies do not come very close to the centre of cluster, and hence ram pressure stripping may be much less effective. To study the effect of non-radial motion, we vary the trajectory of infalling galaxies. The parameter that measures the deviation from radial infall is θ as introduced in section-2.2.3. The variation of $R_{\rm strip}$ with θ, $V_{\rm in}/V_{\rm virial}$, and z are plotted in Figure 2.8. Variation of stripping radius as different parameters are varied is shown here. The infalling galaxy is taken to have a mass of 10^{13} $M_\odot$ with $\lambda = 0.04$ for this figure.

In the first panel, we show the variation with θ, for $V_{\rm in}/V_{\rm virial} = 1$. As the angular momentum of the infalling galaxy about the centre of the cluster increases, stripping becomes less effective. We observed that for $\theta = 30^\circ$ the gas in the disc is retained up to the scale radius $R_{\rm dg}$. Thus non-radial infalling trajectory can lead to retention of some gas in a galaxy. Second and the third panels are the plots for $\theta = 15^\circ$. The

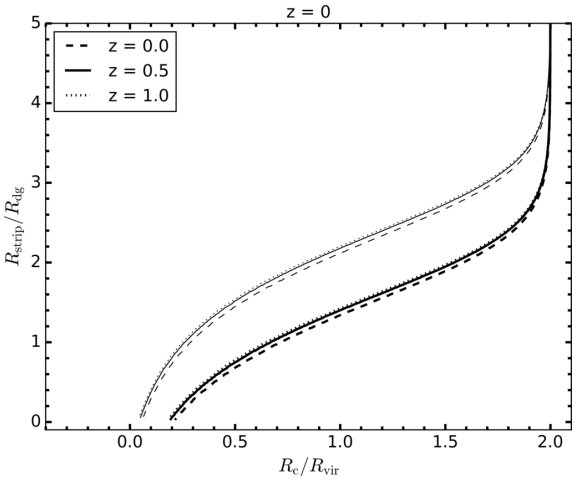

Figure 2.6: The comparison for stripping radius for cluster (thick, lower curves) and group (upper set of curves) environment for the infalling galaxy of same mass (10^{12} $M_\odot$) and different redshifts.

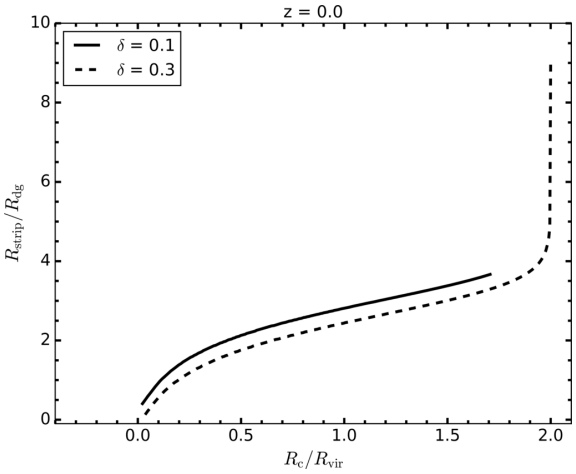

Figure 2.7: The variation of $R_{\rm strip}$ for the case of galaxy environment for an infalling galaxy of mass 10^{10} $M_\odot$.

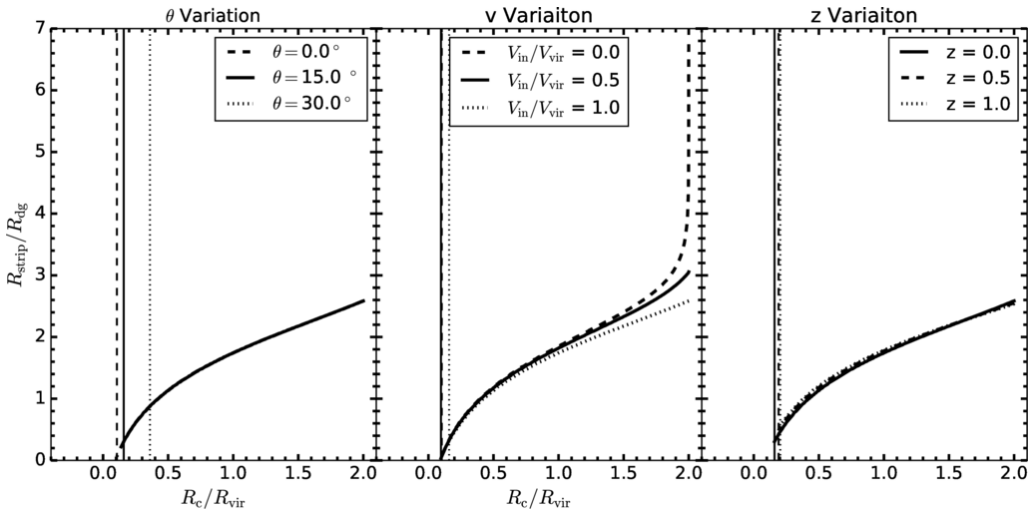

Figure 2.8: The plots of $R_{\rm strip}$ with θ, $V_{\rm in}/V_{\rm virial}$, and z for an infalling galaxy of mass 10^{13} $M_\odot$ with $\lambda = 0.04$. The vertical line show the last point in each curves. Second and the third panels are the plots for $\theta = 15°$.

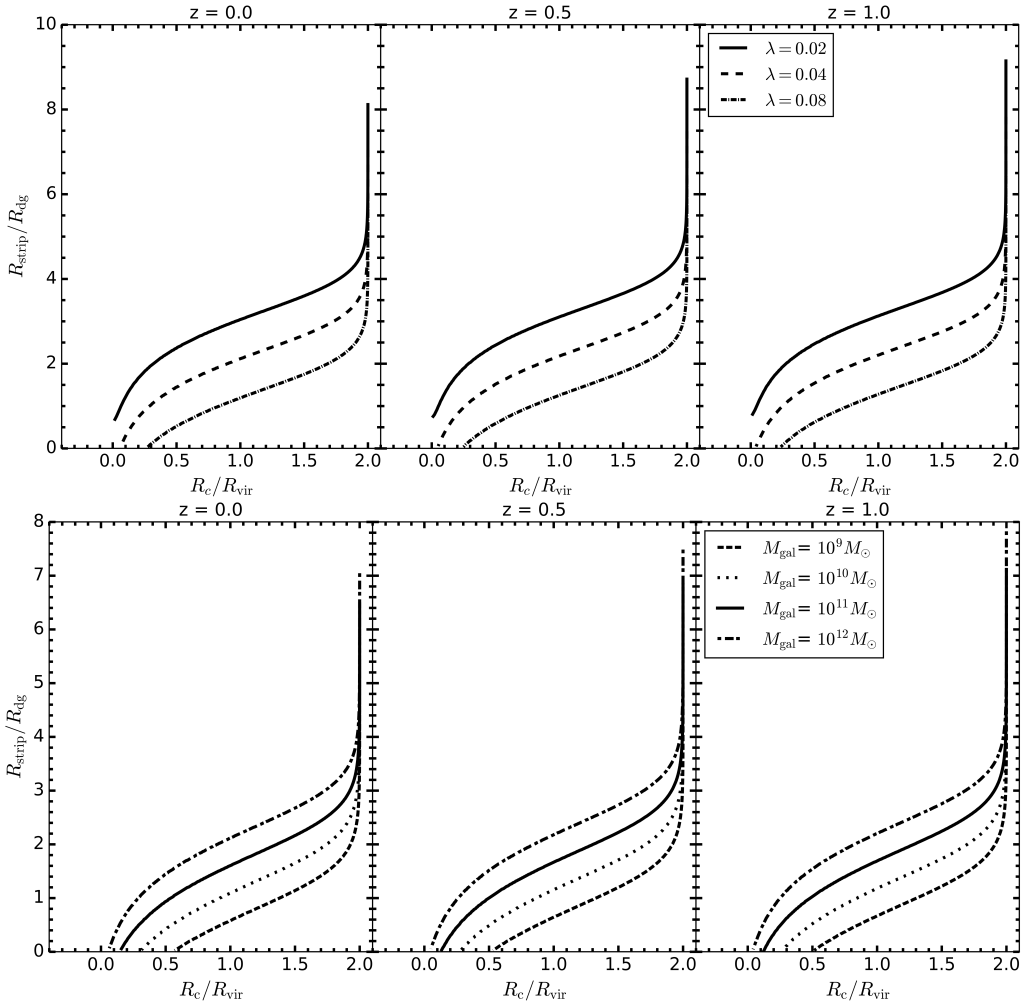

Figure 2.9: Variation of stripping radius with spin parameter, λ (top panel) and mass of galaxies (lower panel). The infalling galaxy is taken to be 10^{12} $M_\odot$in group environment.

variation with velocity and other parameters follows the same trends as discussed for radially falling galaxy.

2.3.3 Inhomogenous infalling disc

In order to test our analytical model and explore sources of large deviations from the worst-case scenario, we study stripping of an inhomogeneous disc galaxy. To simulate the infalling galaxy, we use Adaptive Mesh Refinement (AMR) code `RAMSES` (Teyssier (2002a). A box size of 300 kpc with a maximum resolution of $\sim$ 36 pc is taken. Simulated galaxy was setup in manner similar to that of G10 galaxy from Rosdahl et al. (2017a), with initial galaxy mass as M_{200} of 9×10^{11} $M_\odot$, with disc fraction of 12% and gas fraction of 5%. Stellar and gas disc both have an exponential profile with disc scale length of 3.2 kpc. We do not include any bulge in our simulation from the initial condition. We evolve the galaxy to get gas and stellar distribution at 450 Myr. Then a projection is taken to compute surface densities for gas and stars. The top left of Figure 2.10 shows the surface density.

The gas and stellar surface density from this simulation is then used to study the ram pressure stripping using our analytical model. We take a simple case of galaxy coming with V_{vir} subjected to the radially varying density of intra-cluster medium. Panels of Figure 2.10 are the snap-shots from our model as the galaxy passes through the ambient medium. The RPS is less effective in the regions where the disc had enhanced density and there is a sufficient amount of gas left in the disc of the galaxy, even as the galaxy passes through the central region of the cluster. Thus star formation can continue in galaxies falling into a cluster halo for at least one crossing time as gas in the denser molecular clouds is not stripped off. To illustrate this further in Figure 2.11 we plot the fraction of total mass removed versus $R_c/R_{\rm vir}$. A little more than 40% of the gas mass gets removed in case of inhomogeneous disc in contrast to 100% for the case of previously considered homogeneous disc. We thus conclude that though RPS is an effective mechanism of removing the gas from the disc galaxies, but the internal structure of the infalling galaxy has a larger role to play. Thus inhomogeneities in the interstellar medium of galaxies play a very significant role in the retention of gas and hence in star formation in spite of the effects of ram pressure.

2.4 Conclusions and Discussions

This work is a study to answer the question: *How effective is ram pressure stripping to remove gas from the galaxy as it passes through the ambient medium in a variety of halos and varying group of infalling galaxies?* We consider the ambient medium to be spherically symmetric and the disc galaxy enters the medium face-on. We consider both radial and non-radial initial velocities for the galaxies. We study three kinds of environments namely; cluster, group and galaxy. These differ from each other in their mass and retention of hot gas in the halo. The different depth of the potential well translates into different typical velocities with which galaxies fall in. We assume an isothermal profile for halos and a beta model for the gas distribution of ambient medium, the disc of the infalling galaxy is assumed to have an exponential surface density profile. The ambient medium and infalling galaxy profiles depend on various parameters: the redshift of formation, spin parameter, baryonic mass fraction etc. These have been discussed in detail in section 2.2. We model discs of galaxies as a set of annuli, and we test for ram pressure stripping for each annulus. This allows us to compute the stripping radius, i.e. the radius beyond which all gas from the disc has been stripped. Stripping radius is directly related to the fraction of gas mass removed from the galaxy. We compute the stripping radius in units of the gas disc scaling radius. This is pertinent for interpretation as much of star formation in disc galaxies happen around the scale radius, extending to a few scale radii at most. Thus, if stripping radius is of the order of gas disc scale radius or smaller then we expect star formation to be quenched. However, if the stripping radius is a few times the gas disc scale radius or larger, then star formation in such a galaxy may not be affected significantly.

The results of our study have been enumerated in section 2.3 in detail. Our approach throughout has been to consider the worst-case scenario, one where we maximum amount of gas is stripped from the galaxy. We outline the processes that may lead to gas being retained in the discussion below. Here we summarise our major findings.

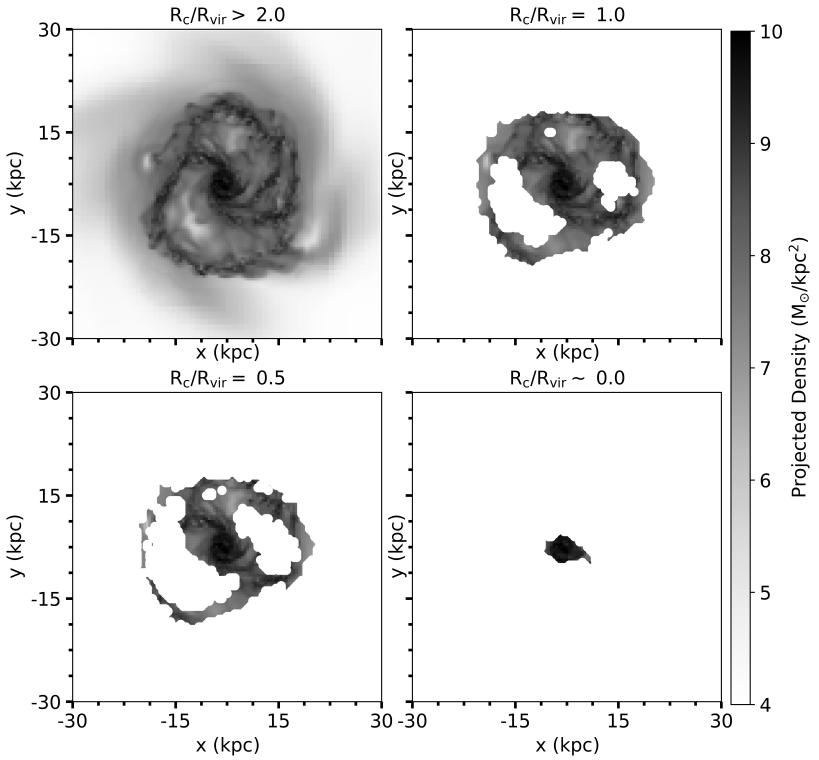

Figure 2.10: Infalling galaxy (as shown in the top left panel) with constant velocity of V_{vir} is subjected to radially varying intra-cluster density. We plot here gas projection at different cluster-centric distances, as given on the top of each panel.

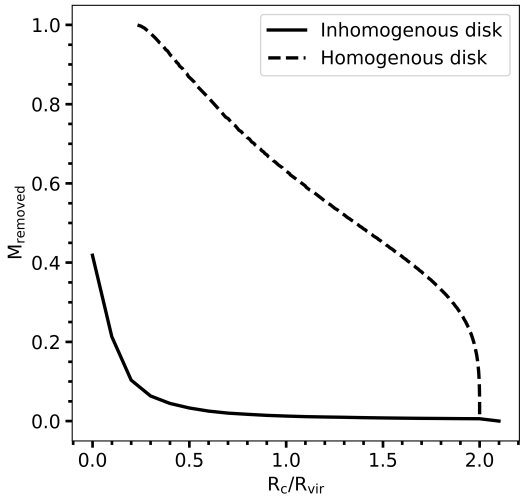

Figure 2.11: Fraction of mass removed as galaxy is subjected to ram pressure stripping plotted against cluster centric distance (R_c) scaled with virial radius of cluster ($R_{\rm vir}$), for both, inhomogeneous (solid line) and homogeneous discs (dotted line).

- For infall in a cluster of galaxies, galaxies of all masses lose the gas disc for radial infall well before reaching the centre of the cluster.

- For most massive galaxies, stripping radius falls below the gas disc scale length below 0.5 R_{vir} for the cluster. Thus we may expect to see some star-forming galaxies in the outer parts of a cluster, particularly if these are in their first passage through the cluster.

- In the case of non-radial infall, there is some gas left in the gas disc even after one crossing of the cluster: gas retention is stronger when the angular momentum of the infalling galaxy is larger for a given initial speed.

- Ram pressure stripping is independent of redshift if we assume the worst-case scenario of the halo and galaxy forming at the same time. If the galaxy forms earlier, as is likely in most situations, more gas will be retained. For example, equation 2.18 will be modified if the infalling galaxy collapsed at redshift z_g and the halo into which it falls collapsed at z_c with $z_g \geq z_c$:

$$\frac{R_{\rm strip}}{R_{\rm dg}} = \frac{R_{\rm ds}}{R_{\rm dg} + R_{\rm ds}} \left\{ \ln \left[\frac{2\pi G \Sigma_{0g} \Sigma_{0s}}{\rho(R_c) V^2(R_c)} \right] + 4 \ln \left[\frac{1+z_g}{1+z_c} \right] \right\} \tag{2.19}$$

  where the values of surface densities, density, velocity, etc. on the right hand side of the equation are scaled to the present epoch. Thus, we see that $R_{\rm strip}$ can be large if the infalling galaxy collapses at a higher redshift.

- We find that gas is stripped more easily for the larger spin parameter. In our model, the disc scale lengths are directly related to the spin parameter of their host halos: a larger spin parameter implies a larger disc scale length. This, in turn, implies that the available gas mass is distributed over a larger area. We have assumed that the ratio of gas mass (and stellar mass) is independent of the spin parameter. If the gas mass is in some manner correlated with the spin parameter of galaxy halos, then the variation seen in our model may not be correct.

- The variation of the initial velocity of the infalling galaxy does not matter much over the full orbit, though it does make a difference at early stages. This is due to the acceleration during infall dominating over any initial motion.

- Ram pressure stripping is sub-dominant in the group environment as compared to clusters. This is due to lower retention of hot gas in the intra-group medium and lower infall velocities due to shallower potential wells.

- This trend continues to lower scales as ram pressure stripping is less important in galaxy environments.

There are several processes that may reduce the impact of ram pressure stripping. We have already discussed non-radial motions above. One such process, which is expected to decrease the effect of ram pressure stripping is the formation of gas clouds or star-forming regions in the galaxies. Such regions of a significantly higher surface density of gas can resist ram pressure much better than the idealised smooth exponential disc considered here. This requires us to consider a non-axisymmetric

distribution of gas and stars. As an illustration of this, we have considered an inhomogeneous simulated Adaptive Mesh Refinement (AMR) code `RAMSES` and then subjecting it to ram pressure stripping algorithm. More than 50% of gas is retained in the disc due inhomogeneities in the disc as shown in Figures 2.10 and 2.11. Thus star formation can continue in an infalling galaxy for about one crossing time, if not longer. At later times, feedback due to star formation in remaining dense clouds will disperse the gas and star formation rate will rapidly approach zero. We plan to explore this extended model in detail in the future.

Ram pressure is expected to dominate in the regions where there is no galaxy in the vicinity of the infalling galaxy. Whenever there is another galaxy within the radius of influence of the infalling galaxy, tidal stripping or galaxy harassment can also play an important role. Tidal stripping can remove all matter from the outer parts of the infalling galaxy. Considering time scales, we believe ram pressure stripping to be very important in cluster halos while tidal stripping is likely to dominate in galaxy halos. In view of other processes, it is important to note here that our analysis is valid only for the first few orbits of the infalling galaxy.

The processes that contribute to significant deviations from the worst case are:

- Non-radial orbits.
- Early formation of infalling galaxies.
- Inhomogeneous ISM in infalling galaxies.

As we have shown, each of these can contribute significantly, and hence in a realistic case, the stripping radius can be an order of magnitude higher than the estimates for the worst-case.

In case of ram pressure stripping in galaxy halos, there is one scenario that can make the process very effective: if the orbit of the infalling galaxy is such that it crosses the disc then for a brief period, it encounters a high-density ambient medium. This can be effective even if this crossing is in the outer parts of the gas disc.

We have studied the process of ram pressure stripping, and we find that it is a very efficient process for removing gas from discs of infalling galaxies in clusters of galaxies. We expect most galaxies to lose all their disc gas within a couple of orbits around the centre of a cluster. The process is less efficient in groups and clusters, and we expect to see gas-rich galaxies in group and galaxy environments.

Chapter 3

Effect of large-scale filament environment in Coma supercluster

This chapter is based on Mahajan, S., Singh, A. and Shobhana, D. "Ultraviolet and optical view of galaxies in the Coma supercluster", 2018, *MNRAS, 478, 4336*

3.1 Introduction

The Coma supercluster is one of the richest large-scale structures (Chincarini & Rood, 1976) in the nearby Universe, comprising two clusters of galaxies, connected by a web of large-scale filaments around 30 h_{70}^{-1} Mpc long (e.g. Fontanelli, 1984). The two clusters, Coma (Abell 1656) and Abell 1367, along with the filaments of galaxies, dispersed with several small galaxy groups span $\sim$ 500 square degrees on the sky (Mahajan et al., 2010). The large-scale filaments in the Coma supercluster have not just been observed by means of the galaxy distribution in the optical wavebands (Gregory & Thompson, 1978; Mahajan et al., 2010), but also diffuse emission in the radio continuum (Kim et al., 1989).

Based on a study using optical data from the Sloan Digital Sky Survey (SDSS) data release (DR7), Mahajan et al. (2010) found that the star formation-density relation in the Coma supercluster for the giant galaxies is much weaker than their dwarf counterparts. However, the fraction of star-forming galaxies for both declines to $\sim$ 0 at the centre of the clusters (also see Mahajan et al., 2011). Cybulski et al. (2014) furthered the study of star formation in the Coma supercluster by combining a complementary optical dataset from SDSS DR 9, with IR data from the *Wide-Field Infrared Survey Explorer* (Wright et al., 2010) and UV data from the *Galaxy Evolution Explorer* (Martin et al., 2005). Cybulski et al. (2014) corroborated the results of Mahajan et al. (2010, 2011) by probing both obscured and unobscured star formation down to ~ 0.02 $M_\odot$ yr^{-1}, in order to quantify the effect of different types of large-scale environments: groups, clusters, filaments and field, on quenching star formation (SF) in galaxies.

In the absence of dust in star-forming galaxies, the UV emission is a good tracer of massive (> 10 $M_\odot$) star formation. On the other hand, optical emission lines such as Hα probe instantaneous star formation over a timescale of $\lesssim$ 20 Myr (Kennicutt, 1998a). Assuming that the UV luminosity is not overwhelmed by the contribution

from the old stellar populations due to the UV upturn such as in massive early-type galaxies (O'Connell, 1999), the UV luminosity measures star formation over a timescale of $\sim$ 100 Myr (Kennicutt, 1998a). Hence, the star formation rate (SFR) estimated from optical emission lines delineates the continuous SF in a galaxy, while the SFR determined from the UV is representative of its recent SF activity. But even though *GALEX* and its predecessor UV imagers have been used to investigate individual galaxies within clusters and groups (e.g. Hicks & Mushotzky, 2005), or galaxy populations therein (e.g. Donas et al., 1990, 1995; Cornett et al., 1998; Boselli et al., 2005), limited work has been done to analyse the UV properties of galaxies in the large-scale filaments.

Since the Coma supercluster is one of the most well-studied regions in the nearby Universe, many other authors (e.g. Bernstein et al., 1995; Mobasher et al., 2003; Hammer et al., 2012; Smith et al., 2010, 2012) have made use of optical and UV data to study the Coma and Abell 1367 clusters and their surroundings. With the advent of large redshift surveys several studies (Gavazzi et al., 2010; Mahajan et al., 2010, 2011; Cybulski et al., 2014; Gavazzi et al., 2013) have also used multi-wavelength data at optical, UV and 21 cm continuum to study the properties of galaxies in the entire supercluster region. In this work we make use of similar datasets: UV data derived from *GALEX* and optical spectroscopic and photometric data from the SDSS for the entire Coma supercluster to further explore the impact of the environment on the properties of galaxies.

Conventionally, the 'environment' of galaxies is quantified as the projected density of galaxies in a fixed 2-d or 3-d region of the sky (e.g. Dressler, 1980). Muldrew et al. (2012) combined 20 published methods of defining the environment into two (i) methods which use nearest-neighbours to probe the underlying galaxy density and, (ii) fixed aperture methods. Muldrew et al. (2012) found that while the former are better suited for quantifying internal density within massive halos, the latter, fixed-aperture methods are better for probing the large-scale environment. Therefore, in order to characterise the large-scale filaments, a combination of these methodologies is required to quantify the environment on different scales. In this work, we implement their result by making use of two different algorithms to define the large-scale filaments, and high-density nodes of the cosmic-web characterised as clusters and groups. We also present a catalogue of all spectroscopically-confirmed galaxy members of the Coma supercluster detected in the UV.

This chapter is organised as follows: in the next section, we describe our datasets, followed by definition of environment in section 3.3. In section 3.4 we analyse the broadband colours of galaxies as a function of environment, while in section 3.5 we study the impact of the large-scale filaments on the properties of galaxies. Finally, we discuss our results in the context of the existing literature in section 3.6 and summarise our results in section 3.7. Throughout this chapter we use concordance ΛCDM cosmological model with $H_0 = 70\,\mathrm{km\ s^{-1}\ Mpc^{-1}}$, $\Omega_\Lambda = 0.7$ and $\Omega_m = 0.3$ to calculate distances and magnitudes. We note that given the low redshift of the Coma cluster ($z = 0.023$), our results are independent of the cosmological model used.

3.2 Data

This work is based on the optical photometric and spectroscopic data acquired from the SDSS data release 12 (Alam et. al. , 2015), and UV data from the *GALEX* survey (Bianchi et al., 2014). In the following, we describe both the datasets used in this work.

3.2.1 Optical data

The Sloan Digital Sky Survey (SDSS) uses two fibre-fed double spectrographs, covering a wavelength range of 3800–9000 Å. The resolution $\lambda/\Delta\lambda$ varies between 1500 and 2500 in different bands. Galaxy magnitudes[1] are K-corrected to $z = 0$ (Chilingarian & Zolotukhin, 2012), and for galactic extinction. For the latter, the $E(B-V)$ values in each of the g and r bands are calculated using the Schlegel et al. (1998) dust maps.

Following Mahajan et al. (2010), we select all galaxies brighter than $m_r = 17.77$ mag and spectroscopic data which lie within $170° \leq \mathrm{RA} \leq 200°, 17° \leq \mathrm{Dec} \leq 33°$ and $0.013 \leq z \leq 0.033$. These criteria yield a total of 4,280 galaxies. In this work we use the equivalent width of the Hα emission line as a measure of the instantaneous (< 10 Myr) star formation rate (SFR) of galaxies.

The spectra of 86% of all the galaxies in the Coma supercluster have all four emission lines (Hα, [NII], Hβ and [OIII]) required to confirm the presence of nuclear activity based on the emission-line ratio diagnostics as first proposed by Baldwin et al. (1981). For this work, we use the classification criteria of Kewley et al. (2001) to identify 518 ($\sim 12\%$) galaxies as AGN. Where applicable, we perform the analysis using non-AGN galaxies only, i.e. the entire sample minus the 518 galaxies whose spectra are dominated by AGN emission.

3.2.2 Ultraviolet data

The ultraviolet photometric data for this work is taken from the *Galaxy Evolution EXplorer* final data release (*GALEX*; Bianchi et al., 2014). *GALEX* conducted an all-sky imaging survey along with targeted programs in two photometric bands: 1516 Å ("far ultraviolet" or FUV) and 2267 Å ("near ultraviolet" or NUV). The bulk of our sample consists of bright, nearby galaxies, and therefore, no exposure time or brightness limit constraints were imposed while looking for a *GALEX* detection. For best photometric and astrometric quality, we have restricted our sample to the inner 0.5° of the *GALEX* field of view and having NUV_artifact < 1. As suggested by Wyder et al. (2007), the latter excludes objects whose flux may be contaminated by reflection from bright stars.

65% of the UV imaging data used in this work were taken as part of the *GALEX*'s primary All-Sky Imaging Survey (AIS) with an effective exposure time of $\sim$0.1 ks. Most of the rest of the data comes from individual guest investigator programs (28%) or the Nearby Galaxies Survey (NGS; 6%) with an effective exposure time of $\sim$1.5 ks. The remaining data was taken as part of *GALEX*'s medium or deep

[1]Throughout this chapter, we use the SDSS 'model' magnitudes. The model magnitude for each galaxy is calculated using the best-fit parameters in the r band, and applied to all other bands; the light is therefore, measured consistently through the same aperture in all bands, allowing for an unbiased measure of galaxy's colours.

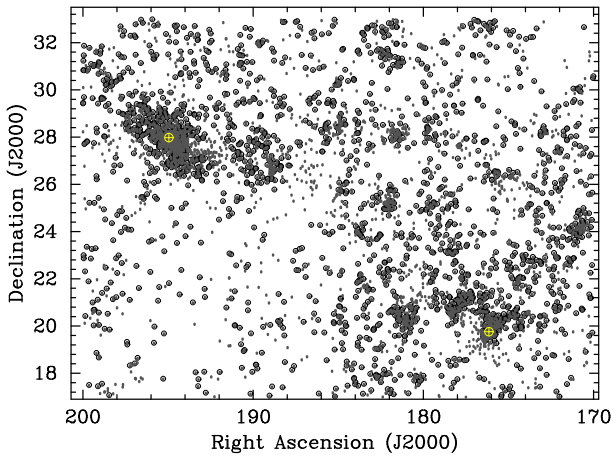

Figure 3.1: The Coma supercluster. All spectroscopically confirmed galaxies are represented as *dots*, and all galaxies with a UV counterparts are *encircled*. The *yellow encircled crosses* represent the centre of the Coma and Abell 1367 clusters.

Plate	MJD	Fiber	*GALEX* ObjID	RA (J2000)	Dec (J2000)	z	Local env	M_r mag	m_{NUV} mag	m_{FUV} mag
2241	54169	562	-	195.547	28.172	0.0299	2	-18.69	-	-
2241	54169	517	3191682282023817108	194.984	27.746	0.0298	2	-19.43	19.05	19.69
2240	53823	530	-	194.629	28.234	0.0243	2	-19.18	-	-
2240	53823	617	3187917554210322283	195.170	27.997	0.0236	2	-20.67	20.61	22.07
2509	54180	226	-	176.020	19.533	0.0243	2	-18.63	-	-
2506	54179	548	2555795125061031411	176.134	20.107	0.0240	2	-20.05	19.87	20.67
2242	54153	384	3054146571327246615	195.313	27.669	0.0236	2	-18.64	22.01	23.13
2241	54169	573	-	195.406	28.016	0.0238	2	-18.07	-	-
2241	54169	371	-	194.523	28.243	0.0240	2	-21.39	-	-
2240	53823	518	-	194.548	27.940	0.0284	2	-19.45	-	-

Table 3.1: The SDSS and *GALEX* data for all the Coma supercluster galaxies in our sample. The local environment of galaxies listed in column 8 is: 0: field, 1: filaments and 2: cluster/group, respectively. See section 3.3 for detailed definition of these environments.

imaging surveys (MIS and DIS), having an average exposure time of ∼1.5 and 30 ks respectively.

We searched for the UV counterpart of each spectroscopically-confirmed supercluster galaxy within a circular aperture with radius 4″ centred on the optical source (Budavári et al., 2009). Amongst others, this process also yields 477 optical sources multiply matched to many UV sources. Following Bianchi et al. (2011), we considered the multiply-matched UV sources as duplicates if they were within 2.5″ of each other. Of those UV sources which satisfied this criterion, if the *photoextractid* of both the UV sources is the same implying both of them are from the same observation, they were both considered unique, else they were assumed to be multiple observations of the same source. In the former case, the matched counterpart was represented by the UV source with the highest *NUV* exposure time. In case of equal *NUV* exposure times for both, the one closest to the field centre in the *GALEX* image was chosen.

For the *FUV* and *NUV* photometry we used Kron magnitudes generated by the *GALEX* pipeline and corrected for galactic extinction using Schlegel et al. (1998) dust maps, assuming the reddening law of Cardelli et al. (1989). The reddening factor for *GALEX* bands is $AFUV/E(B-V) = 8.24$ mag and $ANUV/E(B-V) = 8.2$ mag (Wyder et al., 2007), respectively, which lead to a median extinction correction of ~ 0.23 mag in both the UV bands. Since *GALEX* colour is an important part of our analysis, we chose the *NUV* band as the primary band and then obtained the corresponding *FUV* magnitude measured within the same Kron aperture as estimated using the *NUV* image to get an accurate UV colour.

Hammer et al. (2010) have created a source catalogue of objects detected in a 26 ks deep *GALEX* field in the Coma cluster. For 94 galaxies (matched within 10″) of their sources, we find a median offset of 0.1 mag in the *FUV* and 0.2 mag in the *NUV* magnitudes, respectively. The discrepancy in the measured magnitudes is due to the bayesian deblending technique used by these authors, since the photometry thus obtained is relatively more sensitive to the apparent sizes of galaxies, and underestimates the flux for extended ($R_{90,r} > 10''$) galaxies (Hammer et al., 2010), which make up $> 50\%$ of our sample.

Our final UV catalogue comprises 2,447 UV sources uniquely matched to spectroscopically confirmed SDSS galaxies in the Coma supercluster region. The combined optical-UV data are shown in Figure 3.1, and the data for all 4,280 galaxies are given in Table 3.1. The columns in Table 3.1 are: (i) Plate, (ii) MJD, (iii) Fibre ID, (iv) *GALEX* ID, (v) Right ascension (J2000), (vi) Declination (J2000), (vii) redshift (viii) local environment (0: field, 1: filaments and 2: cluster/group), (ix) $r-$band magnitude (x) *FUV* magnitude, (xi) error in *FUV* magnitude, (xii) *NUV* magnitude and (xiii) error in *NUV* magnitude. The first three columns can be used to crossmatch galaxy data with the SDSS database, while the unique *GALEX* ID can be used for the same with the *GALEX* database.

Since we are covering such a large chunk of the sky ($\sim$ 500 sq. degrees), it is unsurprising that the depth of *GALEX* observations varies widely over the entire supercluster. Cybulski et al. (2014, see their section 2.2 for details), have shown that the *GALEX* data for the Coma supercluster is 75% complete to a luminosity of $\sim$ 26.42 ergs. We, therefore, stress that our UV catalogue is incomplete for two major reasons: firstly, due to incomplete spatial coverage of *GALEX* due to the presence of bright foreground sources (e.g. region around $\alpha \sim 186°$ and $\delta \sim 26°$ in

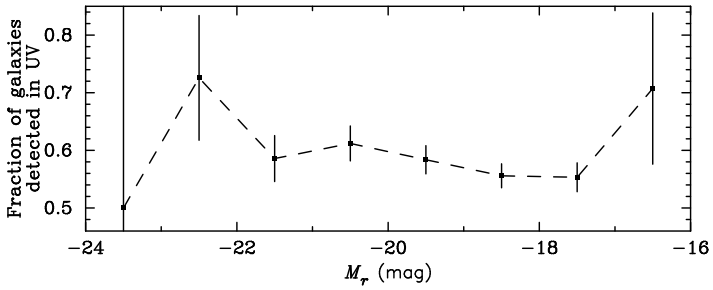

Figure 3.2: Fraction of Coma supercluster galaxies with a UV counterparts in bins of absolute r-band magnitude. On average, $\sim$ 60% of the galaxies are detected by *GALEX* in each bin of M_r. The error bars on each point represent Poissonian uncertainty.

Figure 3.1). Secondly, as shown in Figure 3.2, only $\sim$ 60% of the spectroscopically-confirmed galaxies are detected in each bin of $r-$band magnitude. However, since the fraction of galaxies missing a UV counterpart is almost uniform across the entire luminosity range, except the lowest and the highest luminosity bin comprising 2 and 41 galaxies respectively, we have not corrected for this incompleteness in the following analysis. We use all the UV-detected galaxies for all UV-based analysis, and all spectroscopically-confirmed galaxies for all the optical analysis below.

3.3 The environment

It is now well established that the Coma supercluster comprises of a filamentary network including the two major clusters Coma and Abell 1367, and other smaller galaxy groups (Gregory & Thompson, 1978; Mahajan et al., 2010). This filamentary network has been mapped by the distribution of galaxies as well as observed in the radio continuum at 326 MHz (Kim et al., 1989). In the following sections, we will analyse optical and ultraviolet properties of galaxies in the Coma supercluster as a function of their environment. In order to do so, we first modelled the complex cosmic-web of the Coma supercluster by identifying its various components as described below.

3.3.1 The cosmic-web with DisPerSe

The filaments in the Coma supercluster in this work are defined using Discrete Persistent Structures Extractor (DisPerSe; Sousbie et al., 2011), which is an algorithm capable of finding structures, in particular, linear structures such as large-scale filaments within discrete 2d or 3d datasets (see Sousbieb, 2011, for illustrations of DisPerSe in the astrophysical context). DisPerSe allows us to work directly with particles, and requires only one tunable parameter corresponding to the significance of the retained features in units of σ[2]. Furthermore, DisPerSe does not make any presumptions about the quality of sampling, homogeneity or topology of the space.

DisPerSe is based on discrete Morse theory and persistence homology theory. The Delaunay tessellation is used to segregate the whole space into triangular

[2]In this work we use a significance threshold of 3σ which corresponds to a probability of $\sim$ 0.997 (Sousbie et al., 2011) .

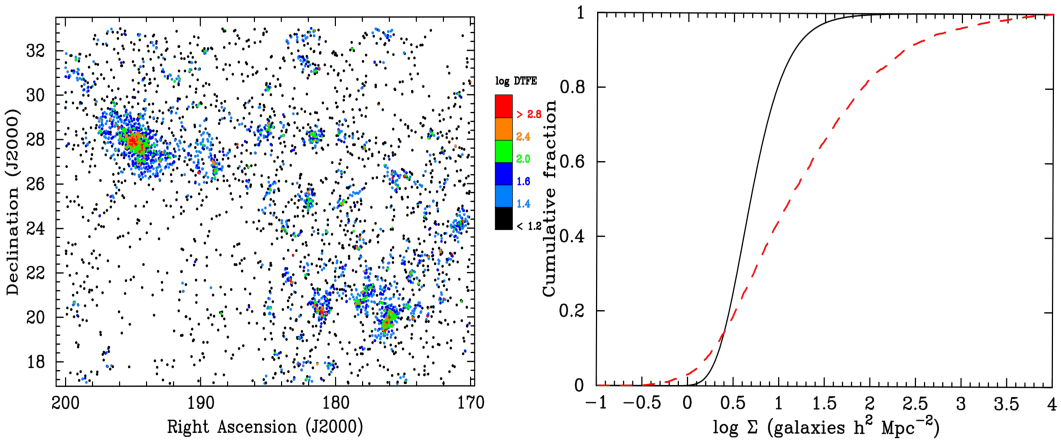

Figure 3.3: *(left:)* The Coma supercluster galaxies colour-coded with log of Delaunay Tessellation Field Estimator value (see text). *(right:)* The mean cumulative distribution of the DTFE density for the random samples *(black solid line)* compared with the same for the Coma supercluster *(red dashed line)*. The Coma supercluster region is not just denser relative to the random distributions, but also comprise very over-dense (clusters and groups) and under-dense (field) regions.

regions. The Delaunay Tessellation Field Estimator (DTFE; Schaap & van de Weygaert, 2000; Cautun & van de Weygaert, 2011) allows the estimation of density at each vertex of the triangular complexes created by Delaunay tessellation. The estimated density can then be used in the Morse theory to identify the critical points where the gradient of density field vanishes.

The topology of a function can be studied using the topology of points which are above a continuous monotonically changing threshold. If the persistence value of a pair of critical points is higher than the noise level defined by the root mean square of persistence values of randomly selected points, the detected feature tends to have a significant density contrast. One can select a threshold of persistence values above which the pairs are to be considered for analysis. This enables the extraction of all significant features in the space while eliminating noise. The filaments can be identified as lines connecting two maximas residing at the centres of groups and cluster regions. For a detailed discussion of the theoretical framework which forms the basis for DisPerSe, we refer the reader to Sousbie et al. (2011).

In Figure 3.3 (left), we show the position of all galaxies colour-coded by their DTFE value. Following Cybulski et al. (2014), we generated 1500 random samples of galaxy densities with the same number of galaxies as in the Coma supercluster, but their positions distributed randomly. Figure 3.3 (right) shows a comparison between the cumulative distribution of the mean of the galaxy density of 1500 random samples with the Coma supercluster. This figure is directly comparable to figure 4 (right) of Cybulski et al. (2014). Since we have used a dataset very similar to theirs, we also observe trends similar to those seen by Cybulski et al. (2014). The densities in the Coma supercluster gradually increases from a few to $\sim 100 - 1000$ galaxies per square Mpc.

Figure 3.3 shows that the Coma supercluster on average is denser than a randomly selected region of the Universe, in the sense that the median density of galaxies in the supercluster is ~ 0.4 dex higher relative to the mean of random samples. These observations are well in agreement with other studies (Gavazzi et al., 2010),

reporting that with a mean density of 0.019 gal $(h^{-1}\ Mpc)^{-3}$ the Coma supercluster is three times over-dense relative to the Universe in general (0.006 gal $h^{-3}\ Mpc^{-3}$ for $M_i < -19.5$ mag; Hogg et al., 2004).

3.3.2 Identifying Galaxy Groups

Along with the clusters and the filament, another prominent environment in the Coma supercluster is of galaxy groups. In this work, we identify the galaxy groups by Hierarchical Density-Based Spatial Clustering of Applications with Noise (HDBSCAN[3]; McInnes et al., 2017). HDBSCAN is a theoretically and practically improved version of the popular Density-based spatial clustering of applications with noise (DBSCAN) algorithm (Ester et al., 1996; Schubert et al., 2017).

DBSCAN requires minimal domain knowledge to determine input parameters, and works efficiently on large datasets. For our work, DBSCAN is a better choice relative to other unsupervised clustering algorithms (e.g. k-means) because of its ability to detect arbitrarily shaped clusters. The functioning of the algorithm is primarily governed by two parameters, minPts (minimum number of data points to be considered as a 'cluster') and ϵ (the maximum radius permissible for a cluster). To begin with, DBSCAN classifies the data into three categories: core points (points with the maximum number of minPts in their vicinity), border points (points with lesser number of minPts but in the vicinity of a core point), and outliers (all other data points). The main issue with this approach is that the points which are in the vicinity of more than one core points, will have an equal probability of being assigned to either of the clusters. Another drawback of the DBSCAN algorithm is that it is inefficient in finding clusters in an inhomogeneous dataset, making it very difficult to select the initial parameters for the algorithm.

HDBSCAN improves upon the methodology of the DBSCAN algorithm by extracting flat clustering based on stability of clusters (J. G. B. Campello et al., 2013). The main governing clustering parameter in HDBSCAN is min_cluster_size (the minimum size of an allowed cluster), which is chosen by the user based on the knowledge of the dataset. Another parameter which is crucial in deciding the final clustering is min_samples, which sets how conservative the clustering should be. By default min_samples is set equal to min_cluster_size, but can be tuned to suit the dataset. A very large value of min_samples will label most of the data points as noise, whereas setting it as unity will allow all the data points to be clustered. In this work we adopt min_sample_size = 20 and min_samples = 10. The working of HDBSCAN can intuitively be divided into five steps:

- calculation of the *mutual reachability distance* (Campello et al., 2015) for all the data points, where, the mutual reachability distance between two points a and b is defined as the maximum of the distance to the kth nearest neighbour for a, b or the distance between a and b, i.e. $d_{\text{mutual}}(a, b) = max\{\text{core}_k(a), \text{core}_k(b), d(a, b)\}$,
- construction of the minimum spanning tree of the data points weighted by their mutual reachability distance,
- building the hierarchy of the connected components,

[3]Specifically we adopted the Python implementation of HDBSCAN

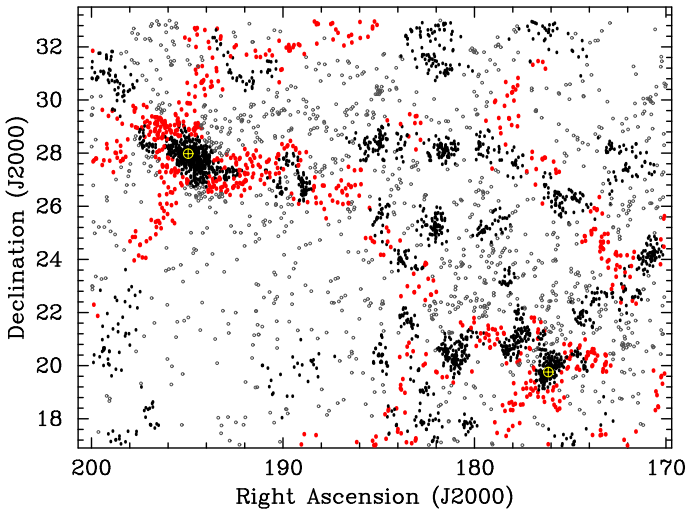

Figure 3.4: Different environments in the Coma supercluster. The *grey open circles, red points*, and *black points* represent the field, filament and cluster galaxies, respectively. The *yellow encircled crosses* represent the centre of the Coma and Abell 1367 clusters.

- depending on the minimum size of the cluster allowed (min_cluster_size), HDBSCAN condenses and retains the clusters having a size greater than min_cluster_size. This step significantly reduces the number of branches relative to the previous step; and

- the clusters which persist longer than their descendant clusters in the hierarchy tree are chosen as stable clusters, and their descendants are disregarded, else the descendant clusters are chosen as stable clusters.

The final step allows HDBSCAN to select clusters with varying density.

3.3.3 Characterisation of environment

For further analysis of galaxy properties as a function of their environment, we segregate the Coma supercluster into three 'local' environments:

- Cluster/group galaxies (2,401): all galaxies identified by HDBSCAN to lie in groups or clusters. For simplicity, hereafter we refer to all the galaxies in these environments as cluster galaxies.

- Filament galaxies (766): all galaxies which are within a radius of 1 Mpc of the filamentary spine (see section 3.5 for details on the choice of filament radius) detected by DisPerSe.

- Field galaxies (1,113): all other galaxies which lie within $170° \leq \mathrm{RA} \leq 200°, 17° \leq \mathrm{Dec} \leq 33°$, and have redshift $0.013 \leq z \leq 0.033$, but are not selected in either of the above two categories.

Figure 3.4 shows the projected distribution of galaxies belonging to various environments in the Coma supercluster.

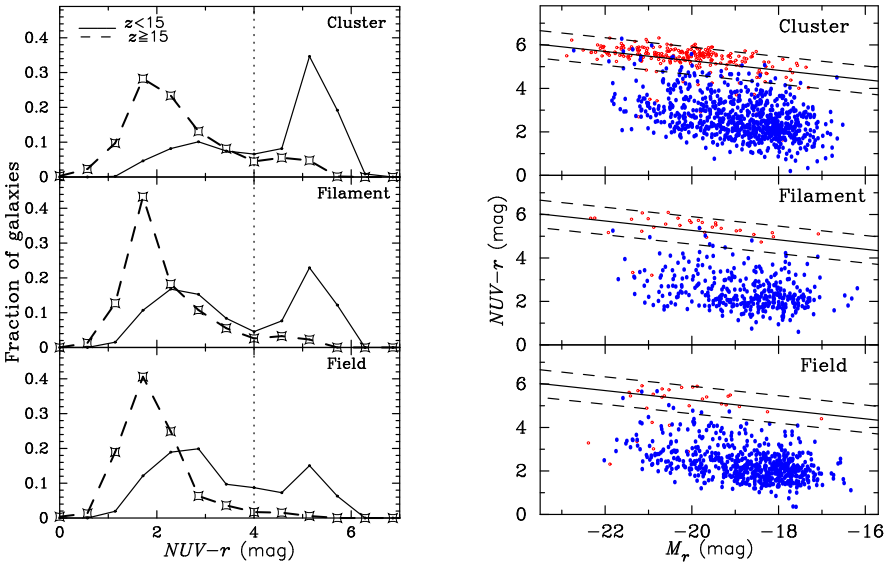

Figure 3.5: (*left*) $NUV - r$ colour distribution of dwarf ($z \geq 15$) and giant ($z < 15$) galaxies in three different environments in the Coma supercluster. (*right*) The $NUV - r$ versus M_r colour-magnitude diagram for the galaxies in three different environments in the Coma supercluster. The points are colour-coded as: passive galaxies (EW(Hα) ≤ 2 Å) as *open red symbols*, and star-forming galaxies (EW(Hα) > 2 Å) as *blue points*. The red sequence fitted to the passive galaxies in clusters are repeated in the other two panels.

3.4 Broadband colours of galaxies in different environments

In this section, we test the impact of the local environment (section 3.3) on optical and UV colours of galaxies. It is worth noting that although such studies have been conducted for various samples of groups and clusters at different redshifts, no other large-scale structure offers such a *continuous range of 'local' environments* in the nearby Universe (e.g. Gavazzi et al., 2010; Mahajan et al., 2010; Cybulski et al., 2014). The proximity of the Coma supercluster also makes it a special laboratory to investigate the properties of not just the giant, but also the dwarf galaxies. But since M^* is well correlated with environment (e.g. Haines et al., 2007), and maybe the underlying property governing other galaxy observables (Kauffmann et al., 2003), where applicable we perform the following analysis in three classes of environments and two bins of luminosity. For the latter we divide our sample into dwarfs ($z \geq 15$ mag) and giants ($z < 15$) using z-band magnitude (z) following Mahajan et al. (2010). At the redshift of the Coma cluster ($z = 0.023$), $z = 15$ mag corresponds to a $M^* \sim 10^{9.5}$ M$_\odot$.

Figure 3.5(*left*) shows the distribution of the $NUV - r$ colour for the dwarf and giant galaxies in the three different environments in the Coma supercluster. As expected, the fraction of red giants declines, while that of the dwarfs increases as the density of environment reduces. The dwarfs are almost always blue except in the densely populated clusters and groups, although in much fewer numbers than their giant counterparts. Wyder et al. (2007, also see Schawinski et al. (2007)) found the $NUV - r$ distribution of SDSS galaxies to be bimodal around $NUV - r \sim 4$

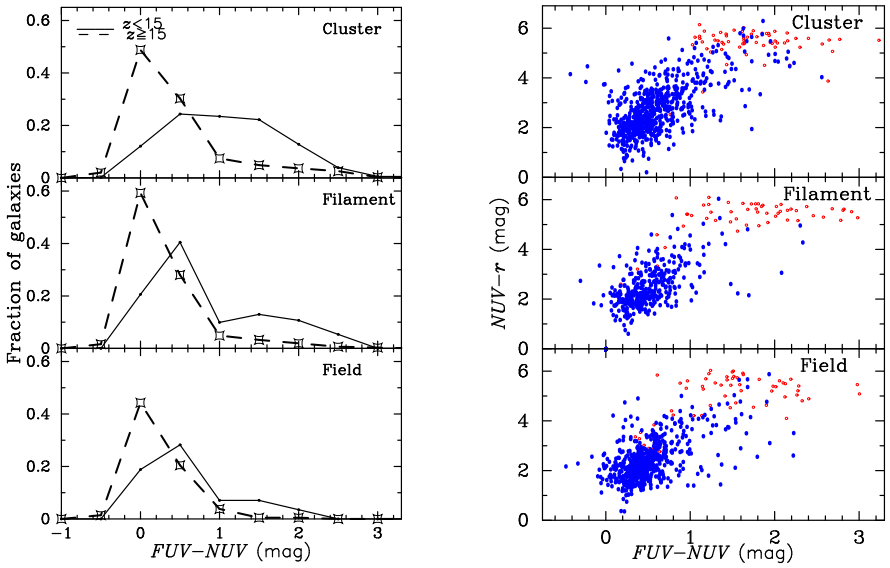

Figure 3.6: *(left) FUV − NUV colour distribution of dwarf ($z \geq 15$) and giant ($z < 15$) galaxies in three different environments in the Coma supercluster. (right) The NUV − r versus FUV − NUV colour-colour distribution of star-forming and passively evolving galaxies in three different environments in the Coma supercluster.*

mag. Using their criteria, we find 38%, 20% and 13% of all UV-detected galaxies in clusters, filaments and field are passive (i.e. $NUV - r > 4$ mag) in our sample, respectively.

Figure 3.5(*right*) shows the distribution of non-AGN galaxies in the $NUV - r$ versus M_r colour-magnitude space for the three different environments. Here we divide the sample into passive and star-forming galaxies around Hα equivalent width (EW) = 2 Å (e.g. Haines et al., 2008). The colour-magnitude relation fitted to passive galaxies in clusters takes the form $NUV - r = 0.94 - 0.22M_r$, with a dispersion of 0.63 mag. This figure evidently shows the strengthening of the red sequence as the environment becomes denser. We note that in all environments galaxies with $NUV - r \lesssim 4$ mag are almost always spectroscopically star-forming. It is also notable that despite a small population of passive galaxies in the filament region, the distinction between the red sequence and the blue cloud is much clearly visible in the filaments relative to the field sample.

These observations are in agreement with the results of Gavazzi et al. (2010), who made use of the M_i vs $g-i$ colour-magnitude relation to show that the red sequence becomes more apparent and the fraction of blue galaxies declines with increasing environmental density. Similar trends have also been observed in and around the Virgo cluster, where using the $NUV - i$ colour Boselli et al. (2014) showed that the red sequence is well established in the low-density outskirts of the cluster, albeit with a much lower fraction of red galaxies relative to their star-forming counterparts.

Overall, in agreement with the literature (e.g. Wyder et al., 2007; Haines et al., 2008) Figure 3.5(*right*) shows that the position of a galaxy in the $NUV - r$ versus M_r colour-magnitude space can be robustly used to distinguish the star-forming galaxies from their passively-evolving counterparts.

The trends seen for $NUV - r$ also continue in the distribution of the $FUV - NUV$ distributions in different environments as shown in Figure 3.6(*left*). The UV colour is a good proxy for young massive stars formed recently in star-forming

galaxies. In the passively-evolving galaxies the FUV emission is dominated by evolved stellar populations, and hence, correlates well with both age and metallicity of the dominating stellar population with surprisingly little scatter (Burstein et al., 1988; O'Connell, 1999; Boselli et al., 2005; Smith et al., 2012). Therefore as expected, the fraction of massive galaxies having $FUV - NUV \gtrsim 1$ mag increases from 27% in the field to 63% in the clusters with the filaments bridging the gap in between with the fraction of red galaxies = 39%. The dwarfs, on the other hand, are relatively bluer than their giant counterparts in all environments, with the fraction of galaxies with $FUV - NUV \gtrsim 1$ mag being 19%, 11% and 7% in the clusters, filament and field region respectively. Segregating galaxies by their SF activity based on EW($H\alpha$), Cortese et al. (2005) also observed similar trends for the galaxies in Abell 1367 such that the star-forming galaxies dominate at high UV luminosities, while the quiescent ones contribute at the faint end of the UV luminosity function.

All galaxies detected in UV are shown in the $NUV - r$ versus $FUV - NUV$ colour-colour distribution in Figure 3.6(*right*). While $NUV - r$ and $FUV - NUV$ become redder together for the blue galaxies (EW(Hα)$\geq$ 2 Å), the $NUV - r$ is always between 5–6 mag for passively-evolving galaxies independent of their $FUV - NUV$ colour. Therefore, just like Figure 3.5(*right*), even the position of a UV-detected galaxy in the UV colour-colour space can be robustly used to distinguish star-forming galaxies from those which are evolving passively (e.g. Gil de Paz et al., 2007).

In a nutshell, in agreement with other studies of the Coma supercluster (Gavazzi et al., 2010; Mahajan et al., 2010) this section shows that not just the hostile environment of clusters, but all components of the cosmic-web influence the broadband colours of the dwarf and giant galaxies in the Coma supercluster.

3.5 Properties of galaxies as a function of distance from clusters and spine of filaments

The observed trend of declining SFR with decreasing cluster-centric distance has been well explored with different datasets in the literature (e.g. Lewis et al., 2002; Gómez et al., 2003b; Balogh et al., 2004). Here we reconfirm this trend in the Coma supercluster by analysing the optical and UV properties of galaxies as a function of their distance from the centre of the nearest cluster or group. We extend this analysis a step further by also investigating the impact of the filament on the properties of galaxies as a function of their distance from the spine of the filaments. In Figure 3.7 we show the median EW(Hα), $FUV - NUV$ and the $g - r$ colour of all as well as non-AGN galaxies as a function of the distance from the nearest group or cluster (section 3.3.2). It is notable that excluding AGN from the sample only changes the normalisation of the radial distribution of galaxies, not the observed trends. Therefore, in the following we discuss the complete sample of galaxies, including AGN.

It is evident that the density of environment has an impact on the colours as well as the EW(Hα) of galaxies, such that the median $FUV - NUV$, as well as the $g - r$ colour of galaxies progressively become bluer, and their emission in Hα increases away from the cluster centre. Beyond $\sim$ 1.5 Mpc from the cluster centre, both colours and EW(Hα) seem to approach a constant value close to the respective

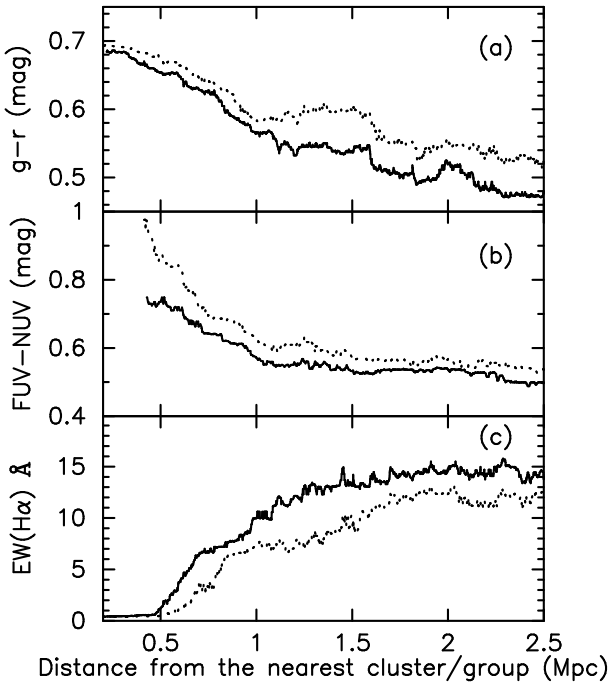

Figure 3.7: (a) $g-r$ colour, (b) $FUV-NUV$ colour and, (c) median EW(Hα) of all *(dotted line)* and non-AGN *(solid line)* galaxies as a function of their distance from the nearest cluster or group. These trends show the expected trend that galaxies progressively become bluer and star-forming further away from the centre of clusters.

medians for the field galaxies. Therefore, in agreement with the literature (Gavazzi et al., 2010; Boselli et al., 2014) Figure 3.7 shows that the fraction of star-forming, blue galaxies in the Coma supercluster increases with the cluster-centric distance.

In Figure 3.8 we show the median EW(Hα), $FUV-NUV$ and the $g-r$ colour of all as well as non-AGN galaxies in the Coma supercluster as a function of their distance from the spine of the filament (section 3.3). While both the colours are constant for galaxies within 1 Mpc of the spine, they decline by $\gtrsim 0.7$ mag beyond it. The trend seen for colours is replicated for the EW(Hα) distribution, which is $\sim$ 13 Å within 1 Mpc of the spine, but increases by another $\sim$ 3 Å beyond 1 Mpc from it. We tested the statistical significance of these trends by dividing the distributions for all the quantities, $g-r$, $FUV-NUV$ and EW(Hα) into three radial bins: $\leq r_{200}$[4], $1-2r_{200}$ and $> 2r_{200}$, respectively. The Kolmogorov-Smirnov (K-S) statistic confirms that the probability for the EW(Hα) distributions in the first and third radial bin to have been drawn from the same parent sample is $2.68e-05$, while the same for the $g-r$ and $FUV-NUV$ colour is $9.76e-08$ and $5.73e-14$, respectively. The same for non-AGN galaxies is $3.34e-04$, $1.61e-07$ and $3.07e-10$, respectively.

Based on these results, we choose to limit the radius of filaments in this work to 1 Mpc as mentioned in section 3.3.3. This is also in agreement with other studies of large-scale filaments based on the SDSS data (Kuutma et al., 2017). A caveat in this analysis, however, is that the SDSS spectra taken with a 3″ diameter fibre only represents the central bulge of large galaxies. Hence, it underestimates the effects

[4] r_{200} is defined as the radius of the sphere centred at the cluster centre within which the matter density is 200 times the critical density of the Universe.

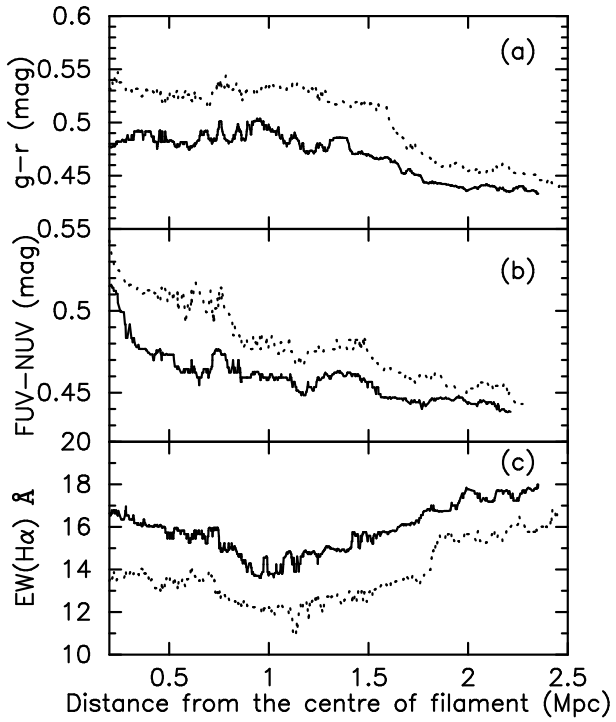

Figure 3.8: (a) $g-r$ colour, (b) $FUV-NUV$ colour and, (c) median EW(Hα) of all *(dotted line)* and non-AGN *(solid line)* galaxies in the Coma supercluster as a function of their distance from the spine of the filament. These trends evidently show that some quenching mechanism comes to play as galaxies close in from field to the spine of filaments.

of quenching due to various environmental mechanisms primarily occurring in the outer regions of large galaxies (Koopmann et al., 2006; Gavazzi et al., 2013).

Together, Figs. 3.7 and 3.8 show that galaxies are not just transformed when they assimilate into dense clusters and groups, but also as they approach the seemingly less hostile environment of the filaments. We discuss the implications of this result in the context of the existing literature in the following section.

3.6 Discussion

3.6.1 The significance of large-scale environment for galaxy evolution

In agreement with the literature, our results show that the large-scale filaments are critical to transformations in a galaxy prior to its assimilation into clusters or groups. With WHIM temperatures of $3-8$ keV and hot gas fraction of $\sim 10\%$ (e.g. Dietrich et al., 2012), filaments are not just passages leading galaxies to their final destination, but offer a unique environment in which the star formation properties of galaxies can change dramatically over a short period of time (Boué et al., 2008; Fadda et al., 2008a; Porter et al., 2008a; Mahajan et al., 2012a).

Using a sample of straight filaments selected from the Two-degree field galaxy redshift survey, Porter et al. (2008a) showed that the statistical parameter η derived from spectra and acting as a proxy for the SFR, is enhanced between 2–3 Mpc from

the edge of the filaments. Moreover, using a sample of Abell clusters ($z \leq 0.12$) selected from the SDSS, Mahajan et al. (2012a) found that the SFR of galaxies is enhanced on the outskirts of clusters, especially the ones which are fed by more filaments. Elsewhere, such an enhancement in star formation is detected in galaxies on filaments feeding clusters using infrared data (Fadda et al., 2008a). These results are intriguing given that most of the star formation in supercluster galaxies at low redshift is contributed by normal galaxies on the periphery of clusters (Haines et al., 2011a).

At high redshift ($z > 0.2$), several authors have made use of multi-wavelength data to investigate large-scale filaments. For instance, Geach et al. (2011) combined the *NUV* data from the *GALEX* with the 24-μm data from the *Spitzer* space telescope to investigate a panoramic 15-Mpc region around the supercluster Cl 0016+16 ($z = 0.55$). In agreement with studies at $z \lesssim 0.1$, their results (also see Coppin et al., 2012; Darvish et al., 2014, 2015) suggest that the star formation rate of galaxies may increase before they fall into clusters. It has also been suggested that the infalling galaxies may experience a phase of obscured star formation before being affected by the cluster environment (Gallazzi et al., 2009).

Owing to their highly coherent motion along linear filaments (González & Padilla, 2009), infalling galaxies are more likely to interact with each other gravitationally relative to their counterparts in field. Such fly-by interactions can trigger a burst of star formation in galaxies falling along filaments (Porter et al., 2008a; Mahajan et al., 2012a). But such an enhancement in SFR of galaxies will also increase their star formation efficiency, hence, assuming no new infall of gas, such galaxies can become redder relative to similar field galaxies even before encountering the cluster environment. The observations presented in this work as well as other studies (Alpaslan et al., 2016a; Kuutma et al., 2017; Kraljic et al., 2018) support this hypothesis.

Along with the trend in galaxy properties as a function of cluster-centric distance, now there is also a growing consensus that the properties of galaxies on filaments change as a function of their distance from the backbone of the filaments. Using data from the SDSS, Kuutma et al. (2017) found a higher elliptical-to-spiral ratio, increasing $g-i$ colour and decreasing SFR for galaxies moving from field to filaments. In fact they found the latter trends in the $g - i$ colour and SFR to be persistent even after separating spiral and elliptical galaxies ($M_r \leq -20$ mag). Using UV-derived SFR for a sample of $\sim 12,000$ galaxies ($z < 0.09$) from the Galaxy and Mass Assembly (GAMA) survey, complete to a stellar mass of $\sim 10^9$ $M_\odot$, Alpaslan et al. (2016a) showed that the galaxies at the core of filaments are more massive and have lower specific SFR (sSFR; SFR/M_*) relative to their counterparts at the edges of field. By using a complementary dataset from the GAMA survey, Kraljic et al. (2018) also reached similar conclusions. These results are in agreement with the comparative analysis of properties of galaxies falling into groups isotropically and along filaments. In this comparison, Martínez et al. (2016) found that the luminosity function of galaxies in filaments is indistinguishable from the galaxies infalling isotropically, yet their sSFR is lower than the latter, suggesting that galaxies in filaments are more strongly quenched.

Recently Kleiner et al. (2017) examined the HI-to-M_* (HI fraction) of galaxies in the nearby (< 181 Mpc) Universe using data from the 6-degree Field Galaxy Survey and stacking HI data from the HI Parkes all sky survey. They found that while the

HI fraction for galaxies with $M_* < 10^{11}$ $M_\odot$ is the same on filaments and in the control sample, vice-versa is true for galaxies more massive than 10^{11} $M_\odot$. Kleiner et al. (2017) suggested that this result is evidence of cold mode accretion of gas in massive galaxies on filaments, owing to their larger potential well. The galaxies on filaments have relatively more HI than their field counterpart. Our results are in broad agreement with Kleiner et al. (2017) such that in this work we have shown that the intermediate density environment prevalent in the filaments affects dwarfs as well as the giants, although this effect is observed to be more pronounced in the latter. But since we do not find enough galaxies observed in HI for the entire Coma supercluster, in this work we can neither support nor reject the hypothesis of cold mode accretion proposed by Kleiner et al. (2017).

The results presented here are also in broad agreement with those of Gavazzi et al. (2013). Using samples of HI-rich and HI-poor late-type galaxies (LTGs; $M_{HI}/M_\odot \geq 9$) in the Local supercluster and part of the Coma supercluster from the ALFALFA survey, they showed that HI-rich LTGs represent $\sim 60\%$ of all LTGs in the low and intermediate-density environments, and drop to zero at the centre of the Coma cluster. On the other hand, the frequency of HI-poor LTGs increases with increasing galaxy density.

3.6.2 How do filaments affect galaxies

The census of observed baryons in the local Universe falls short of their estimated contribution of 5 per cent to the total energy budget by a factor of two. Cosmological simulations indicate that rather than condensing into virialised haloes, the missing baryons reside in the filamentary cosmic-web. The symbiotic relation between the WHIM ($10^5 - 10^7$ K), and the constituent galaxies of the filaments is well represented by the discovery of a bent double lobe radio source (DLRS) in a filament feeding the rich cluster Abell 1763 (Edwards et al., 2010a). Assuming that the bend in the jet of the DLRS is due to the ram-pressure experienced by it 3.4 Mpc away from the centre of the cluster, Edwards et al. (2010a) constrained the density of WHIM to be a few times 10^{-29} gm cm^{-3}, in agreement with the literature, thereby evidently showing that environmental processes such as ram-pressure stripping may operate much farther away from high-density environment of clusters.

By studying the spectroscopic properties of 28 star-forming galaxies ($z \sim 0.53$) in the COSMOS field, Darvish et al. (2015) found that within uncertainties, the EW, EW versus sSFR relation, EW versus M_* relation, line-of-sight velocity dispersion, dynamical mass, and stellar-to-dynamical mass ratio are similar for filament and field star-forming galaxies. Yet on average, star-forming galaxies on filaments are more metal-enriched ($0.1 - 0.5$ dex) relative to their field counterparts. Darvish et al. (2015) suggest that the high metallicity may have been caused by the inflow of the enriched intrafilamentary gas into galaxies residing on filaments. However, these high redshift observations are in conflict with the results of Hughes et al. (2013) who found that even though gas-poor galaxies in the Virgo cluster ($z \sim 0$) are typically more metal-rich, statistically the M_*-metallicity relation is independent of environment. Hughes et al. (2013) also demonstrated that removal of gas from the outer regions of disc galaxies may increase the observed metallicity by ~ 0.1 dex.

Darvish et al. (2015) also showed that electron densities are significantly lower by a factor of $\sim$ 17 in filament star-forming galaxies compared to those in the

field, possibly because of a longer star-formation timescale for filament star-forming galaxies. This, and other aforementioned studies complement the results found in this work and highlight that galaxy properties are not just shaped by M_* and the large-scale galaxy density, but also the tidal effects of the anisotropic cosmic-web resulting from the interactions between the intra-filamentary gas and galaxies.

3.6.3 Epilogue

Several innovative techniques such as gravitational lensing (Van Waerbeke et al., 2014), stacking of optical photometric data (Zhang et al., 2013), and stacking of x-ray data (Fraser-McKelvie et al., 2011) are now being employed to discover and characterise various aspects of the cosmic-web. Therefore, observations such as those presented here are crucial not just for strengthening our models of the formations and evolution of the Universe, but also to serve as a benchmark to compare with discoveries and trends observed at higher redshift. In the near future, state-of-the-art technology and global observational projects will play a key role in enhancing our understanding of the cosmic-web. To prepare ahead for these data, while some studies are utilising simulations to examine the evolution of the cosmic-web properties with redshift (Gheller et al., 2016), others are trying to predict the 21-cm signal of WHIM which may be detected by the Square Kilometer Array (SKA) (Horii et al., 2017, also see Tejos et al. (2016)). Elsewhere, x-ray observations of large-scale filaments have been reported (Werner et al., 2008; Eckert et al., 2015). With an ever-expanding database of the known large-scale structures at different epochs, we can hope to understand the evolution of the environment and properties of galaxies in filaments in the near future.

3.7 Summary

We have utilised the optical data from the SDSS DR 12 and UV data from the *GALEX* survey to present a catalogue of UV detected galaxies in the Coma supercluster. We have used DisPerSe to characterise the large-scale filaments, and HDBSCAN algorithm to identify the groups and clusters of galaxies in the Coma supercluster. The key results reported in this work are:

- The position of a galaxy in the $NUV-r$ versus r colour-magnitude space and in the $FUV-NUV$ versus $NUV-r$ colour-colour space can be robustly used to separate passively-evolving galaxies from their star-forming counterparts in all environments: clusters, filaments and field.

- Dwarf galaxies are almost always blue except in the dense interiors of the clusters and groups. On the other hand, most of the giants are red in all environments in the Coma supercluster, but their fraction decreases with the environmental density. These trends are seen for the $FUV-NUV$, as well as the $NUV-r$ colour.

- The $g-r$ and $FUV-NUV$ colour and EW(Hα) for galaxies vary as a function of their distance from the nearest cluster or group viz., galaxies become redder and emission in Hα declines with their distance from the nearest maximum in density.

- Within a radius of 1 Mpc from the spine of the filament, galaxies become redder, and the median EW(Hα) declines closer to the spine of the filament. This transformation in $g - r$, $FUV - NUV$, and Hα emission of galaxies is statistically significant, and therefore, evidently depicts the key role played by the large-scale filaments in shaping properties of galaxies.

Chapter 4

Study of effects of large-scale filament environment in simulations

This chapter is based on Singh, A., Mahajan, S. and Bagla, J. S. "Study of galaxies in large-scale filament environment in EAGLE simulation", under review in MNRAS since January, 2020.

4.1 Introduction

There is plenty of evidence in the literature to suggest that the galaxies on filaments have higher star formation rate relative to their counterparts in clusters and field (Porter & Raychaudhury, 2007b; Fadda et al., 2008b; Porter et al., 2008b; Mahajan et al., 2012b, 2018; Vulcani et al., 2019). Furthermore, galaxies on filaments are found to be more metal-rich (Darvish et al., 2015), as well as host more satellite galaxies (Guo et al., 2015). Studies of galaxy pairs on filaments indicate a significant alignment between the pair axis and the axis of the filament on which they reside (Lambas et al., 1988; Donoso et al., 2006; Mesa et al., 2018). In particular, Mesa et al. (2018) found that the alignment for pairs of elliptical galaxies is stronger than the pairs comprising one or both spiral galaxies, especially within 200 h^{-1} kpc of the spine of the filament.

Several recent studies suggest that the properties of galaxies on filaments change as a function of their distance from the cylindrical axis of the filament. Using optical spectroscopic and photometric data from the Galaxy And Mass Assembly (GAMA) survey and the Horizon-AGN simulation suite, Kraljic et al. (2018) found that galaxies tend to become passive closer to the filament axis. Multi-wavelength data from the GAMA survey were also used by Alpaslan et al. (2016b) to show that galaxies ($M_* > 10^9$ $M_\odot$; $z < 0.09$) become less star forming and more massive with decreasing distance from the filaments' axis. Mahajan et al. (2018) studied the Coma supercluster ($z \sim 0.023$) using similar optical data from the Sloan Digital Sky Survey (SDSS) and ultraviolet (UV) data from the Galaxy Evolution Explorer (*GALEX*) mission. One of their major results is that the colours of galaxies become redder and emission in the Hα line decreases on approaching the spine of the filament. Similar

results have also been obtained for galaxies at higher redshift (Chen et al., 2017; Malavasi et al., 2017; Laigle et al., 2018b; Luber et al., 2019).

In the last few years, state-of-the-art simulations have been employed to understand the symbiotic relationship between the large-scale structure and its galaxy constituents. Large cosmological simulations not just serve as a testbed for validating various theories of structure formation and evolution, but also serve as a laboratory to predict the properties of the yet to be observed constituents of the Universe. For instance, Martizzi et al. (2018) used the IllustrisTNG simulations to show that the filaments contain more star-forming gas, as well as higher mass fraction of such gas relative to clusters. In a study based on the Horizon MareNostrum simulation, Gay et al. (2010) explored the properties of galaxies at redshift of $z = 1.5$ (box size of 50 h^{-1} Mpc), and found that the G-K colour of galaxies becomes redder on approaching the spine of the filaments.

Even though the present-day simulations are able to produce global trends in the properties of galaxies, they depend upon recipes to mimic effects of various sub-grid physical processes at play. Since these parameters can not be found using first principles, it is critical to understand the variation in properties of galaxies as a continuous function of their environment in order to validate different sub-grid recipes. The Evolution and Assembly of GaLaxies and their Environment (EAGLE; Schaye et al., 2015; Crain et al., 2015; McAlpine et al., 2016; Trayford et al., 2016; Correa et al., 2017) is one such suite of simulations which has been used to study various aspects of evolution of galaxies in recent years (Trayford et al., 2015; Furlong et al., 2015; De Rossi et al., 2017a). A very useful aspect of the EAGLE simulations is that the calibration of the feedback parameters is performed by broadly matching the galaxy stellar mass function (GSMF) at $z \sim 0$, maintaining reasonable galaxy sizes. Through this new implementation, EAGLE can reasonably match and predict multi-wavelength observations at large scales, making them an ideal resource to study galaxies in different environments.

We describe our methodology in the next section, followed by the results of our analysis in section 4.3, which are discussed in the context of the existing literature in section 4.4. We finally conclude in section 4.5.

4.2 The EAGLE Simulations

In this work, we employ data produced by the EAGLE simulation (Schaye et al., 2015; McAlpine et al., 2016), which is a suite of hydrodynamical simulations run with a modified version of the Gadget-3 code. The simulation uses a flat ΛCDM model with parameters taken from the Planck mission (Planck Collaboration et al., 2014) results: $\Omega_\Lambda = 0.693$, $\Omega_\mathrm{m} = 0.307$, $\Omega_\mathrm{b} = 0.04825$, $\sigma_8 = 0.8288$, $n_\mathrm{s} = 0.9611$, $Y = 0.248$, and $H_0 = 67.77$ km s^{-1} Mpc^{-1} (i.e. $h = 0.6777$). Specifically, we use the reference model RefL0100N1504 with co-moving box length of 100 h^{-1} Mpc. The total number of particles in the RefL0100N1504 run is 2×1504^3, giving an initial gas particle mass (m_g) of 1.81×10^6 M$_\odot$, and a dark matter particle mass of 9.70×10^6 M$_\odot$, respectively. by using state-of-the-art numerical techniques, EAGLE differs from other simulations in its implementation of energy feedback from stars, i.e. it does not distinguish between core-collapse supernovae, stellar winds and radiation pressure. In this study we have used the snapshot at $z = 0.1$ to create mock observational data.

The physical parameters

Star formation in the EAGLE simulations is implemented using the Kennicutt-Schmidt relation (Kennicutt, 1998a) between the gas mass density and the star formation density (Schaye & Dalla Vecchia, 2008). In particular, the star formation rate decreases with increasing metallicity above the density threshold given by Schaye (2004) as:

$$n_{\rm H}^{*} = 10^{-1}{\rm cm}^{-3}\left(\frac{Z}{0.002}\right)^{-0.64} \tag{4.1}$$

where, Z is the gas metallicity. The simple stellar populations represented by these stellar particles follow the Chabrier initial mass function (IMF). Furthermore, in order to prevent artificial fragmentation, a density dependent temperature floor ($T_{\rm eos}(\rho_{\rm g})$) is applied following the equation of state : $P_{\rm eos} \propto \rho_{\rm g}^{\gamma_{\rm eos}}$ with $\gamma_{\rm eos} = 4/3$, where P is the pressure, $\rho_{\rm g}$ is the gas density and γ is the ratio of the heat capacities. The temperature floor is normalised to $T_{\rm eos} = 8000$ K at $n_{\rm H} = 0.1$ cm^{-3} to mimic gas in cold phase. When the gas density exceeds $n_{\rm H}^{*}$, and the temperature $\log_{10}(T/K) < \log_{10}(T_{\rm eos}/K) + 0.5$, the gas particles are assigned a star formation rate (SFR):

$$\dot{m}_{*} = m_{\rm g}\ A\ (1\ M_{\odot}pc^{-2})^{-n}\ (\frac{\gamma}{G}f_{\rm g}P)^{(n-1)/2}, \tag{4.2}$$

where, G is the gravitational constant, $\gamma = 5/3$ is ratio of specific heats and $f_{\rm g}$ is the fraction of mass in the gas, and is kept at 1.0 for the RefL100N1504 model. Parameters $n = 1.4$ and $A = 1.515 \times 10^{-4}$ M$_{\odot}$ yr^{-1} kpc^{-2} are estimated from the fit to observational data (Kennicutt, 1998a).

The rates of radiative cooling and heating are computed on an element-to-element basis in the presence of Haardt & Madau (2001) ultraviolet or x-ray ionizing background and the cosmic microwave background. Eleven elements (H, He, C, N, O, Ne, Mg, Si, S, Ca and Fe) which are important for calculating cooling rates at $T > 10^4$ K (Wiersma et al., 2009b) along with the total metallicity are tracked in the simulations.

Parameter	Description
M_{*}	Total stellar mass within the aperture (M$_{\odot}$).
$M_{\rm gas}$	Total gas mass within the aperture (M$_{\odot}$).
$M_{\rm tot}$	Total subhalo Mass (M$_{\odot}$)
x,y,z	Position of subhalo
SFR	Star formation rate within the aperture.
u	u band without dust attenuation.
g	g band without dust attenuation.
r	r band without dust attenuation.

Table 4.1: The physical parameters from the EAGLE simulation used to study the properties of galaxies.

The simulations incorporate various sub-grid feedback mechanisms including stellar winds from asymptotic giant branch (AGB) stars, supernovae (both core collapse and type IA; Wiersma et al., 2009a) and active galactic nuclei (AGN; Schaye et al., 2015). The prompt stellar feedback is implemented in a manner similar to Dalla Vecchia & Schaye (2012). In this 'stochastic feedback' model, the fraction of

energy ($f_{\rm th}$) released by the core collapse supernovae is given by:

$$f_{\rm th} = f_{\rm th,min} + \frac{f_{\rm th,max} - f_{\rm th,min}}{1 + \left(\frac{Z}{0.1Z_{\odot}}\right)^{n_Z} \left(\frac{n_{\rm H,birth}}{n_{\rm H,0}}\right)^{-n_n}}, \tag{4.3}$$

where, $f_{\rm th,max}$ and $f_{\rm th,min}$ are the asymptotic values of $f_{\rm th}$ and $n_{\rm H,birth}$ is the density of the parent gas particle. In this model, n_n, n_Z, and $n_{\rm H,0}$ are free parameters. This fraction is injected into the neighbouring cells 30 Myr after the birth of the stellar particle. The thermal energy ejected by a star is distributed stochastically isotropically, resulting in temperature change of $\Delta T = 10^{7.5}$ K.

When the mass of a halo reaches 10^{10} $M_{\odot}$, a gas particle at the centre of the potential well is converted into a seed black hole with a mass of 10^5 h^{-1} $M_{\odot}$ (Springel et al., 2005). The accretion of matter on the central black hole is based on a modified Bondi-Hoyle model (Schaye et al., 2015). A fraction of 0.015 of the rest mass energy of the matter accreted on the central black hole is returned to the surrounding thermally as a jump of $\Delta T = 10^{8.5}$ K.

All the free parameters related to physical processes are calibrated to reproduce the GSMF and galaxy sizes at $z = 0.0$.

Properties of galaxies

In EAGLE simulations, the dark matter haloes are identified using the friends-of-friends (FOF) algorithm (Einasto et al., 1984), such that the dark matter particles separated by less than 0.2 times the mean inter-particle separation are bound into a single halo. The individual galaxies are identified using the SUBFIND algorithm (Springel et al., 2001; Dolag et al., 2009), which labels the galaxy closest to the centre of the parent halo as the central galaxy, and other haloes inside the parent as satellite galaxies.

It is difficult to quantify the mass or luminosity of galaxies in simulations using the SUBFIND algorithm, because it assigns the mass of unbound particles to the central galaxy. This leads to an extended stellar distribution for such galaxies. Hence, in this work we use the stellar mass of the subhalo obtained within an aperture of 30 kpc in physical units (pkpc, henceforth), centred at the minima of the subhalo potential (Trayford et al., 2015; Schaye et al., 2015). The choice of aperture is motivated by the fact that 3-D aperture of 30 kpc matches the results obtained using 2-D Petrosian aperture (Schaye et al., 2015).

The EAGLE simulation uses the Bruzual & Charlot (2003) population synthesis models for each particle to obtain the spectral energy distribution (SED) of galaxies. The spectra convolved with the filter response function within 30 pkpc aperture gives the broadband colours of the galaxies in optical and near infrared wavebands (Doi et al., 2010; Hewett et al., 2006). We employ some of these rest-frame colours to study the properties of galaxies. A full list of all the variables used in our analysis is provided in Table 4.1. In this work, we use the SFR inside 30 kpc in physical units centred at minima of subhalo potential to explore such trends. The SFR has been measured using the mass of dense gas in the subhalo (Schaye & Dalla Vecchia, 2008).

Studies of large-scale filaments based on observations mainly focus on the outskirts of massive clusters (e.g. Dolag et al., 2006; Porter et al., 2008b; Mahajan

et al., 2012b), or superclusters[1] (e.g. Porter & Raychaudhury, 2007b; Haines et al., 2011b; Mahajan et al., 2018), which often comprise two or more massive clusters and groups with large-scale filaments passing through them. In order to mimic such superclusters using the EAGLE simulations, in this work we identify systems where two massive clusters may be connected via filaments. The EAGLE simulations however have a small box size (the largest box is 100 h^{-1} Mpc on each side), hence not many superclusters are expected to have formed in it (Bagla & Ray, 2005; Bagla et al., 2009). Therefore, in order to make the best use of the available data, we generated mock observations by identifying the positions of haloes with mass $\sim 10^{14}$ $M_\odot$. Nine such clusters were found, resulting in 36 ($^9C_2$) potential slices comprising superclusters. Table 4.2 lists the properties of these haloes ($z = 0.1$), which are analysed further, which gives us a sample of 294,780 galaxies. To find the underlying structure of the cosmic-web, we restricted ourselves to galaxies with $M_*/M_\odot \geq 10^9$ (within 30 pkpc aperture). This choice of stellar mass limit is motivated by earlier work which showed that for the RefL0100N1504 run, simulations are well matched to the observations for $M_*/M_\odot \geq 10^9$ (Schaye et al., 2015; Trayford et al., 2016).

grpid	$M_{\rm tot}/M_\odot$	R (pkpc)	x (Mpc)	y (Mpc)	z (Mpc)	Number of subhaloes
27000000000000	3.4×10^{14}	1426.70	5.72	75.61	47.48	17101
27000000000001	1.7×10^{14}	1135.12	18.12	79.88	53.51	9942
27000000000002	2.89×10^{14}	1349.73	9.12	35.03	54.52	9152
27000000000003	2.9×10^{14}	1356.48	52.43	5.00	20.12	7430
27000000000004	1.85×10^{14}	1162.48	10.96	81.29	54.89	7365
27000000000005	1.38×10^{14}	1054.56	77.85	76.97	42.28	6909
27000000000006	1.38×10^{14}	1055.64	76.13	89.23	41.89	6191
27000000000007	1.11×10^{14}	981.45	61.25	33.08	20.23	6183
27000000000008	1.00×10^{14}	948.02	84.83	47.33	8.14	3190

Table 4.2: Clusters used for analysis. The columns are: (i) grpid: group id of the group detected by the friends-of-friends algorithm. (ii) $M_{\rm tot}$: mass (M_{200}) of the group. (iii) R: radius of the group halo. (iv) x, (v) y and (vi) z are the respective coordinates of group halo, and, (vii) number of subhaloes identified by the SUBFIND algorithm.

4.2.1 Mock Observations

Although simulations contain 3-dimensional (3D, henceforth) information, we created 2D projections of 3D slices in order to compare our results with the observations. Furthermore, the 2D analysis allows us to artificially expand our dataset by rotating the central axis of the supercluster systems found in the simulation box as described below. Motivated by observational studies of supercluster filaments crossing clusters of galaxies (e.g. Dolag et al., 2006; Porter et al., 2008b; Mahajan et al., 2012b, 2018), we begin by considering each cluster pair system as a possible supercluster candidate.

In order to generate a slice of these data for making mock observations, the coordinate system was changed by translating the origin to the centre of the line

[1]In this work a filament or a network of filaments bound by clusters of galaxies on opposite ends is referred to as a 'supercluster'.

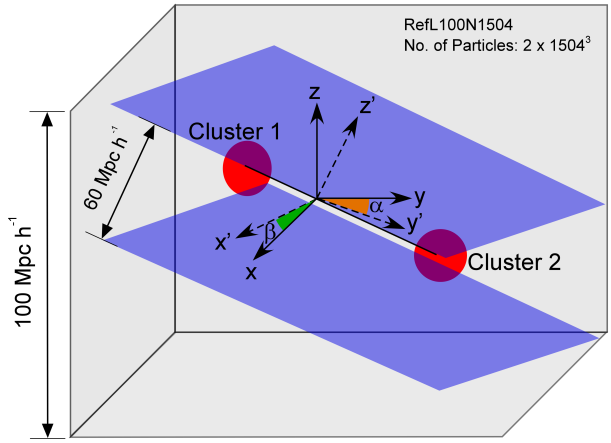

Figure 4.1: The setup employed for creating the slices for mock observations. A slice is cut from the simulation box around each pair of clusters ($M_{200}/M_{\odot} > 10^{14}$), by translating the original coordinate system (O), such that the centre of the modified coordinate system coincides with the centre of the line joining the two clusters. The system is then rotated about this axis, and angles α, and β are randomly generated. This new coordinate system is referred in the text as O'. Throughout this paper, environment of galaxies is characterised based on the 2D projection of 36 such slices in the O' frame of reference.

joining the two clusters in the system. The system is then rotated by keeping one axis fixed with the line joining the two clusters, and choosing the orientation of the remaining two axes randomly. Laigle et al. (2018a) have shown that a 60–200 Mpc thick slice can capture real 3D filaments even in their 2D projection. Therefore, in order to characterise the environment in 2D projections, we choose a slice of co-moving width 60 Mpc with the normal perpendicular to the line joining the cluster pair as shown in Figure 4.1. This choice of width compliments the width of the Coma supercluster region studied in Mahajan et al. (2012b, 2018). In the following, we refer to this transformed frame as O′.

4.2.2 Classification of Environment

The cosmic-web can be broadly segregated into different components based on the density of galaxies. Characterisation of these environments requires identifying the local topology and clustering of the constituents. In this study, we follow an approach similar to that used in Mahajan et al. (2018, hereafter SM18) to characterise environment into groups and clusters, filaments and field, respectively.

In order to identify filaments in the 2D projected slices, we employ the Discrete Persistent Structures Extractor (DISPERSE; Sousbie, 2011) algorithm. DISPERSE uses the Morse theory and persistence theory to map the persistence of critical points obtained by measuring density at discrete points to the underlying topology. It identifies features such as nodes, filaments, and saddle points using just one parameter. This parameter called the persistence threshold crudely corresponds to the level of complexity to be retained while identifying structures in a distribution. We direct the reader to SM18 and Sousbie (2011) for detailed application and working of the algorithm, and choice of parameters.

The persistence threshold above which all the critical points are retained for

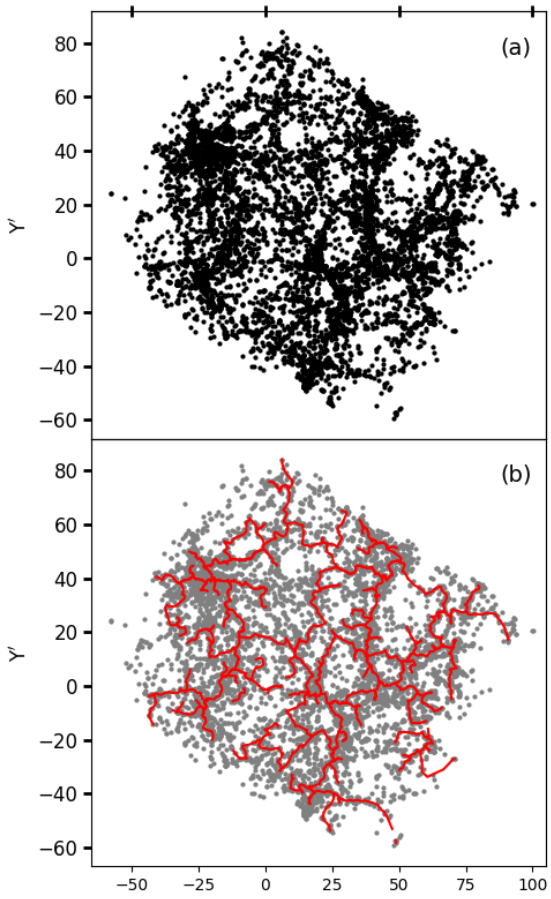

Figure 4.2: The projected position of galaxies in one of our slices. (b) Same as (a), with *red lines* overplotted to represent the filaments identified by DISPERSE.

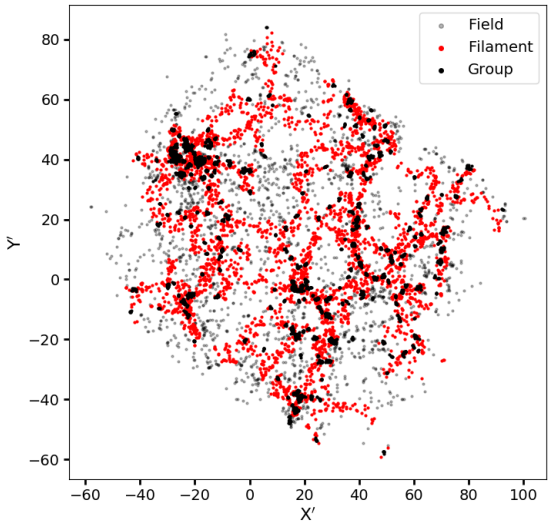

Figure 4.3: Projected position of galaxies in the same slice shown in Figure 4.2, with each point labeled with the environment it belongs to. The radius for the filaments is assumed to be 2 Mpc (see text for details). The *black, red*, and *grey points* represent galaxies in groups and clusters, filaments, and field, respectively.

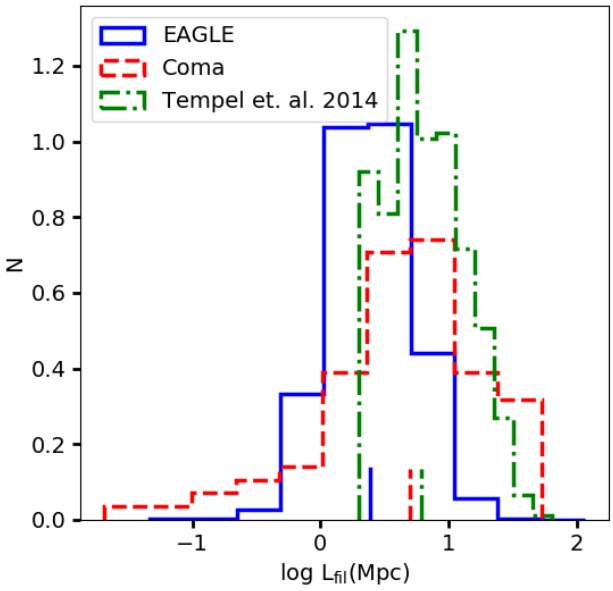

Figure 4.4: Comparison between the distribution of length of filaments in a study based on the SDSS data (Tempel et al., 2014), the Coma supercluster (Mahajan et al., 2018) and our sample. The bars shown on the bottom panel represent the median of the respective distributions. The filaments identified in both the observational datasets are found to be longer relative to the filaments from the EAGLE simulations in this work.

analysis is usually taken to be 3-5 σ, where σ is the standard deviation. It suppresses the selection noise and picks relatively denser and longer filaments (Sousbie, 2011). In this work, we choose the significance threshold of 3σ which segregates the noise from the points used for analysis in this work for each mock observation.

Filaments are obtained by applying DISPERSE on the distribution of galaxies in the O′ projection. In Figure 4.2(b) we show the filaments identified for a representative slice. We identify filament galaxies as those which (i) do not belong to clusters or groups, and (ii) are ≤ 2 Mpc from the spine of the filament. The choice of filament radius is driven by the fact that $\sim 75\%$ of all galaxies found within 5 Mpc of the spine of the filaments lie ≤ 2 Mpc from the central axis (also see Sec. 4.3.1).

In order to identify the galaxies in each slice, we use EAGLE's group catalogue to identify the friends-of-friends groups with total mass, $M_{\rm halo} > 10^{12.5}$ M$_\odot$, and comprising at least four galaxies with $M_*/M_\odot > 10^9$ (Schaye et al., 2015). The galaxies which are not linked to groups, clusters or filaments were classified as field galaxies. In Figure 4.3 we show the distribution of galaxies in different environments in one of the slices.

4.3 Properties of galaxies on filaments

In order to study the properties of galaxies in different environments in the EAGLE simulations, we stack all the 36 slices obtained from mock observations. In the following we analyse the trends in the properties of galaxies, in particular the

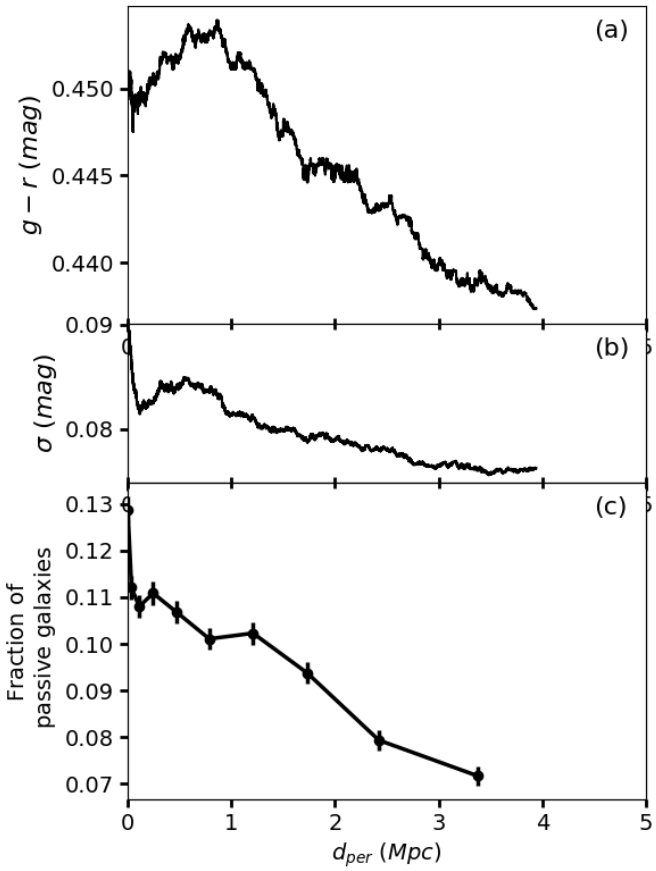

Figure 4.5: The (a) $g-r$ colour of galaxies, (b) median absolute deviation (MAD) of $g-r$ colour shown in (a), and (c) fraction of passive galaxies ($sSFR < 0.01$ Gyr) on filaments as a function of their distance from the spine of the filament. Galaxies become redder and the fraction of passive galaxies increases with decreasing distance from the spine of the filaments.

galaxies on filaments with respect to their counterparts residing in denser and rarer regions of the space.

4.3.1 The large-scale filaments

In Figure 4.4 we compare the distribution of length of filaments from our stacked sample generated from the EAGLE simulations, with the filaments in the Coma supercluster (SM18), as well as another distribution of filaments obtained from the SDSS dataset (see figure 11 of Tempel et al., 2014). While SM18 identified the filaments in 2D projections, just like this work, the filaments of Tempel et al. (2014) were identified from the 3D distribution of galaxies.

To compare these distributions, we use the Welch's t-test (Welch, 1947), which tests for the hypothesis that two distributions have different means. We find that the distribution of lengths of filaments from EAGLE simulation when compared with the filaments from SM18 and Tempel et al. (2014) gives p-values < 0.01 in both cases. The filaments found in both the observational datasets are found to be relatively longer than the filaments found in the EAGLE simulations. However, this result can only be considered qualitatively because of the different redshifts of the samples, and

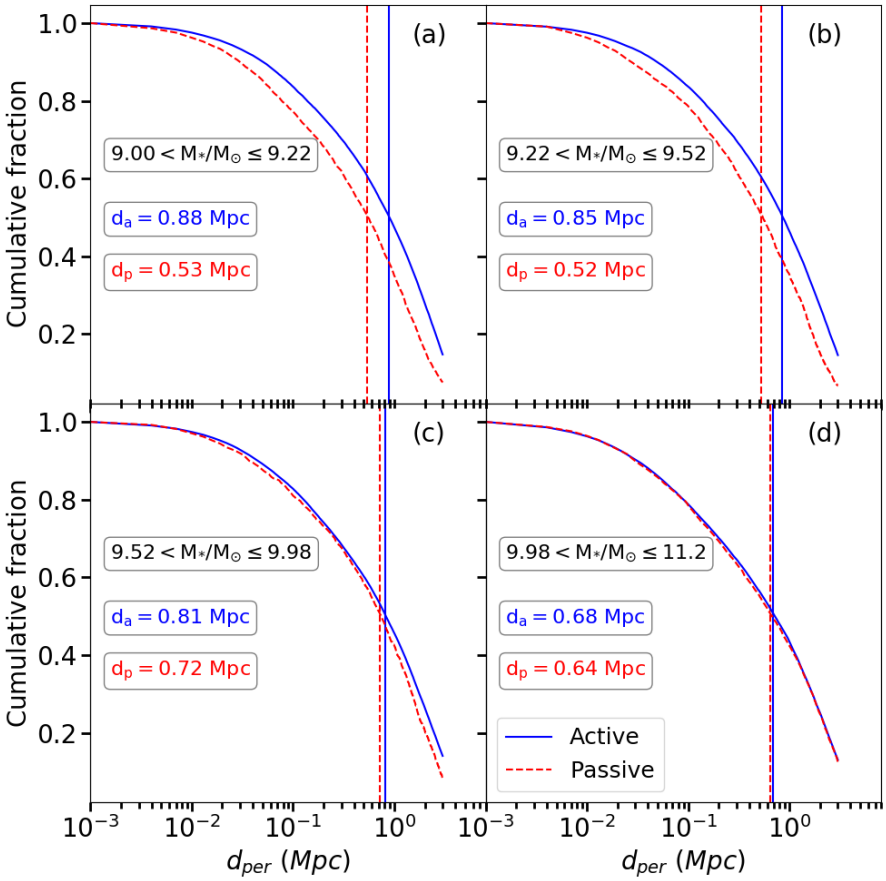

Figure 4.6: The cumulative distributions of active and passive galaxies are shown as a function of $d_{\rm per}$ for different mass bins. The *vertical dashed lines* correspond to median value for $d_{\rm per}$ for the active (*dashed red line*) and the passive (*solid blue line*), respectively. The four mass bins are chosen to have the same number of galaxies in each bin. The median of the distribution for the active galaxies in the three low stellar mass bins (a)-(c) have value close to 1 Mpc, i.e. the radius of filaments comprising majority of the galaxies on the cosmic-web. The distributions for the active and passive galaxies in these three mass bins are also statistically distinct. On the other hand, the galaxies in the highest mass bin are statistically similar to each other. These distributions evidently show that at fixed stellar mass, passive galaxies lie closer to the spine of the filament than their active counterparts.

the fact that the procedure for finding the filaments is dependent on the algorithms with free parameters which can influence the distribution of length of filaments (Libeskind et al., 2018).

Colours of galaxies

Broadband optical colours are often a good representative of the age of the most dominant stellar population, and hence, the age of galaxies. Therefore, in order to study the impact of the filament environment on the evolution of galaxies we analyse their colour as a function of increasing environmental density. In Figure 4.5 we show the running median of the $g-r$ colour of galaxies, median absolute deviation (MAD) of $g-r$ colour, and the fraction of passive galaxies (sSFR < 0.01 Gyr^{-1}; Schaye

Table 4.3: The Welch test statistical probability for the likelihood that the galaxies in bin x are the same as bin y. The bins are chosen in ascending order of the distance of galaxies from the spine of the filament such that, bin 1: $0 \leq d_{\rm per}/{\rm Mpc} \leq 1$, bin 2: $1 < d_{\rm per}/{\rm Mpc} \leq 2$ and bin 3: $2 < d_{\rm per}/{\rm Mpc} < 5$.

Parameter	bin1-bin2	bin2-bin3	bin1-bin3
$g-r$	1.497×10^{-23}	1.554×10^{-27}	3.059×10^{-82}
sSFR	0.310	8.711×10^{-25}	2.871×10^{-44}
M_{gas}/M_{tot}	0.058	5.401×10^{-14}	1.341×10^{-31}
M_*/M_{tot}	9.859×10^{-108}	0.021	5.094×10^{-158}
Z_{NSF}	3.845×10^{-127}	2.321×10^{-49}	$\lll 0.0$
Z_{SF}	0.871	1.216×10^{-26}	5.194×10^{-44}

et al., 2015), as a function of their perpendicular distance from the spine of filaments ($d_{\rm per}$). We find that the galaxies become redder and more passive closer to the spine of filaments within a radius of 2 Mpc from the filament axis. Specifically, the passive fraction increases from 8% at a distance of ~ 2 Mpc from the spine of the filaments to 11.5% at the centre of the filaments. Welch's t-test statistic shows that the colour of galaxies at $d_{\rm per} < 1$ Mpc is statistically different from their counterparts farther away from the spine of the filaments (Table 4.3). The MAD quantifies the width of the distribution at different $d_{\rm per}$, essentially showing that the distributions are broader closer to the spine of the filaments where most of the galaxies lie. This result is in tune with the findings from observations (Alpaslan et al., 2016b; Kuutma et al., 2017; Kraljic et al., 2018; Bonjean et al., 2019), as well as other simulations (Gay et al., 2010). Such trends with $d_{\rm per}$ have helped in constraining the radius of filaments to $1-2$ Mpc (Bonjean et al., 2018; Mahajan et al., 2018; Tanimura et al., 2019).

The stellar mass of galaxies is well known to correlate with the environmental density. Hence in order to break this degeneracy between M_* and environment, in Figure 4.6 we show the cumulative fraction for the active and passive galaxies in filaments separately in four mass bins: $10^9 < M/M_\odot \leq 10^{9.22}$, (b) $10^{9.22} < M/M_\odot \leq 10^{9.52}$, (c) $10^{9.52} < M/M_\odot \leq 10^{9.98}$ and (d) $10^{9.98} < M/M_\odot \leq 10^{11.2}$. The mass bins are chosen to include the same number of galaxies in each bin. For the three low stellar mass bins ((a)-(c)), the median $d_{\rm per}$ for the active galaxies' distributions have values close to 1 Mpc, i.e. the radius of filaments comprising $\gtrsim 50\%$ of the galaxies on the cosmic-web. We further tested for statistical differences among the distributions in each panel using the Kruskal-Wallis (KW) test (Kruskal & Wallis, 1952). The KW statistic is a non-parametric rank-based test which assumes independent observations, continuous variability and same shape for the two distributions. For the four panels in Figure 4.6 the KW test yields a probability of 5.67e-82, 1.10e-52, 2.85e-06, and 0.31 in favour of the hypothesis that the two distributions had the same medians. Based on this analysis we also conclude that at fixed stellar mass, passive galaxies lie closer to the spine of the filament than their active counterparts.

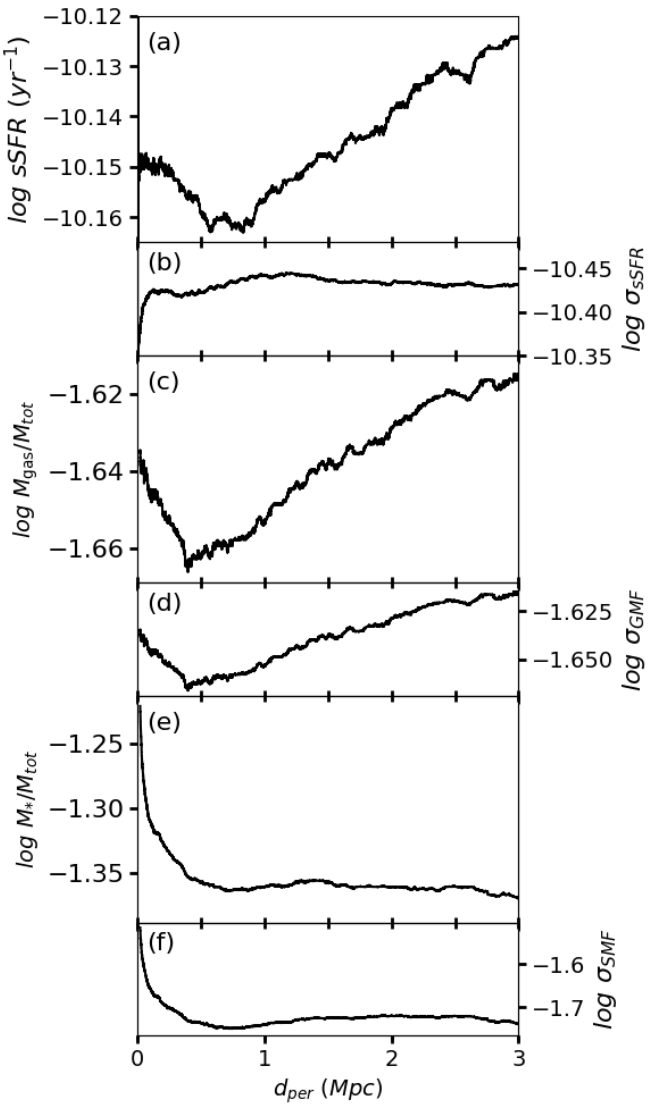

Figure 4.7: The (a) median sSFR, (c) gas mass fraction, and (e) stellar mass fraction as a function of $d_{\rm per}$. Plots (b), (d) and (f) show the MAD for sSFR, gas mass and stellar mass respectively. M_{tot} is the sum of M_{gas}, M_* and M_{dm} inside the 30pkpc aperture of each galaxy. Outside a radius of 0.5 Mpc, the sSFR and the gas mass fraction decrease with decreasing distance from the spine of the filaments, while the stellar mass function remains constant. Within a radius of ~ 0.5 Mpc, the trend seems to reverse, and all three quantities exhibit enhancement with decreasing $d_{\rm per}$, indicating that the intrafilamentary medium condensing closer to the spine of the filament may be responsible for increasing the SFR of filament galaxies with $d_{\rm per} < 0.5$ Mpc.

Star formation in filament galaxies

The star formation rate of filament galaxies is enhanced relative to their counterparts in clusters as well as the field (Fadda et al., 2008b; Mahajan et al., 2012b). SM18 showed that while the optical and UV colours becomes bluer, the equivalent width of the Hα line increases for the filament galaxies moving away from the spine of the filaments.

In Figure 4.7(a)-(b) we show the variation of the running median of the specific star formation rate (sSFR) as a function of the perpendicular distance ($d_{\rm per}$) to the spine of the filaments and the MAD for the same. On approaching the filaments, the sSFR decreases slowly until ~ 1 Mpc from the spine of the filaments, and thereafter increases again closer to the central axis. Table 4.3 confirms the observed trends by showing that the sSFR distribution for galaxies within $\lesssim 2$ Mpc is different from their counterparts further away from the spine of the filaments. This result correlates well with the $g-r$ colour of galaxies becoming bluer in Figure 4.5(a). Furthermore, these results support the findings of Liao & Gao (2019), who have suggested that the galaxies on filaments can accrete intrafilamentary gas to feed star formation, and the density of this gas should also increase with decreasing distance from the spine of the filaments.

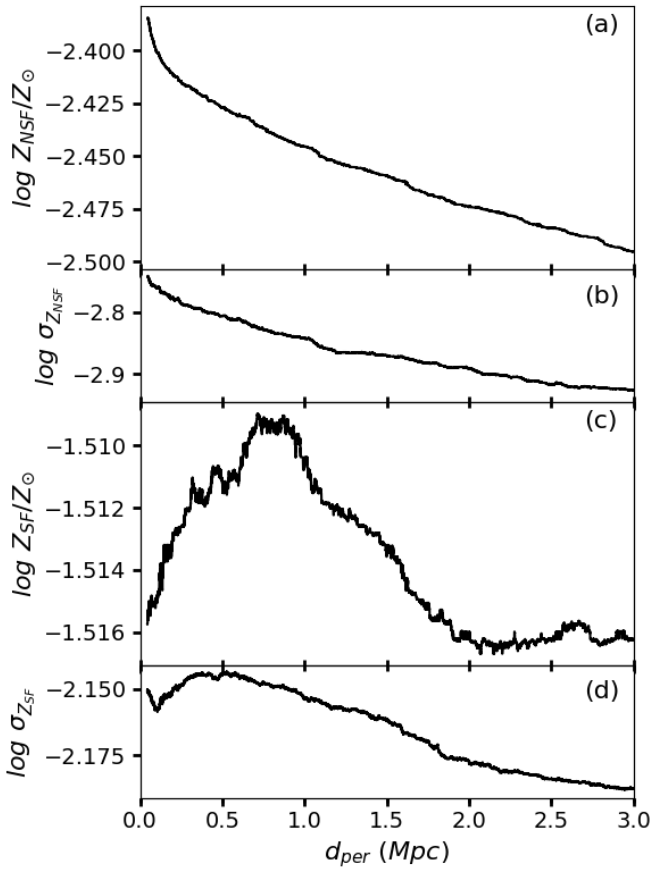

Figure 4.8: The median metallicity of (a) the star forming gas ($Z_{\rm SF}$) and, (c) the non star-forming gas ($Z_{\rm NSF}$) as a function of $d_{\rm per}$. Plots (b) and (d) show MAD for $Z_{\rm SF}$ and $Z_{\rm NSF}$ respectively. The $Z_{\rm SF}$ within $d_{\rm per} \lesssim 1$ Mpc is elevated relative to gas further away. The $Z_{\rm NSF}$, on the other hand increases smoothly with decreasing $d_{\rm per}$, indicating accretion of non-star-forming gas on the filament galaxies.

In order to test our hypothesis and test if the increase in star formation activity near the spine of the filaments is correlated with an increase in the availability of gas, we study the distribution of mass in stars and gas in the filaments as a function of $d_{\rm per}$. In Figure 4.7(c)–(f) we show the variation in the fraction of stellar mass and gas mass as a function of $d_{\rm per}$ for $\sim 96\%$ of the galaxies in our sample with non-zero

gas mass fraction, and the respective MAD for the same. The denominator for the fractions, $M_{\rm tot}$ is the total mass of the galaxy, which includes the gas ($M_{\rm gas}$), stars (M_*) and the dark matter mass (M_{dm}) inside a 30 pkpc aperture.

The median stellar mass fraction (SMF) shows a mild increase only within $\lesssim 0.5$ Mpc from the central axis of the filaments. This trend is reciprocated by the gas mass fraction (GMF) as well. However, at $d_{\rm per} > 0.5$ Mpc, the median GMF rises smoothly, but the median SMF remains constant. The observed trends are also confirmed statistically in Table 4.3.

Furthermore, we note that all the trends seen in Figure 4.7 are primarily driven by low mass ($10^9 \leq M/M_\odot \leq 10^{10}$) which dominate our sample. Galaxies with stellar masses in the range $10^{10} - 10^{10.5}$ also show trends similar to their less massive counterparts with minor deviations. But the most massive galaxies show an almost constant distribution for sSFR and the gas mass fraction, but an incline in the stellar mass fraction distribution with decreasing $d_{\rm per}$ at small distances ($d_{\rm per} \lesssim 0.5$ Mpc) from the spine of the filament.

These trends suggest that the intrafilamentary gas condenses into the galaxies on filaments and fuel star formation, supporting the results of Liao & Gao (2019). However, these small changes (2%–5%) in the GMF and the sSFR are not enough to turn a passively evolving galaxy to an active one as seen here in Figure 4.5, and in other studies based on observations (Bonjean et al., 2019). Also because of the small magnitude of these changes it is not surprising that such trends have yet not been observed in real data. The increase in the passive fraction of galaxies is likely caused by increased gravitational interactions amongst filament galaxies, likely due to an increased number density of galaxies closer to the spine of the filament. As a result of these interactions, these galaxies not only exhaust their reservoir of gas, but will also show momentary increase in their star formation activity, therefore contributing to the trend observed for the sSFR. Similar conclusions have also been drawn by Bonjean et al. (2019), who modelled the passive fraction of filament galaxies to find a positive gradient in their SFR which they attributed to mergers.

Metallicity

Metallicity, the fraction of mass in elements heavier than Helium is dependent on the complex interplay of gas accretion on galaxies and outflows from different feedback processes. For our analysis of metallicity, we use the smoothed metallicity provided for each subhalo by Wiersma et al. (2009b). The gas metallicity is divided into the star-forming ($Z_{\rm SF}$) and non-star-forming ($Z_{\rm NSF}$) metallicity, respectively. The star-forming gas is cold ($\sim 10^4 K$) enough to form stars, with the SFR dependent upon the metallicity (Schaye & Dalla Vecchia, 2008). On the other hand, the non-star forming gas comprises hot and under-dense gas which can not form stars. We refer the reader to Schaye (2004) for a detailed discussion on how star-formation is implemented in the EAGLE simulation.

Our prior results indicate that galaxies are likely to accrete gas as they move towards the spine of the filament. Therefore, in order to test this hypothesis using Z we show the running median of $Z_{\rm SF}$ as a function of their perpendicular distance from the spine of the filaments, $d_{\rm per}$ in Figure 4.8. Although with significant scatter, the median $Z_{\rm SF}$ within $\lesssim 2$ Mpc of the spine of the filaments is clearly elevated relative to the galaxies further away. On the other hand, $Z_{\rm NSF}$ is found to increase

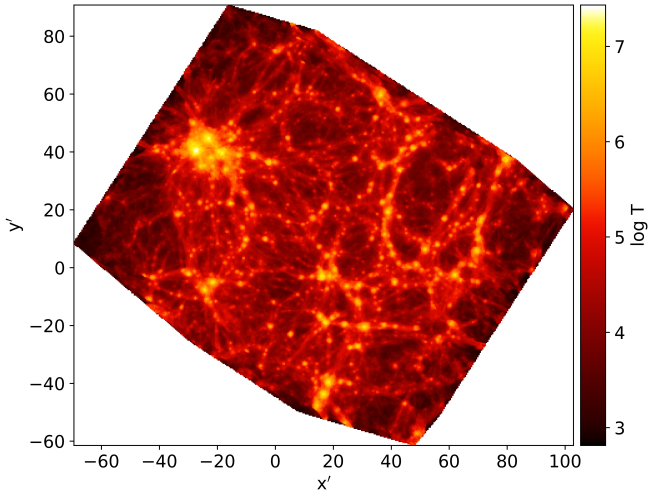

Figure 4.9: Projected temperature for the sample slice plotted in Figure 4.3. This plot makes use of the particle dataset at $z = 0.1$. The colours represent the mean of $log\ T$. The filaments clearly show concentration of gas at $10^4 < T(K) < 10^5$. This gas can be accreted by the filament galaxies.

smoothly with decreasing distance from the filament axis[2] (Figure 4.8(c)). This result, together with Figure 4.7(c) indicates that the non-star forming gas is accreted onto the galaxies. This result also supports the findings of Liao & Gao (2019) who used hydrodynamical simulations to show that at high redshifts ($z = 4.0$ and 2.5) around 30% of the gas accreted on the galaxy halos on filaments is the intrafilamentary medium.

4.4 Discussion

We have used data products from the EAGLE simulations to show that the intermediate density environment prevalent on the filaments influence the properties of galaxies on them. In the following, we discuss our results in the context of the filament galaxies studied in the literature, and also analyse the properties of filament galaxies relative to their counterparts in other environments.

4.4.1 Filaments in the literature

Kleiner et al. (2017) used the 6 degrees Field Galaxy Survey (Jones et al., 2009) and the Parkes all-sky survey (Staveley-Smith et al., 2000) to study the HI fraction of galaxies on nearby filaments identified by DISPERSE. They found that the galaxies ($M_*/M_\odot \geq 10^{11}$) closer (< 0.7 Mpc) to the spine of the filaments have higher HI-to-stellar mass ratio (HI fraction), where as the HI fraction among lower mass galaxies show no difference with respect to the control sample of galaxies > 5 Mpc away from

[2]Just like Fig. 4.7, these trends in metallicity are also driven by the low-mass galaxies ($10^9 \leq M/M_\odot \leq 10^{10.5}$). The more massive galaxies show noisy, almost constant distribution of both Z_{SF} and Z_{NSF} except an apparent decline within $d_{\rm per} \lesssim 1$.

the spine of the filaments. Kleiner et al. (2017) attributed the higher HI fraction in massive filament galaxies to cold gas accretion from the intrafilamentary medium.

On the other hand, Crone Odekon et al. (2018) used data from the ALFALFA survey (Giovanelli et al., 2005) to study the HI reservoir in galaxies. Complimentary to the results presented here, Crone Odekon et al. (2018) observed that at fixed stellar mass and colour, galaxies show a deficiency in HI on approaching the filaments. Furthermore, they also observed that at fixed local density, the HI fraction of lower mass galaxies ($10^{8.5} < M_*/M_\odot < 10^{10.5}$) decreases on approaching the filaments.

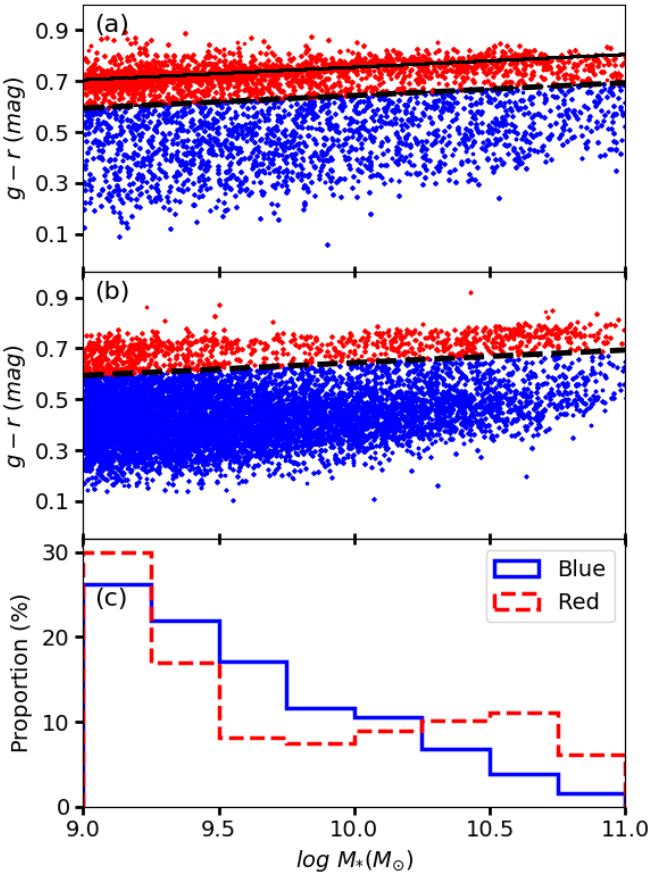

Figure 4.10: The (a) $g-r$ colour of galaxies in groups and clusters, and (b) filaments as a function of their stellar mass. The black line shows the red sequence fitted to the galaxies in clusters. In this work all galaxies bluer than 2σ from the red sequence are considered as blue, and the complimentary population is considered red. (c) This figure shows the kernel density estimates of stellar mass for the red and the blue populations on filaments. The Welch's t-test gives a p-value of $2.25e-175$, indicating that the two populations are statistically distinct. It is also evident that although majority of blue galaxies have masses $< 10^{10} M_\odot$, a significant fraction of red galaxies follow suit.

Even though the lower mass limit of our sample is 0.5 dex greater than the sample used by Crone Odekon et al. (2018), we can make use of the particle dataset to study the trends observed in the EAGLE simulation. In Figure 4.7 we show that the gas mass fraction decreases with $d_{\rm per}$ until 0.5 Mpc from the spine of the filament, but at $d_{\rm per} \lesssim 0.5$ Mpc, the trend seems to reverse. It is worth noting that the stellar mass of

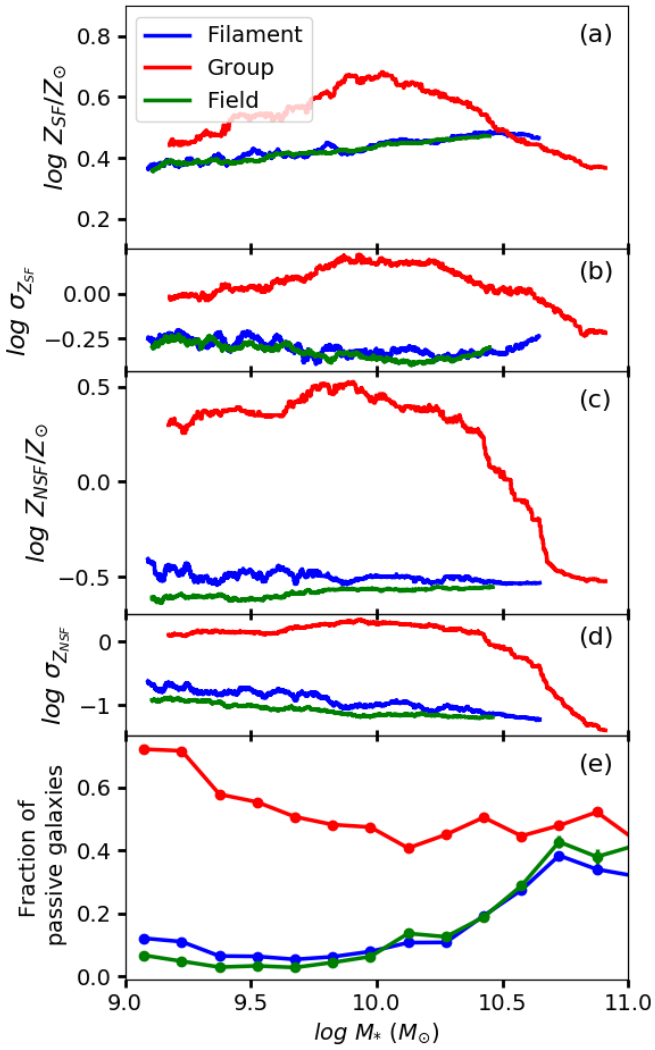

Figure 4.11: The (a) median metallicity of star forming gas ($Z_{\rm SF}$) and (c) non star-forming gas ($Z_{\rm NSF}$)as a function of stellar mass (M_*) of galaxies in groups and clusters (*red*), filaments (*blue*) and field (*green*), respectively. MAD for $Z_{\rm SF}$ and $Z_{\rm NSF}$ is shown in (b) and (d) respectively. (e) The fraction of passive galaxies as a function of M_* in the three environments. In groups the fraction of passive galaxies increases with decreasing M_* for galaxies with $M_* < 10^{10} M_\odot$. While an opposite trend is observed for the filaments and field.

galaxies also seems to increase within the same radius around the spine of filaments. These results, together with enhanced sSFR within 0.5 Mpc from the spine from the filament (Figure 4.7 (a)), indicate that the enhanced gas condensing in galaxies closer to the spine of the filaments may lead to an increase in the rate of formation of stars. This hypothesis is in tune with the results of Kleiner et al. (2017) as well as Figure 4.9, where we have used the particle dataset from the EAGLE simulation to show the projected temperature map for the gas in the same example slice shown in Figure 4.3. It is evident that the filaments in the EAGLE simulation comprise gas at $10^4 < T(K) < 10^5$, which can fuel star formation in the galaxies, especially closer to the spine of the filaments (Bonjean et al., 2019).

Darvish et al. (2015) studied 28 galaxies on filaments against 30 galaxies in field from the COSMOS survey ($z \sim 0.53$; Scoville et al., 2007). They found that the star-forming galaxies on filaments have higher metallicity than their counterparts in the field. Darvish et al. (2015) attributed this difference to the accretion of pre-enriched filamentary gas on to the filament galaxies. In a complimentary study of filaments at $z = 1.5$ from the Horizon hydrodynamical simulation, Gay et al. (2010) also found that the gas-phase metallicity of galaxies increases with decreasing distance from the spine of the filaments. Our analysis shows similar trends in Figure 4.8. However, we also note that the EAGLE simulations' reference model used here (RefL0100N1504) is known to over-predict the metallicity relative to runs with smaller box lengths and observations (figure 1; De Rossi et al., 2017b). But since this over-prediction is consistent throughout the box, it should not influence the trends observed in the metallicity as a function of environment.

Kuutma et al. (2017) used the SDSS data to study the statistical variation in the properties of galaxies on approaching the spine of the filaments. Kuutma et al. (2017) found that the galaxies become more elliptical and redder in the $g-i$ colour with decreasing distance from the spine of the filaments. Using a similar dataset, SM18 studied the Coma supercluster to find a similar increase in the $g-r$ colour index of galaxies with decreasing $d_{\rm per}$. A similar trend is reflected in the analysis presented here in Figure 4.5. We find that the median $g-r$ colour of galaxies becomes redder with decreasing distance from the spine of filaments.

Alpaslan et al. (2016b) analysed 1799 star-forming spiral galaxies ($z \leq 0.09$) within 3.79 h^{-1} Mpc of the centre of filaments using data from the Galaxy and Mass Assembly (GAMA) survey. In agreement with the results presented in this work as well as other literature (e.g. Kraljic et al., 2018; Laigle et al., 2018b), they found that galaxies closer to the spine of the filaments are more massive, and at fixed M_*, galaxies are quenched closer to the spine of the filaments. Based on our own results and those presented in the literature we therefore suggest that along with stellar mass and large-scale environment, anisotropic tides along filaments impact the assembly history of galaxy halos, and hence the properties of galaxies.

4.4.2 Filaments vs groups and field

In this section, we compare the properties of galaxies on filaments to their counterparts in groups and clusters, and the field.

In Figure 4.10 we show the distribution of galaxies in the colour-M_* plane for the groups and filaments, respectively. In order to compare the two colour distributions, we fit the red sequence to the distribution of cluster galaxies. In this work, all galaxies with $g-r$ colour more than 2σ bluer than the red sequence are classified as blue galaxies, where σ is the standard deviation (0.055 mag) obtained by iteratively fitting the red sequence. It is evident from Figure 4.10 (b) that there are fewer red galaxies on filaments, relative to the clusters. Specifically, while $\sim 54\%$ of the cluster galaxies are red, only 13% of the filament galaxies follow suit.

In Figure 4.10(c) we plot the kernel density estimates (KDE) of stellar mass for galaxies in both the colour selected populations of filament galaxies. KDE are closely related to histograms but are continuous and smooth. KDE is a non-parametric methods for calculating probability distribution of a variable using a non-negative function called kernel. We used Gaussian kernel and scott estimator (Scott, 2015)

for bandwidth used in the kernel. A large fraction of the blue galaxies (77%) are found to have stellar mass, $M_*/M_\odot \leq 10^{10}$. On the other hand, while most of the red galaxies on filaments are massive, around 63% of them have $M_*/M_\odot \leq 10^{10}$. The Welch's t-test applied to the two distribution yields a p-value of $2.25e-175$, inferring that the two populations are statistically distinct. This result indicates that some environmental mechanisms may be responsible for quenching star formation, or removing gas from the low-mass galaxies as well on the filaments.

The metallicity of a galaxy is related to its stellar mass M_*, such that more massive galaxies also have higher gas as well as stellar metallicities (McClure & van den Bergh, 1968; Lequeux et al., 1979; Garnett, 2002; Tremonti et al., 2004; Lee et al., 2006; Mannucci et al., 2010; Cresci et al., 2019). In Figure 4.11(a and c) we show the median metallicity of the star-forming gas ($Z_{\rm SF}$), and the non-star forming (NSF) gas ($Z_{\rm NSF}$) as a function of M_* in different environments. In agreement with the previous findings (De Rossi et al., 2017b), the NSF gas is found to be less metal rich relative to the star-forming gas. While the galaxies on filaments and field show almost constant $Z_{\rm SF}$ and $Z_{\rm NSF}$, their counterparts in groups show marginally different trends on either side of $M_*/M_\odot \sim 10^{10}$, such that the Welch t-test probability is 0.045 in favour of the hypothesis that the distribution of $Z_{\rm SF}$ for the lower mass galaxies ($M_*/M_\odot \lesssim 10^{10}$) is statistically similar to their massive counterparts. The respective probability for $Z_{\rm NSF}$ for group galaxies is found to be $\ll 0$. Such trends of lower Z in the most massive galaxies have also been observed in the Coma cluster (Poggianti et al., 2001), and the Coma supercluster (Tiwari et al., 2020).

Figure 4.11 can be compared to figure 1 of De Rossi et al. (2017b), who have also made use of the EAGLE simulation to compare the mass-metallicity relation obtained in simulations with various observational datasets and found them to agree within uncertainties. Our analysis indicates that the slope of the mass-metallicity relation is primarily determined by the galaxies in dense environments.

In Figure 4.11(c) we show the fraction of passive galaxies ($sSFR < 0.01$ Gyr^{-1}) as a function of stellar mass in different environments. It is evident that in the groups' environment, the fraction of low-mass ($M_*/M_\odot < 10^{10}$) passive galaxies increases significantly with decreasing M_*. On the other hand, the galaxies in filaments and field show identical trends in the opposite direction, i.e. the fraction of passive galaxies increases with M_*, particularly for galaxies with $M_*/M_\odot > 10^{10}$. This result is in broad agreement with the literature (e.g. Haines et al., 2006) where the dwarf galaxies are found to be passive only if they are a satellite to a massive galaxy. SM18 had also shown that the $NUV - r$ colour distribution of galaxies changes from field to clusters, mainly because of a higher fraction of massive galaxies turning redder in dense environments.

The morphology of galaxies can provide important clues to their evolution. In this work, we use the morphology of resolved galaxies having more than 300 stellar particles as per the procedure described by Thob et al. (2019). The shape parameters are derived using the reduced iterative inertia tensor in ellipsoidal apertures. Ellipticity is defined as:

$$e = 1 - \frac{c}{a} \tag{4.4}$$

where, c and a are the length of semi-minor and semi-major axis, respectively. In Figure 4.12 we plot the distribution of e for galaxies in different environments. The Welch's t-test for all but one pairs of environments yield p-value of ~ 0. The distri-

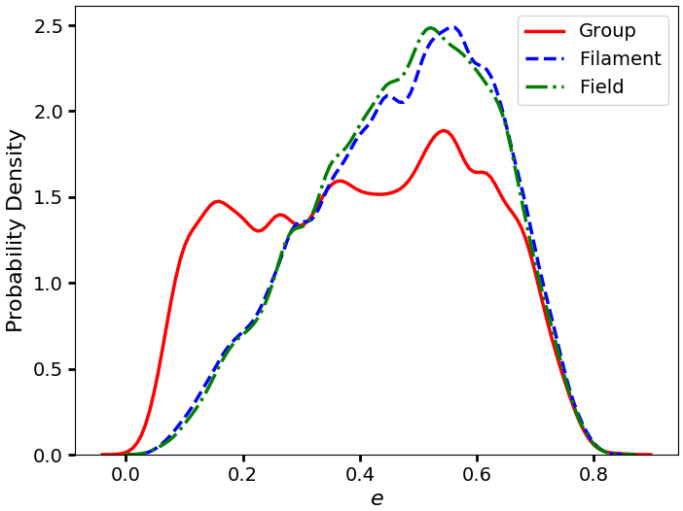

Figure 4.12: Distribution of ellipticity (e) of galaxies in the red population in different environments. Galaxies in clusters show a wider range of ellipticities relative to their counterparts in filaments and field. The Welch's t-test for the distribution of e of galaxies in all but one pair of populations is ~ 0. A p-value of 0.116 for the galaxies in field and filaments indicate that the morphology of these two populations is statistically identical.

bution of e for the filament and field galaxies has the Welch's t-test probability of 0.116 in favour of the hypothesis that the two distributions are identical, suggesting that the ellipticity of the field and filament galaxies are statistically indistinguishable. This result is in agreement with the observations (Alpaslan et al., 2015) where the GAMA survey data was used to show that the galaxies in filaments and field have similar distributions of ellipticity, such that the maximum of the distribution lies in the range $0.2-0.6$. On the other hand, the groups and clusters are dominated by low e, i.e. more elliptical galaxies.

4.5 Conclusion

We employ data from the EAGLE simulations to explore properties of galaxies in different environments, in particular, the large-scale filaments. We summarize the major findings of our analysis below:

- Galaxies become redder and more passive closer to the central axis of the filaments. Furthermore, this trend is likely observed due to an increase in the relative fraction of passively-evolving galaxies having $M_*/M_\odot \lesssim 10^{10}$ (Figures 4.6, 4.10(c)) closer to the centre of the filaments. In agreement with the results from various observations, this trend is observed within a radius of 2 Mpc around the spine of the filament, thus providing an upper limit for the filaments' radius.

- Both, the gas and stellar mass fractions of galaxies rise closer to the spine of the filaments within $d_{\rm per} < 0.5$ Mpc. But at $d_{\rm per} > 0.5$ Mpc the SMF remains constant while the GMF rises smoothly with increasing distance from the spine of the filaments. Together with the findings from the literature, these results

lead us to conclude that the observed trends are a consequence of increased gravitational interactions between filament galaxies closer to the spine of the filament. This enhancement in the interaction rate is caused by an increased number density of galaxies closer to the centre of the filaments.

- The morphology of galaxies on filaments is similar to their counterparts in field but statistically distinct from the ones in clusters. However, fewer red galaxies are found on the filaments relative to clusters.

To conclude, our results indicate that many properties of galaxies on filaments are different from their counterparts in clusters and field. The colour, star formation, metallicity and gas fraction of filament galaxies change as a function of their distance from the central axis of the filament. This could be an impact of the IFM as well as the number density of galaxies, both of which increase with decreasing $d_{\rm per}$. High resolution spectroscopic and HI data for galaxies covering all environments and a range of stellar masses are required to confirm our results. We hope the upcoming facilities such as the Vera Rubin Observatory (VRO) would be crucial for the same. At shorter wavelengths, the Advanced Telescope for High ENergy Astrophysics (ATHENA) x-ray observatory is likely to unravel the properties of the warm-hot intergalactic medium (WHIM) in the 0.5–12 kev range.

Chapter 5

Effects of galaxy interaction using merger simulation

5.1 Galaxy mergers

Galactic interactions in the form of collisions or flybys, structurally transform and accelerate the evolutionary processes in galaxies. The evolution of interstellar gas and star formation rate in such cases are dictated by kinematics of the interactions. Interactions provide departure from the secular evolution of galaxies and therefore, new ways of understanding the physical processes happening inside them. Mergers are stated to be main mechanism for formation of intermediate-mass ellipticals (e.g., Naab & Burkert, 2003; Bournaud et al., 2005; Cox et al., 2006; Yıldırım et al., 2017).

The collision of two galaxies involves a tremendous amount of energy. For example, two objects with masses $\sim 10^{12}$ $M_\odot$ interacting with relative velocities of ~ 300 km s^{-1}, so the collision energy is of order 10^{53} J. This energy is equivalent to about 10^{8-9} supernovae. Due to encounter velocity being about 0.1 % of the speed of light, this cannot be classified as a high energy phenomenon. But the energy released is comparable to the binding energies of the galaxies; therefore, the interaction has important evolutionary effects. The interaction typically has timescales of $\sim 10^2$ Myr.

Toomre & Toomre (1972) performed a collisionless (star-like) particle simulations. They noticed that features like tails were observed for close collisional encounters. They concluded that large-scale tidal distortions are formed as a result of decay in orbital energy, and two galaxies will eventually merge. They speculated that since the interaction timescale is very small compared to the age of the Universe, we observe only a fraction of merging galaxies. The mean distance between the galaxies in the Universe is much greater than their sizes; therefore, most collisions happen in gravitationally bound groups. Their simulations indicated that even a close encounter would result in a sudden increase of fuel in central regions due to flow of gas either from its own outer disc or via accretion from its partner. This increase in star formation was later observed by Larson & Tinsley (1978) by studying merging galaxies. They concluded that the colours of merging galaxies indicated a sudden burst of star formation as short as 20 Myr with 5% of the mass involved in it.

The merger of two galaxies inside dark matter halos not on a radial path is dictated by various physical processes. For a massive body moving inside an infinite,

homogeneous collection of low-mass objects, the gravitational interaction results in a dissipative force that resists its motion. The massive object as it moves through the cloud of low-mass objects pulls them towards itself, forming an overdense region. The gravitational pull from this overdense region decelerates the massive object. This drag force is known as *dynamical friction* (Chandrasekhar, 1943; Tremaine & Weinberg, 1984; Weinberg, 1986, 1989).

Mergers of galaxies of comparable masses are called *major mergers* and for galaxies with one galaxy much more massive than the other, like in the case of a spiral and dwarf galaxy, the mergers are called *minor mergers*. This work focuses on merger between a massive central galaxy ($M \sim 10^{12}$ M$_\odot$) and a dwarf galaxy ($M \sim 10^{9}$ M$_\odot$), therefore, we concern ourself with minor mergers.

For a merger to be classified as a *minor merger* the ratio of masses of the satellite (companion) to the central galaxy has to be less than or equal to 0.1. For a minor merger to have a significant impact on the central galaxy, the mass ratio should be more than 0.01. The observational signatures of minor mergers are much weaker than those of major mergers, so observational comparisons are harder. Moreover, there are technical difficulties in the simulations, especially in adequately resolving a companion that is much smaller than the primary. Galaxies have a wide range of masses; therefore, the probability of same mass galaxies colliding with each other is less.

Most of the present-day galaxies have encountered minor mergers in the past, and these mergers play crucial roles in defining their properties as seen today. Hernquist & Mihos (1995) showed that minor mergers are more frequent than the major mergers. Holmberg (1969) showed that the satellite galaxies are preferentially located along the minor axis of the central galaxies, an effect later called as *Holmberg effect*.

Minor mergers are less destructive than the major mergers. In some cases, it may simply increase the mass of the disc without destroying it (Quinn et al., 1993). Minor mergers are responsible for heating of the stellar disc (Hopkins et al., 2008) which may result in a so-called *thick disc* (Villalobos & Helmi, 2008, 2009; Villalobos et al., 2010; Di Matteo et al., 2011). These mergers lead to the formation of internal waves, extended spiral arms, inner stellar disc and rings. Some of the mergers may also result in the formation of spheroids. Bournaud & Combes (2004) showed that many successive minor mergers form elliptical galaxies more efficiently than a single major merger.

In this work, we run a set of minor merger simulations of mass ratio 0.08 to study the effects on the dwarf galaxy after one pericentric passage. We vary the properties related to the trajectory, compactness and initial gas mass content in the dwarf galaxy. In section 5.2, we discuss the numerical setup used in this work. In sections 5.3 and 5.4 we discuss the properties of central and dwarf galaxies. We discuss the simulation setup in section 5.5 followed by results in section 5.6.

5.2 Numerical setup

The method consists of two parts, first simulating the central and dwarf galaxies in isolation and second, to simulate a merger. In the following sections, we describe these simulations. We use Adaptive Mesh Refinement (AMR) code `RAMSES` (Teyssier, 2002b) for these simulations.

5.2.1 RAMSES code

In what follows we will be describing basic details of method and implementation concerning an Eulerian code RAMSES (Teyssier, 2002a).

RAMSES is a massively parallel Adaptive Mesh Refinement hydrodynamical code, written in Fortran90 for self-gravitating plasma flows. Many numerical ingredients for physical processes such as star formation, intergalactic background UV heating, interstellar medium cooling function, and various recipes for feedback have been implemented in it.

In simulations performed with RAMSES :

- Dark matter and stars are treated as massive particles and modelled as gravitationally interacting particles. Gravitational force is softened to inhibit collisional relaxation.
- The gas is described by a density/energy/velocity/pressure field discretised on a grid which is adaptively refined.

We have already discussed general aspects of hydrodynamics for an Eulerian code in section 1.7.2. RAMSES uses MUSCL scheme with moncen or minmod slope limiter. This has proven effective in capturing shocks. This is a higher-order Godunov scheme which combined with sharp Riemann solver and adaptive mesh refinement (AMR) works well to capture discontinuities within a few grid cells (Teyssier, 2002a; Fromang et al., 2006; Ziegler, 2005; Agertz et al., 2007). There are, a variety of options available for Riemann solvers in RAMSES : LLF (local-Lax-Friedrichs), HLL (HartenLaxvon Leer), Lax-Friedrich and HLLC (HLL Contact) solver.

In this work, we use MUSCL-HANCOCK scheme as Godunov flux integrator, LLF Riemann solver and MinMod slope limiter for the reconstruction of state vector on the grid.

Adaptive mesh refinement (AMR)

As gravitational collapse forms structures like filaments, galaxies, GMC and stars, density contrast varies by many orders of magnitude. Since computational resources are limited, one wants a coarse grid in the regions of small density contrast (information poor regions) and fine grid regions of high contrast. To achieve this, RAMSES uses the adaptive mesh refinement with refinement criterion based on physical parameters.

Codes in computational astrophysics use two kinds of Adaptive mesh refinement (Berger & Oliger, 1984). First is called *patch based approach* which consists of rectangular grids of different sizes nested together. Codes like ENZO (O'Shea et al., 2004) and FLASH (Fryxell et al., 2000) use this approach. Second is a *tree based approach* (Barnes & Hut, 1986; Khokhlov, 1998) in which a parent grid cell is refined into daughter cells on a cell-by-cell basis. Codes like ART (Kravtsov et al., 1997) and RAMSES use this approach.

In patch-based approach, data structures are less complex as code has to handle only a small number of grids which cover an area of interest. On the other hand, tree based approach requires tree traversal, making it hard to optimise cache and memory access. However, tree-based codes are able to follow the hydrodynamical flow better and thus; their computational cost is much more optimised when compared to patch based codes.

RAMSES uses octree AMR structure in which each cell is refined into two cells along each dimension. Therefore, in 3-dimensions, one has eight daughter cells, and in 2-dimensions, one has four daughter cells. As RAMSES is massively parallelised using Message Passing Interface (MPI) library, each processor works only on a sub-volume (domain). To get domains, there are various methods which are available to the user. Most commonly used method is based on Peano-Hilbert space-filling curve (Peano, 1890; Hilbert, 1891).

Adaptative time-stepping

In any Eulerian code, in order to ensure convergence of implemented numerical schemes while solving the advection of the fluid flow on a grid with cell size of Δx and the flow velocity v, CFL condition (Courant et al., 1967) must be satisfied:

$$\frac{v\Delta t}{\Delta x} < C \gg 1 \tag{5.1}$$

Since RAMSES uses oct tree structure $\Delta x^{l+1} = \Delta x^l/2$, CFL condition leads to $\Delta t^{l+1} = \Delta t^l/2$. This means both space and timesteps are adaptive. As one can see that finer grids have smaller time steps, therefore, incrementing all the grids at every time step is computationally inefficient. RAMSES uses *level subcycling* in which the grids of each AMR level update according to their own timestep and whole AMR grid is update only when needed. Every coarse level is synchronised with the fine level at every other two fine time steps.

The criterion which decides if a cell should be refined into daughter cells is called the *refinement criterion*. This can be based on the total mass of particles in the cell, geometry, local jeans length and gradient of the field. We use a box size of 300 kpc filled with a coarse grid of 8 levels with $(2^8)^3$ cells. We allow an additional five levels of refinements giving a spacial resolution of $\sim$ 36 pc.

Particle dynamics and self-gravity in RAMSES

The stars and Cold dark matter in RAMSES are modeled as collisionless massive particles. Thus they only interact by gravitation. In order to compute their dynamical evolution one needs to solve the *Poisson equation*:

$$\begin{aligned} \text{Poisson equation: } & \Delta\Phi = 4\pi G\left(\rho_{\text{gas}} + \rho_{\text{ particles }}\right) \\ \text{Gravitational force: } & \dot{\mathbf{v}} = -\nabla\Phi \end{aligned} \tag{5.2}$$

In order to calculate the gravitational potential field Φ one needs to project particle masses onto the grid. RAMSES implements the most commonly used kernel for this called the cloud-in-cell (CIC) kernel (Hockney & Eastwood, 1981). Once the density field is computed, it is added to the gas density field, and RAMSES can determine Φ on an optimised multigrid solver (Guillet & Teyssier, 2011).

Gravitational force from gravitational potential using $\mathbf{g}^n = -\nabla\Phi^n$ at a given time t^n is computed on the grid by differentiating the gravitational potential Φ using 5-point finite difference scheme. This potential is computed at particle position $\mathbf{X}_p^n$ using the CIC kernel. Velocity and positions are updated using second order

predictor-corrector method (Teyssier, 2002a):

$$\mathbf{v}_p^{n+1/2} = \mathbf{v}_p^n - \nabla\Phi^n \Delta t^n/2 \tag{5.3a}$$
$$\mathbf{x}_p^{n+1} = \mathbf{x}_p^n + \mathbf{v}_p^{n+1/2}\Delta t^n \tag{5.3b}$$
$$\mathbf{v}_p^{n+1} = \mathbf{v}_p^{n+1/2} - \nabla\Phi^{n+1}(X_p^n)\Delta t^n/2 \tag{5.3c}$$

Star formation

We discussed in section 1.4.2 that perturbations in molecular clouds collapse to form stars. If a pressureless fluid collapses under gravity the time-scale of collapse is called the *free-fall time* given by:

$$\rho^{-1/2} \propto t_{\rm ff} = \sqrt{\frac{3\pi}{32G\rho}} \qquad \text{(3D homogeneous sphere)} \tag{5.4a}$$
$$= \sqrt{\frac{\pi}{G\rho}} \qquad \text{(infinite 1D cosine perturbation)} \tag{5.4b}$$

Since the physical scale of star formation is very small it is not possible to resolve it even in galactic scale simulations, `RAMSES` like most of other codes, implements a subgrid recipe for star formation. The s_m term in equation 1.110a is written as:

$$\frac{\partial\rho}{\partial t} + \vec{\nabla}\cdot(\rho\vec{v}) = s_m = -\frac{{\rm d}\rho_*}{{\rm d}t} \tag{5.5}$$

Therefore, in some cells where density is high enough, gas reservoir is depleted and corresponding mass is converted into a star particle. Local star formation rate is given by:

$$\frac{{\rm d}\rho_*}{{\rm d}t} = \frac{\rho}{t_*}\,(\rho \geq \rho_0) \tag{5.6a}$$
$$= 0\,(\rho < \rho_0) \tag{5.6b}$$

where t_* is the local star formation time-scale, ρ is local gas density and ρ_0 is star formation density threshold above which star formation is triggered. Star formation time scale t_* is assumed to be proportional to local free-fall time $t_{\rm ff}$:

$$t_* = \frac{t_{\rm ff}}{\epsilon} \tag{5.7}$$

where ϵ is called *star formation efficiency*.

We have chosen ρ_0 and ϵ equal to 1 H/cm^3 and 0.02 respectively. Stellar particles are created by stochastic model (Rasera et al., 2006). At a time step Δt, a stellar mass number n is sampled from a Poisson's distribution with mean (λ) as $\rho(\Delta x^3/m_*)(\Delta t/t_*)$. Here Δt is the simulation timestep, and m_* is set equal to the mass resolution of the simulation. A new particle with mass nm_*.

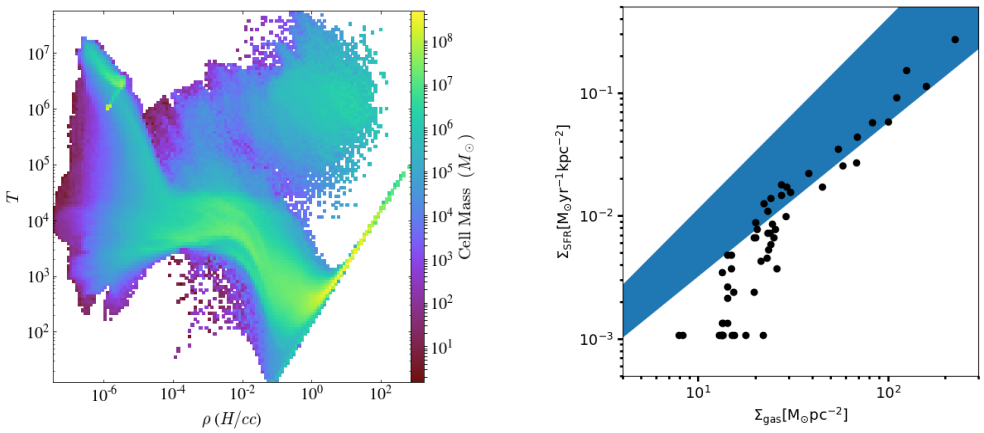

Figure 5.1: (left) Density versus temperature phase plot. (right) Kennicut-Schmidt (KS) relation for the central galaxy by taking star formation in < 50 Myr inside radius of 15 kpc. The shaded region shows the allowed range of values obtained from observations. We note that the simulation results are not inconsistent with the observed relation

Gas dynamics

Gas is modelled in RAMSES by solving the Euler's equation on adaptive grids. We use a method based on MUSCL to solve Euler's equation with a second-order unsplit Gundonov scheme. The Local Lax-Friedrichs (LLF) method was chosen as Riemann solver with MinMod slope limiter (Roe, 1986).

In order to prevent the numerical fragmentation of gas, simulation must be able to resolve Jeans length and Jeans mass (Truelove et al., 1997). To accomplish this, an artificial pressure is maintained along with thermal pressure of the gas. Pressure floor can be expressed in terms of an effective temperature $T_{\rm J} = T_0 n_{\rm H}/n_*$. Here n_* is the star formation threshold. We have set T_0 as 500 K. This pressure floor ensures that Jeans length is always resolved with ≥ 4 cells in the highest resolution.

Cooling and heating processes

The gas can cool using ionic and atomic processes and this radiative cooling is modeled in `RAMSES` by a cooling function Λ. The UV background due to quasars and massive young stars is modeled using the heating function given by Haardt & Madau (1996a). The source term s_e in section 1.110c is given by:

$$s_e = n_{\rm H}^2 \times (\mathcal{H} - \Lambda) \tag{5.8}$$

This is tabulated beforehand for a set of (ρ, Z, T) values. Using this table local cooling rate is interpolated for each AMR cell in simulation.

In this work, we allow the metal and atomic cooling of the gas. A uniform UV-background is used, which is turned on at a redshift of 8.5 (Haardt & Madau, 1996b). We have used self-shielding from the local UV of dense gas with density above 0.01 H/cc (Roškar et al., 2014).

Central galaxy	
M_{200} (10^{10} $M_\odot$)	102.4
V_{200} (km s^{-1})	210.1
$N_{\rm dm}$	10^6
$N_{\rm stars}$	2×10^6
$M_{\rm dm}$ (10^{10} $M_\odot$)	44.3
$M_{\rm stars}$ (10^{10} $M_\odot$)	6.29
$M_{\rm gas}$ (10^{10} $M_\odot$)	2.69
λ	0.04
stellar disc scalelength ($r_{\rm ds}$; kpc)	2.28
stellar disc radial cut ($r_{\rm cut,star}$; kpc)	11.13
gas disc scalelength ($r_{\rm dg}$; kpc)	3.71
gas disc radial cut ($r_{\rm cut,gas}$; kpc)	11.13
dark matter halo scalelength ($r_{\rm halo}$; kpc)	19.95
dark matter halo radial cut ($r_{\rm cut,halo}$; kpc)	49.88
Dwarf galaxy	
M_{200} (10^{10} $M_\odot$)	8.99
V_{200} (km s^{-1})	65.0
$N_{\rm dm}$	10^6
$N_{\rm stars}$	2×10^6
$M_{\rm dm}$ (10^{10} $M_\odot$)	6.21
$M_{\rm stars}$ (10^{10} $M_\odot$)	0.160
$M_{\rm gas}$ (10^{10} $M_\odot$)	0.160
$\lambda = 0.02$	
stellar disc scalelength ($r_{\rm ds}$; kpc)	0.75
stellar disc radial cut ($r_{\rm cut,star}$; kpc)	2.5
gas disc scalelength ($r_{\rm dg}$; kpc)	0.75
gas disc radial cut ($r_{\rm cut,gas}$; kpc)	2.5
$\lambda = 0.04$	
stellar disc scalelength ($r_{\rm ds}$; kpc)	1.5
stellar disc radial cut ($r_{\rm cut,star}$; kpc)	5.0
gas disc scalelength ($r_{\rm dg}$; kpc)	1.5
gas disc radial cut ($r_{\rm cut,gas}$; kpc)	5.0
$\lambda = 0.08$	
stellar disc scalelength ($r_{\rm ds}$; kpc)	3.0
stellar disc radial cut ($r_{\rm cut,star}$; kpc)	10.0
gas disc scalelength ($r_{\rm dg}$; kpc)	3.0
gas disc radial cut ($r_{\rm cut,gas}$; kpc)	10.0

Table 5.1: Parameters used in initial condition for central and dwarf galaxies.

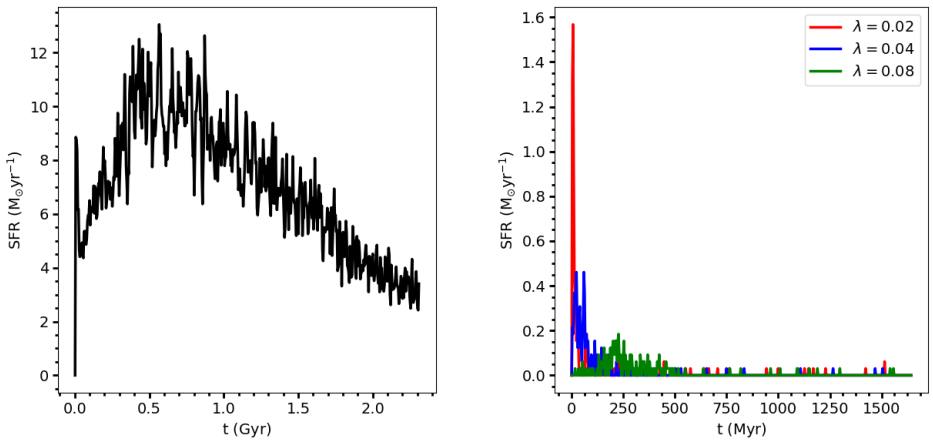

Figure 5.2: (left) Star formation rate in an isolated central galaxy. (right) Star formation rate in isolated dwarf galaxies with different compactness.

Stellar feedback with delayed cooling

Feedback plays a key role in preventing excessive star formation. In this work, we have used delayed cooling (Gerritsen, 1997; Thacker & Couchman, 2000; Stinson et al., 2006) as the feedback mechanism. The energy from a particle marked for a supernova is injected into the neighbouring cell and cooling for the gas inside the expected Sedov blast wave radius is 'turned off'. This allows the gas to be efficiently heated, preventing the star formation and provides acceleration to it for outflows.

The stellar environment is turbulent from the stellar winds and supernova filled with cosmic rays and magnetic field. Thermal energy dissipates almost instantaneously through cooling. Non-thermal processes take much longer to dissipate. We use the implementation given by Teyssier et al. (2013) for AMR codes. To mimic the specific energy density in non-thermal processes: turbulence, cosmic rays or magnetic field, a variable $\epsilon_{\rm turb}$ is introduced. In this type of feedback, known as *delayed cooling*, a specific energy tracer ($\epsilon_{\rm turb}$) is stored on the grid as a passive scalar which is associated with unresolved turbulent energy.

The time scale of decay of the non-thermal components ($t_{\rm diss}$) is much longer than the one associated with gas cooling. The evolution of this energy is given by:

$$\frac{D\epsilon_{\rm turb}}{Dt} = \frac{\dot{E}_{\rm inj}}{\rho} - \frac{\epsilon_{\rm turb}}{t_{\rm diss}} \tag{5.9}$$

where $\dot{E}_{\rm inj}$ is the non thermal energy source term. The second term is the dissipation term with timescale $t_{\rm diss}$.

The non-thermal energy injection is parametrized as:

$$\dot{E}_{\rm inj} = \dot{\rho}_* \eta_{\rm SN} 10^{50} \text{ erg/M}_\odot \tag{5.10}$$

which corresponds to injection of 10^{51} erg for every 10 $M_\odot$ star. $\eta_{\rm SN}$ is the fraction of stars going supernovae and is taken as 10 % (Teyssier et al., 2013).

The turbulent velocity dispersion is given by:

$$\sigma_{\rm turb} = \sqrt{2\epsilon_{\rm turb}} \tag{5.11}$$

The radiative cooling is turned off till the time $\sigma_{\rm turb}$ is above a minimum value $\sigma_{\rm min}$ which is kept fixed at $\sigma_{\rm turb} = 100$ km s^{-1}. This value corresponds to 0.1 % of injected specific energy of supernova.

In this feedback recipe, there are two main free parameters, $t_{\rm diss}$ and $\sigma_{\rm min}$. Both these parameters have similar effects on variation so one can be fixed and other is used as a parameter. $\sigma_{\rm min}$ is fixed at 100 km s^{-1}. There is only one parameter that is free in this implementation, i.e. $t_{\rm diss}$. We have taken the value of $t_{\rm diss}$ to be 2 Myr.

Delayed cooling is better than other feedback mechanisms like kinetic feedback because it is able to suppress cooling catastrophe and enhances the outflows. Though over-cooling in simulation is a numerical problem, shutting off radiative cooling amounts to meddling with the physical process which prevents the formation of stars. One can think of this strong supernova II feedback as a compensation for all other feedback processes neglected here that could have been important for galaxy evolution.

5.3 Central Galaxy

We use DICE (Perret, 2016) for creating initial conditions. For the central galaxy, we follow the setting of G1 galaxy from (Perret et al., 2014). We summarise some of the parameters used in initial conditions for the central galaxy in Table 5.1. We start with stellar and gas disc with exponential density profile embedded inside a dark matter halo. Figure 5.1(left) shows the phase diagram for the isolated run for the central galaxy. The gas in temperature range 10^4 K $< T < 10^6$ K and $10^{-4} < n_{\rm H} < 10^{-1}$ comes from inter-galactic medium (IGM). The gas with $T > 10^5$ K and $n_{\rm H} < 10^{-4}$ is hot diffused gas, produced from the feedback and residing in circumgalactic medium (CGM). It is clear that above the density of 0.1 H cm^{-3} the artificial pressure floor is operating, preventing numerical fragmentation.

Kennicutt (1998b) observed that the star formation rate surface density ($\Sigma_{\rm SFR}$) follows an Universal relation, now called Kennicutt-Schmidt (KS) relation, with gas surface density given by: $\Sigma_{\rm SFR} \propto \Sigma_{\rm gas}^{1.4}$. In the Figure 5.1(right) we plot star formation rate density ($\Sigma_{\rm SFR}$) against the gas surface density ($\Sigma_{\rm gas}$). The line represents the fit for observationally observed Kennicut-Schmidt relation. We observe that the simulation is able to produce a galaxy which can reproduce K-S relation reasonably well.

In Figure 5.2(left) we show the star formation rate in the central galaxy. At the start of the simulation, there is an initial star-burst followed by a gradual decrease in star formation. For a galaxy in isolation with the absence of new gas coming in the form of inflows, this increase and the gradual decrease is expected in case of delayed cooling feedback recipe (Rosdahl et al., 2017b).

5.4 Dwarf Galaxy

We simulate a dwarf galaxy in isolation for comparing it with the case of mergers with different parameters. Table 5.1 lists the parameters used for simulating dwarf galaxies. We simulate the dwarf galaxy with virial mass ($M_{\rm vir}$) 8.99×10^{10} M$_\odot$. The disc scale radius for gas in dwarf is varied from 0.75 kpc to 3.0 kpc for the spin parameter (λ) 0.02 to 0.08.

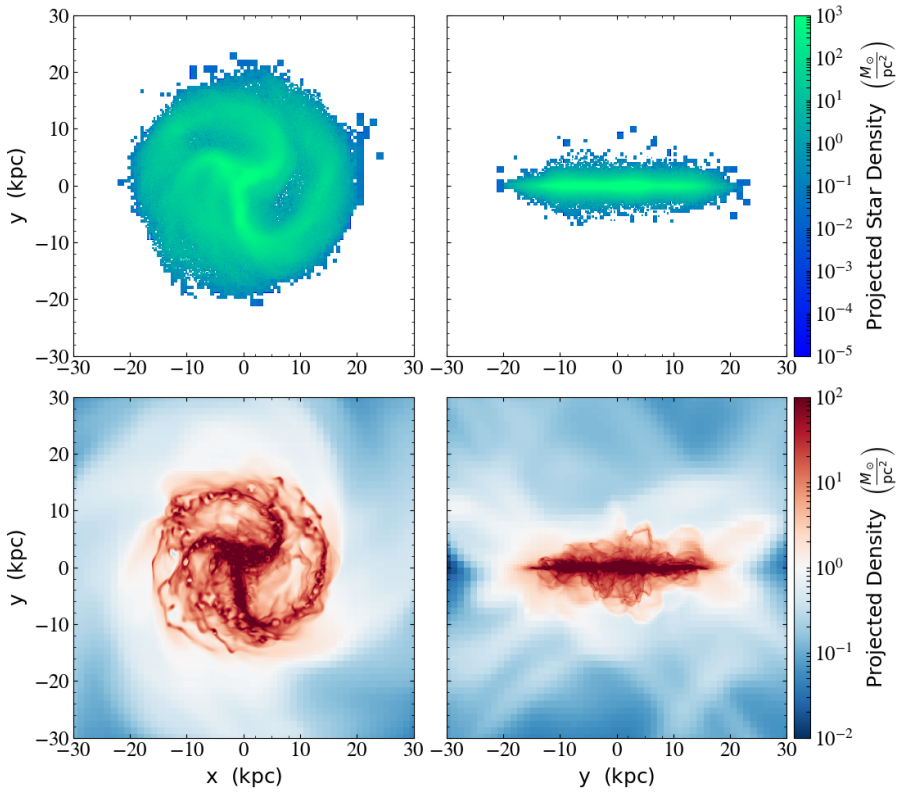

Figure 5.3: Plots for isolated central galaxy at 372 Myr: (top) projection plot for gas density in face-on (left) and edge-on (right) views.(bottom) projection plot for stellar mass density in face-on (left) and edge-on (right) views.

In Figure 5.4 we plot projected stellar mass (face-on view) and projected gas density (edge-on view) for isolated dwarf galaxies for different spin parameters. As the disc scale radius for a higher spin parameter ($\lambda = 0.08$) is larger, the stellar disc is bigger compared to the case of a low spin parameter ($\lambda = 0.02$). As there is weaker gravitational pull compared to the central galaxy, the galactic outflows in the case of dwarf galaxies is higher.

In Figure 5.2(right) we have shown the star formation rate for isolated dwarf galaxies with different spin parameters. For a smaller spin parameter ($\lambda = 0.02, 0.04$) since the disc is more concentrated, there is a strong initial stellar burst followed by decay, but in the case of a higher spin parameter ($\lambda = 0.08$) there is a smaller burst of star formation. Since in case of a higher spin parameter, the gas is more diffused in galactic disc the criterion for star formation is not satisfied easily, resulting in lower star formation rate.

5.5 Merger simulations

We perform a series of simulations varying different parameters related to the merger scenario. In Table 5.2 we list the values taken for different parameters related to the merger setup. We have performed following sets of merger simulations and studied the amount of gas that remains in the dwarf galaxy and the effect on the star formation.

- *Effects of pericentric distance*: Initially the galaxies are separated by 125 kpc.

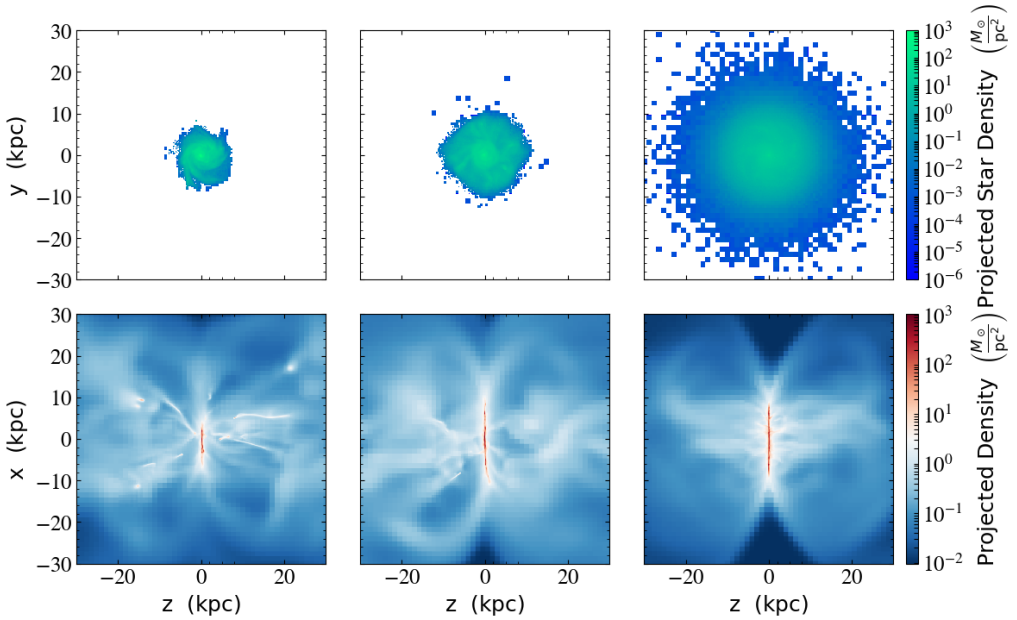

Figure 5.4: This plot shows isolated dwarf galaxy (plots at 300 Myr): different columns represent dwarf galaxies with different spin parameters. (top row) stellar projection mass projection viewed face-on. (bottom row) gas density projection plot viewed edge-on.

Parameter	Values
pericentric distance (kpc)	20, 40, 50
spin parameter (λ)	0.02, 0.04, 0.08
gas fraction in dwarf (%)	0.875, 1.75, 3.5

Table 5.2: Merger simulations initial conditions.

Table 5.3 shows the initial velocities given to the dwarf galaxy to achieve different pericentric distances corresponding to 20 kpc, 40 kpc and 80 kpc. The spin parameter for the dwarf galaxy is fixed at 0.04.

- *Effects of compactness*: For the trajectory having a pericentric distance of 40 kpc we vary the spin parameter (λ) to simulate galaxy with different compactness. We perform simulations with spin parameters 0.02, 0.04 and 0.08 for the dwarf galaxy.

- *Effects of gas mass*: For the trajectory having a pericentric distance of 40 kpc we vary the gas mass in the dwarf galaxy. We perform the merger simulations with gas mass in dwarf varying from 0.08×10^{10} $M_\odot$, 0.16×10^{10} $M_\odot$ and 0.32×10^{10} $M_\odot$.

We run a total of seven merger simulations and five isolated dwarf galaxy simulations to compare with merger simulations. For each merger simulation, we study the evolution of stellar mass and gas mass in the disc and compare the evolution with isolated galaxy with time.

Pericentric distance (d_{peri})	velocity (km/s)
20 kpc	[0, -42.3, 0]
40 kpc	[0, -69.2, 0]
80 kpc	[0, -103.3 , 0]

Table 5.3: Merger simulations parameters: the dwarf galaxy is placed at position $x = 125$ kpc, $y = 0.0$ kpc, $z = 0.0$ kpc and given different velocities in y-direction to achieve different pericentric distances.

5.6 Results

5.6.1 Effects of pericentric distance

In Figure 5.5(top) we show the projected stellar mass for different pericentric distances. In the cases of 80 kpc and 40 kpc pericentric distances, the stars at in the outer disc have been stripped from the disc forming tidal tails. In the case of 20 kpc pericentric distance, the disc shows a single tidal tail. In Figure 5.5(bottom) we show the projected gas density of the galaxies. There is a decreasing trend for the gas that remains in the disc with decreasing pericentric distance. We observe gas in the disc decreases considerably as the pericentric distance decreases.

In Figure 5.6 we show the cumulative stellar mass of the new stars formed in the dwarf galaxy for different trajectories. We observe a sharp increase in the stellar mass of the galaxies, which corresponds to initial star-burst. Near the pericenter of the trajectories, there is a gradual increase in the stellar mass. This second increase of stellar mass is more prominent for the trajectory with 20 kpc pericentric distance. The reason for this increase can be the compression of gas by tidal forces that leads to star formation.

In Figure 5.7 we show the gas with temperature $T < 10^4$ K inside the disc with radius 5 kpc and 2 kpc and height of 1 kpc. There is an initial loss of gas at both the radii because of initial star formation. In outer radius, the decrease in mass of the gas inside is more for the case of 20 kpc pericentric distance after passing from the pericenter. In all the cases we observe that gas within the inner radius remains nearly constant after crossing pericenter except in the case of 20 kpc pericentric distance where it decreases.

To explore how the merger affects the star formation activity in the dwarf galaxy we compare the evolution of hot gas ($T > 10^4$ K), cold gas ($T <= 10^4$ K) and stellar mass (M_*) compared to the isolated galaxy at different times.

The evolution of cold gas ($T <= 10^4$ K) mass inside the disc of height 1 kpc and radius of 2 kpc and 5 kpc is shown in Figure 5.8(b). Before the pericentric passage, in the cases of 80 kpc and 40 kpc pericentric distances, there is a relative increase in cold gas at the outer radius, which is absent in 20 kpc case. The inner disc is not affected significantly in any of the cases before the pericentric passage as we observe fluctuations in the ratio with respect to the isolated case. On nearing the pericenter, we observe a significant decrease in cold gas mass at both radii, which becomes larger as the pericentric distance decreases.

In Figure 5.8(a) we show the ratio of hot gas ($T > 10^4$ K) mass inside a sphere of radius 5 kpc as a function of time. In the case of 80 kpc pericentric distance, we observe that hot gas mass remains similar to the isolated galaxy evolution before the

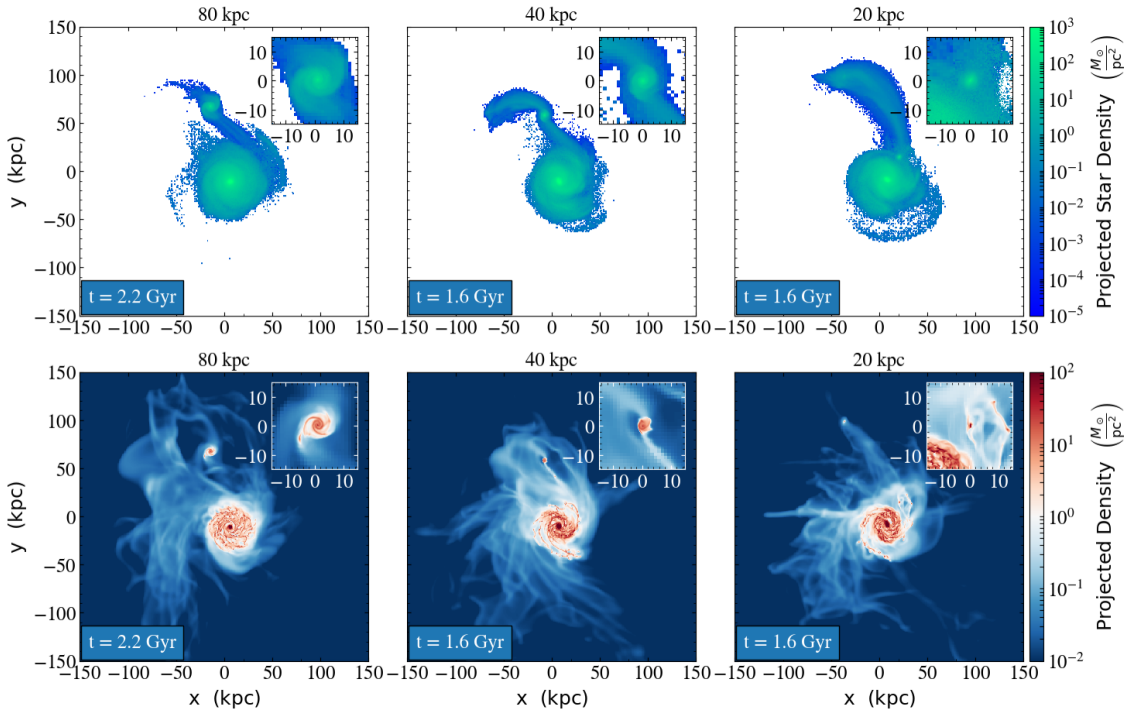

Figure 5.5: Effects of pericentric distance: (top) stellar mass projection plot and (bottom) gas density projection plot for different pericentric distances of 50 kpc, 40 kpc and 20 kpc in face-on view.

pericentric passage but increases 10 times when the galaxy is closer to the pericenter. For the cases of 40 kpc and 20 kpc pericentric distance, there is a sudden increase in the hot gas mass compared to isolated evolution and reaches a maximum of ~ 20 times near to the pericenter.

The stellar disc of the dwarf galaxy is expected to be disturbed as it passes near the pericenter of the trajectory. In Figure 5.8(c) we show the relative stellar mass evolution of the stellar disc with respect to isolated evolution inside a disc of height 1 kpc and outer radius of 2 kpc and 5 kpc. Before approaching the pericenter, for both the radii and different pericentric distance, we observe similar stellar mass evolution observed in the isolated case. On approaching the pericenter in cases of 80 kpc and 40 kpc there is no significant difference is observed in the inner disc. The stellar mass in outer disc for 40 kpc pericentric distance decreases by 25% on approaching the pericenter whereas no change is observed in 80 kpc case. For 20 kpc pericentric distance, we observe that both inner and outer discs are disturbed. The stellar mass decreases on approaching the pericenter in the inner and outer disc is 25% and 50% respectively.

To explore the trend of more gas accretion and star formation in the case of low pericentric distance in Figure 5.9 we show a temperature slice, and on top of it, we plot the streamlines, showing the family of curves tracing the tangent to the velocity vector of the gas element, for 20 kpc and 80 kpc pericentric distance. The plots show the time just after the pericentric passage where the galaxy is denoted by the green circle. It is observed that in case of low pericentric passage, the cold gas from the circumgalactic medium can reach the dwarf galaxy radially and therefore the star formation can fuel the star formation around the pericentric passage. In

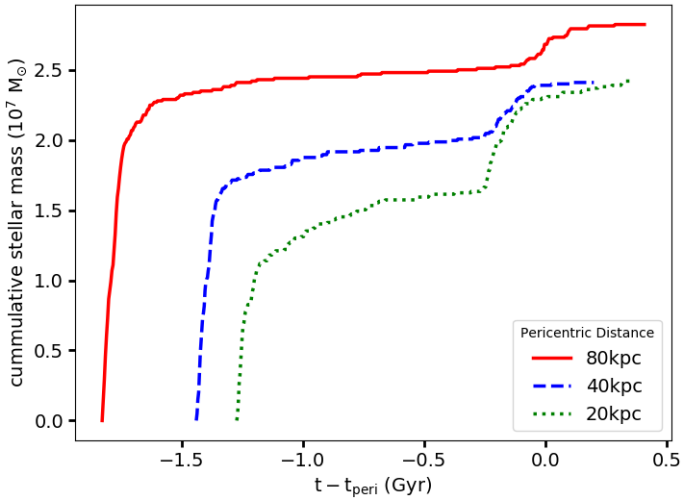

Figure 5.6: Effects of pericentric distance: cummulative stellar mass of dwarf galaxy for merger simulation with different pericentric distances. We observe a spike in stellar mass as galaxy approaches the pericenter. The spike in stellar mass increases with decrease in pericentric distance.

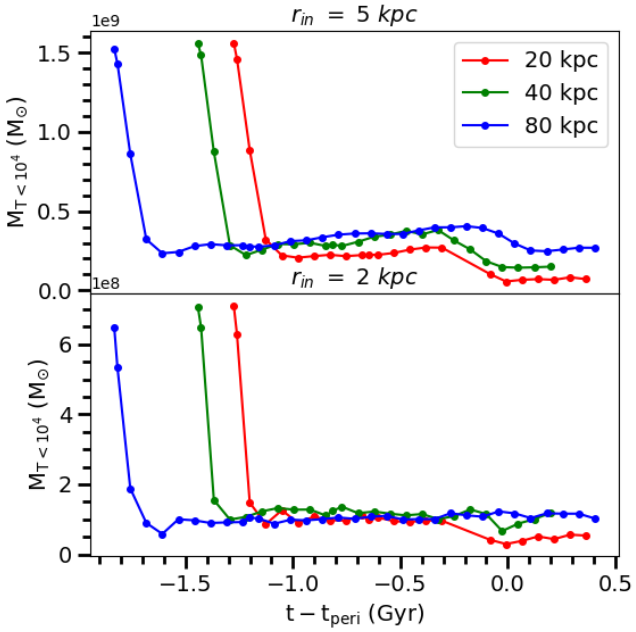

Figure 5.7: Effects of pericentric distance: mass of the gas with temperature $T < 10^4$ K in disc with thickness of 2 kpc and different radius $r_{\rm in}$ of 5 kpc (top panel) and 2 kpc (bottom panel). Gas retained by the dwarf galaxy decreases for decreasing pericentric distance. For a radius of 2 kpc the gas remains unaffected in the cases of 40 kpc and 80 kpc but shows a further decrease for 20 kpc case.

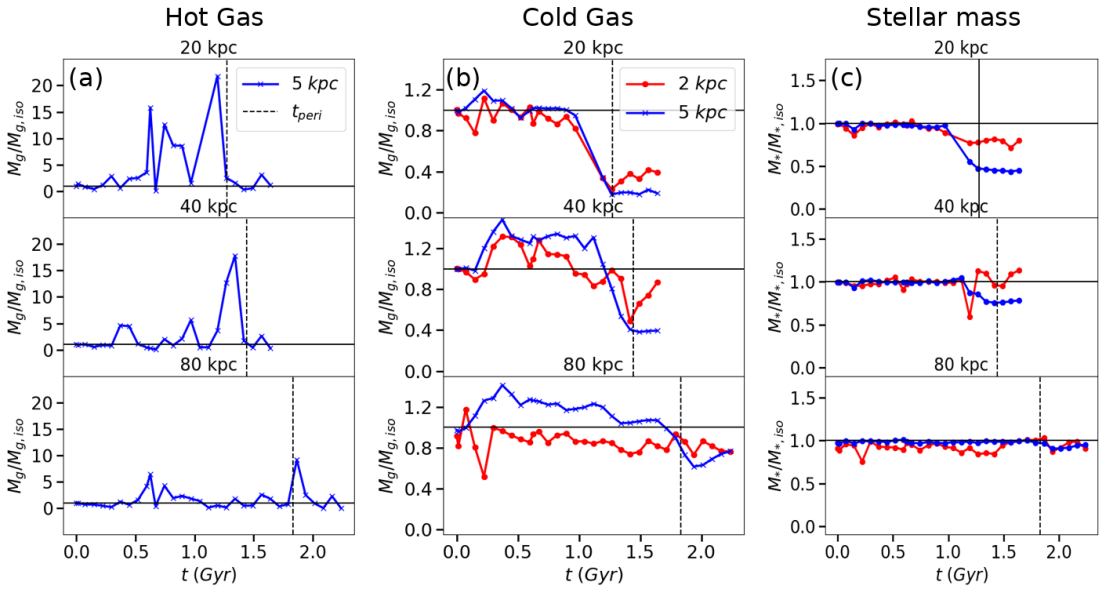

Figure 5.8: Effect of pericenter: comparison with respect to isolated simulation of dwarf galaxy of (a) mass in hot gas ($T > 10^4$ K) inside a sphere with radius of 5 kpc, (b) Mass of cold gas ($T <= 10^4$ K) and stellar mass (M_*) inside a disc with height of 1 kpc and radius of 2 kpc and 5 kpc. On decreasing the pericentric distance there is increase in hot gas, more loss of stars from stellar disc and cold gas compared to isolated galaxy simulations.

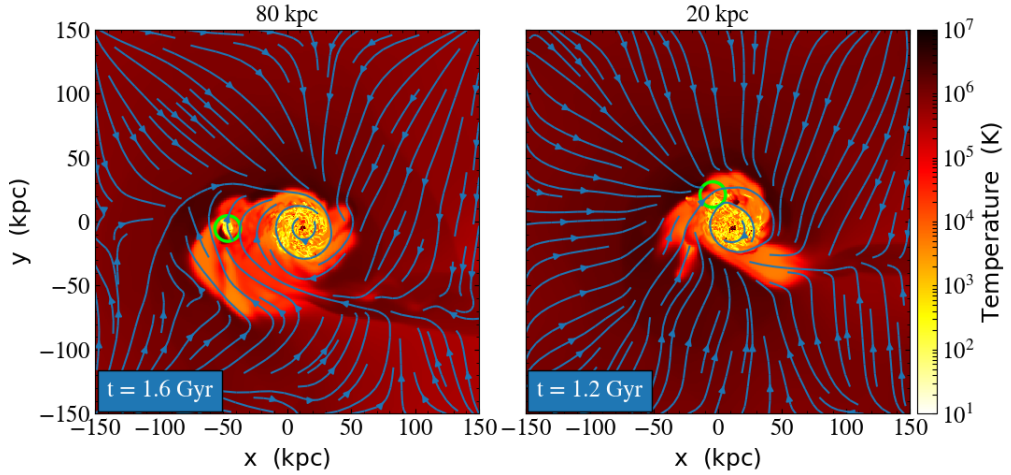

Figure 5.9: Effect of pericenter: temperature slice of the merger simulations just after the pericentric passage with the pericentric distances of 80 kpc and 20 kpc. The overplotted lines show the streamlines of the flow of gas. Position of the dwarf galaxy is denoted by the green circle. For a low pericentric distance, the cold gas from the circumgalactic medium reaches the dwarf galaxy radially and fuels the star formation around the pericenter. For larger pericentric distance, the streamlines are curled up and the gas falling towards the dwarf galaxy gets heated up.

case of larger pericentric distance, the streamlines are curled up and do not take a radial path to the dwarf galaxy. The gas falling towards the dwarf galaxy also gets heated up. This results in less efficient supply of star-forming gas; therefore, less star formation activity takes place on pericentric passage for a larger pericentric distance.

This decrease in cold gas mass observed in Figure 5.8(b), increase in cumulative stellar mass observed in Figure 5.6 and increase in hot gas mass observed in Figure 5.8(a) indicates that on approaching the pericenter, there is the formation of stars due to compression by tidal forces. From figure Figure 5.8(c) we can conclude that on decreasing pericentric distance these newly formed stars along with older stars in the disc are increasingly pulled out of the disc.

5.6.2 Effects of compactness

We model the compactness of the dwarf galaxy using the spin parameter of the dark matter halo. In case of isothermal distribution of dark matter particles, the spin parameter of galaxy dictates the gas distribution. For isothermal dark matter profile, the gas distribution in the disc has an exponential profile with disc scale radius (r_g) given by:

$$r_g = \frac{\lambda}{\sqrt{2}} r_{vir} \tag{5.12}$$

where λ is the spin parameter of the galaxy and r_{vir} is the virial radius of the dark matter halo. The distribution of gas is more compact for a galaxy with low value of spin parameter.

In Figure 5.10(top) we show the projected stellar mass for different spin parameters (λ) for a trajectory having 40 kpc pericentric distance. In all the cases the stars at in the outer disc have been stripped from the disc forming tidal tails. We observe a thick, more prominent tidal tail for the case of a higher spin parameter ($\lambda = 0.08$). In Figure 5.10(bottom) we show the projected gas density of the galaxies. There is a decreasing trend for the gas that remains in the disc with increasing spin parameter. We observe that the gas retained in the disc decreases considerably as the spin parameter increases.

In Figure 5.11 we show the cumulative stellar mass of the dwarf galaxy for different spin parameters. The initial star-burst is more pronounced in the case of a lower spin parameter ($\lambda = 0.02$). This is due to a higher concentration of gas. For higher spin parameter ($\lambda = 0.08$) the gas is distributed over a larger area. Close to the pericenter of the trajectory, there is a gradual increase in the stellar mass. This second increase of stellar mass is similar for all three spin parameters.

In Figure 5.12 we show the cold gas with temperature $T < 10^4$ K inside the disc with radius 5 kpc and 2 kpc and height of 1 kpc. There is an initial loss of gas at both the radii because of initial star formation. In the case of 5 kpc radius, the decrease in mass of the gas inside is more for the case of the higher spin parameter ($\lambda = 0.08$) after passing from the pericenter. The gas for dwarf galaxy with higher spin parameter is distributed over in a larger area and thus easily stripped by tidal forces. In all the cases we observe that gas within the distance of 2 kpc from centre remains nearly constant after pericentric passage.

The evolution of cold gas ($T <= 10^4$ K) mass inside the disc of height 1 kpc

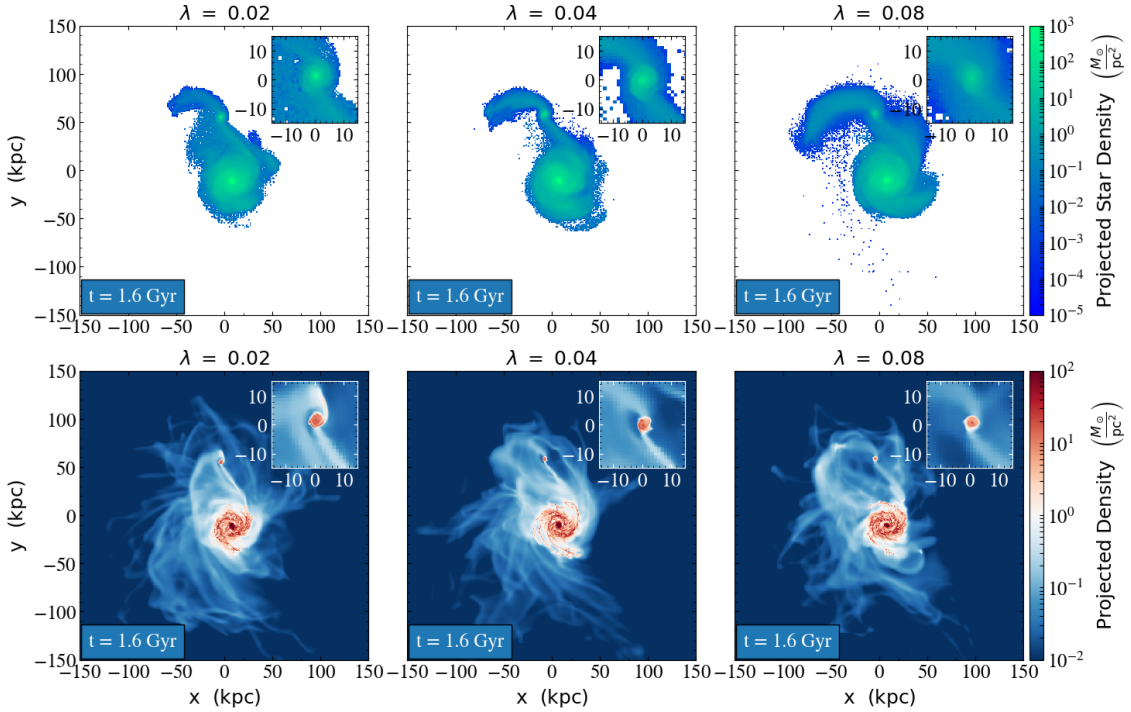

Figure 5.10: Effects of compactness: (top) stellar mass projection plot and (bottom) gas density projection plot for different compactness. The pericentric distance for all the three cases is 40 kpc.

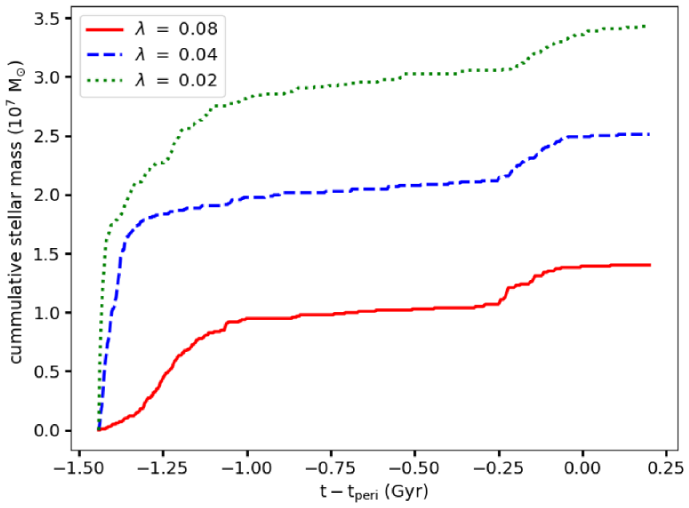

Figure 5.11: Effects of spin parameter: cummulative stellar mass of dwarf galaxy for merger simulation with different compactness. We observe a spike in stellar mass as galaxy approaches the pericenter. The spike in stellar mass is same for the three cases with spin parameters 0.02, 0.04 and 0.08.

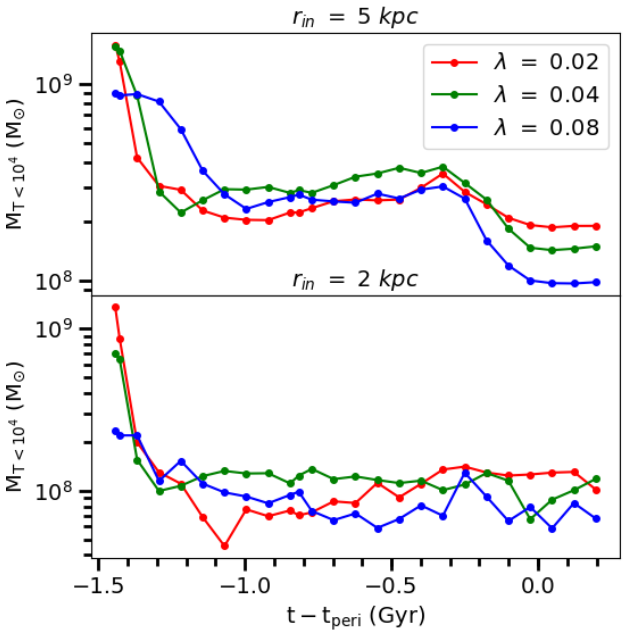

Figure 5.12: Effects of spin parameter: mass of the gas with temperature $T < 10^4$ K in disc with thickness of 2 kpc and different radius $r_{\rm in}$ of 5 kpc (top panel) and 2 kpc (bottom panel). Gas retained by the dwarf galaxy decreases for decreasing compactness (increasing λ). For a radius of 2 kpc the gas remains unaffected for all the cases.

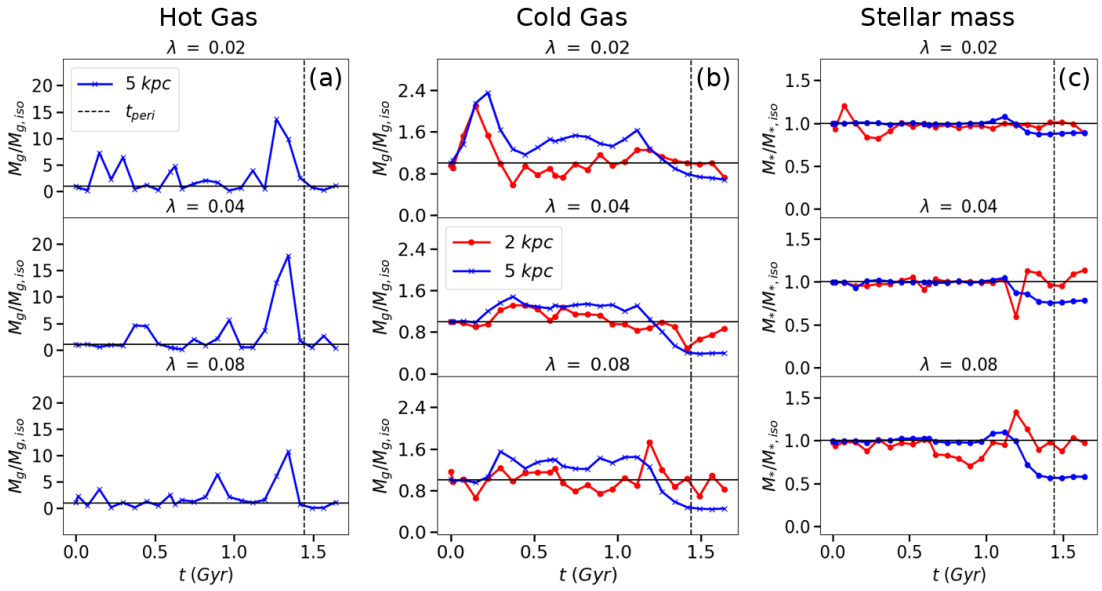

Figure 5.13: Effect of compactness: comparison with respect to isolated simulation of dwarf galaxy of (a) mass in hot gas ($T > 10^4$ K) inside a sphere with radius of 5 kpc, (b) Mass of cold gas ($T <= 10^4$ K) and stellar mass (M_*) inside a disc with height of 1 kpc and radius of 2 kpc and 5 kpc. On increasing compactness from low ($\lambda = 0.08$) to high ($\lambda = 0.02$) there is increase in hot gas, less loss of stellar mass and cold gas from the disc of dwarf galaxy compared to isolated galaxy simulations.

and radius of 2 kpc and 5 kpc is shown in Figure 5.13(b). For less compactness ($\lambda = 0.04, 0.08$), we observe a similar evolution compared to the isolated galaxy at both radii before passing from the pericenter. In case of a more compact disc ($\lambda = 0.02$) there is a significant increase in cold gas mass at both inner and outer radii with stellar mass becoming 2.5 times the isolated galaxy. In merger simulation, the more compact galaxy has more stars compared to the isolated galaxy before pericentric passage. After passing from the pericenter, we observe that the stellar mass in outer disc decreases by 20% for more compact disc ($\lambda = 0.02$) to 60% for less compact discs.

In Figure 5.13(a) we show the ratio of hot gas ($T > 10^4$ K) mass inside a sphere of radius 5 kpc for different compactness. We observe that there is no systematic difference between the hot gas mass between isolated simulation and merger simulations for all the compactness. There is a short increase in hot gas mass content before the pericentric passage. On approaching the pericenter, gas content increases by a factor of 10 for low compactness ($\lambda = 0.08$) to more than 15 in the case of high compactness ($\lambda = 0.02$).

We show in 5.13(c) ratio of stellar mass in the dwarf galaxy for isolated and merger within discs having a height of 1 kpc and a radius of 2 kpc and 5 kpc. The stellar mass in inner disc remains similar at all times to the isolated simulation. The stellar mass in the outer disc remains equal to the isolated case before passing from the pericenter. After passing from the pericenter, there is a decrease in stellar mass in outer disc ranging 40% for low compactness ($\lambda = 0.08$) to 15% in the case of high compactness ($\lambda = 0.02$).

We observed in Figure 5.11 that the increase in stellar mass on approaching the pericenter is similar for all compactness. This increase in stellar mass results in an increase in hot gas content observed in Figure 5.13(a) but this additional stellar mass produced for the decreasing cold gas mass in outer disc seen in Figure 5.13(b) is pulled from the outer disc into the tidal arms. More compact dwarf galaxy ($\lambda = 0.02$) is able to retain its stellar content in out disc more than the less compact disc ($\lambda = 0.08$).

5.6.3 Effects of gas mass

In Figure 5.14(top) we show the projected stellar mass for different mass of gas in dwarf galaxies for a trajectory having 40 kpc pericentric distance. In all the cases the stars in the outer disc have been stripped from the disc in tidal tails. We observe a thick, more prominent tidal tail for the case of the higher gas mass. In Figure 5.14(bottom) we show the projected gas density of the galaxies. There is a decreasing trend for the gas that remains in the disc with decreasing gas mass. We observe that the gas in the disc decreases considerably as the gas mass increases.

In Figure 5.15 we show the cumulative stellar mass of the dwarf galaxy for different gas masses in the disc. The initial star-burst is more in the case of high gas mass in the disc. This is due to a higher concentration of gas as denser gas cools down to form stars. Close to the pericenter of the trajectory, there is a gradual increase in the stellar mass. We observe that for the disc with more gas, the effect on cumulative stellar mass is not visible. The increase on approaching pericenter is more prominent for lower gas mass runs (0.16×10^{10} $M_\odot$ and 0.08×10^{10} $M_\odot$).

In Figure 5.16 we show the gas with temperature $T < 10^4$ K inside the disc with

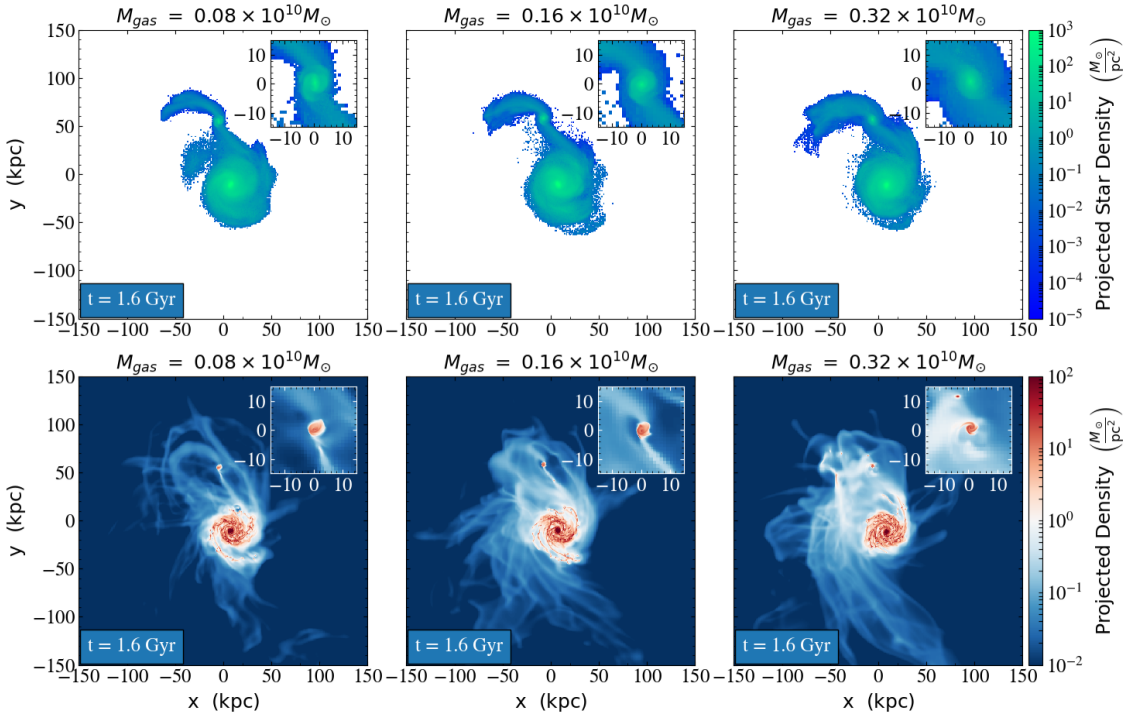

Figure 5.14: Effects of gas mass: (top) stellar mass projection plot and (bottom) gas mass projection plot for different gas masses with a trajectory having pericentric distance of 40 kpc in face-on view.

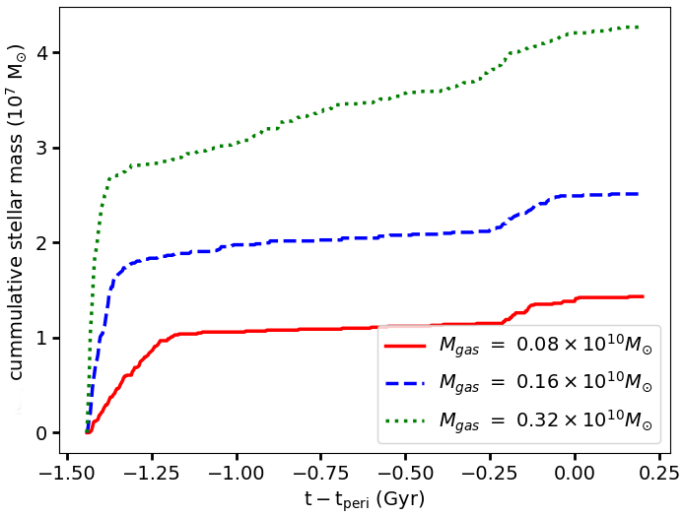

Figure 5.15: Effects of gas mass: cummulative stellar mass of dwarf galaxy for merger simulation with different gas mass in disc. We observe a very small spike in stellar mass as galaxy approaches the pericenter which decrease with increase in gas mass.

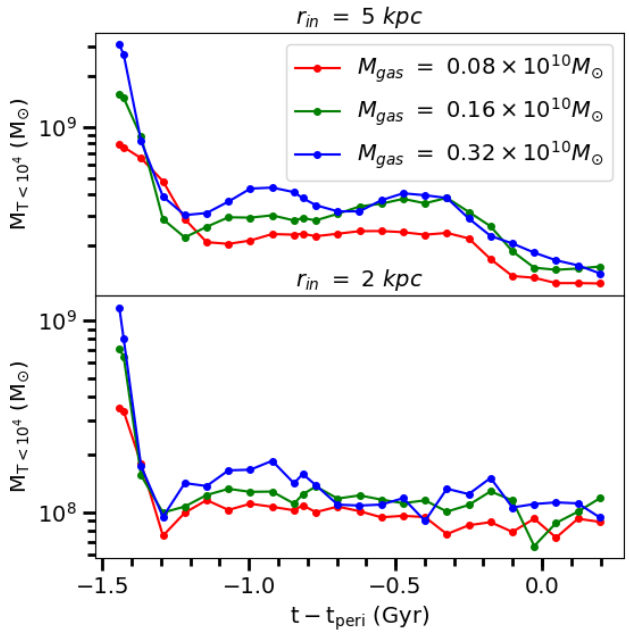

Figure 5.16: Effects of gas mass: mass of the gas with temperature $T < 10^4$ K in disc with a thickness of 2 kpc and different radius $r_{\rm in}$ of 5 kpc (top panel) and 2 kpc (bottom panel). The relative retention of gas by the dwarf galaxy is more in the case of low gas mass and decrease with increasing gas mass. For a radius of 2 kpc the gas remains unaffected for all the cases.

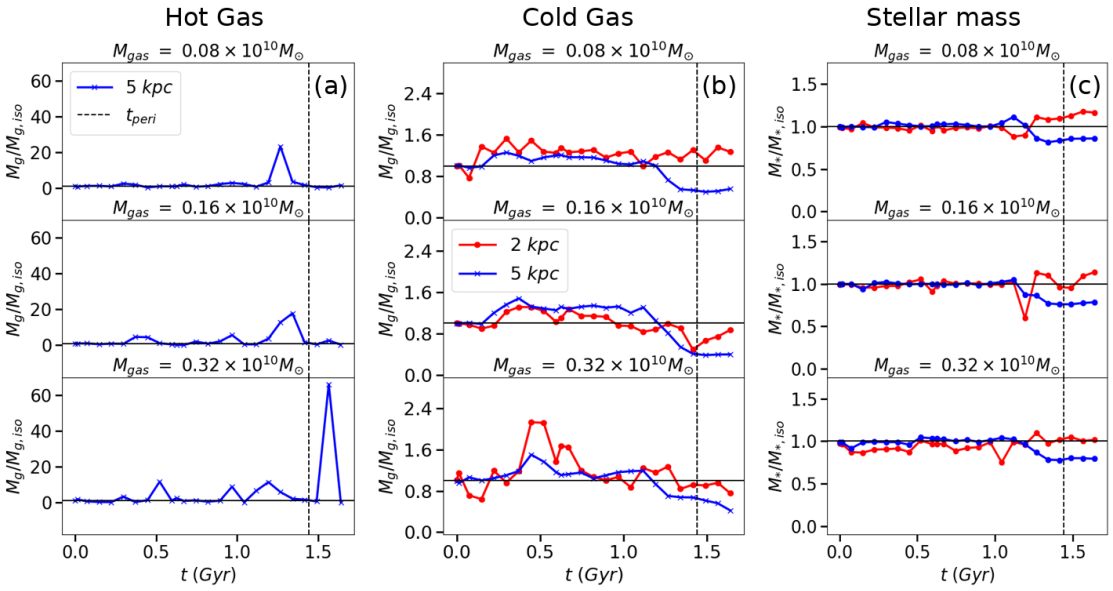

Figure 5.17: Effect of gas mass: comparison with respect to isolated simulation of dwarf galaxy of (a) mass in hot gas ($T > 10^4$ K) inside a sphere with radius of 5 kpc, (b) Mass of cold gas ($T <= 10^4$ K) and stellar mass (M_*) inside a disc with height of 1 kpc and radius of 2 kpc and 5 kpc. On increasing the initial gas mass in the disc there is increase in hot gas but similar decrease in stellar mass and cold gas on passing the pericenter compared to isolated galaxy simulations.

radius 5 kpc and 2 kpc and height of 1 kpc. In the case of 5 kpc radius, the decrease in mass of the gas inside increases with gas mass after passing from the pericenter. The relative retention of gas by the dwarf galaxy is more in the case of low gas mass and decreases as the gas in the disc increases. In all the cases we observe that gas within the distance of 2 kpc from centre remains nearly constant after pericentric passage.

In Figure 5.17(b) we show the comparative evolution of cold gas ($T <= 10^4$ K) mass inside discs with height 1 kpc and two different radii of 2 kpc and 5 kpc. We observe that before reaching the pericenter, the cold gas inside the inner radius is more compared to the isolated galaxy of similar mass. For higher gas mass this increase is double but becomes closer to the gas content in the isolated galaxy as the gas mass decreases. After reaching the pericenter, the gas in the outer part of the disc decreases significantly for all the cases with gas mass becoming nearly half of that of the isolated galaxy for all different cases of gas mass.

We study the hot gas content in the dwarf galaxy for dwarf galaxy with a different gas mass in disc. In Figure 5.17(a) shows the hot gas ($T > 10^4$ K) mass inside a sphere of radius 5 kpc. The hot gas content is similar to the isolated galaxy cases, but small increase which matches the increase in cold gas mass content of inner and out disc observed around 0.5 Gyr in 5.17(b). On reaching the pericenter, there is a huge increase in hot gas content reaching as much as 60 times. This increase correlates with the gas mass content of the disc.

We show the stellar mass evolution of dwarf galaxy in Figure 5.17(c). The stellar mass remains the same as that of isolated galaxy simulations. After reaching the pericenter, we observe a similar decrease in stellar mass for all the three cases of gas masses. The stellar mass in outer radius reduces by 20% in all the cases.

On varying the initial gas mass in the dwarf galaxy, we observe that on passing the pericenter the relative increase in star formation is the same in all the cases as shown in Figure 5.15. There is significantly more hot gas present in the dwarf galaxy on reaching pericenter in all the cases which decrease as the disc gas mass decreases, as shown in Figure 5.17(a). In all the three cases considered we observe a similar decrease in stellar mass from the outer disc of the dwarf galaxies.

5.7 Summary

In this study, we performed hydrodynamical simulations of a merger between a dwarf galaxy and a massive central galaxy. We study the effects of a merger on the dwarf galaxy in a single pericentric passage by varying various parameters related to trajectory and intrinsic parameter of the dwarf galaxy. We summarise the main results below:

- Effects of pericentric distance:
    - On approaching the pericentre there is an increase in the stellar mass. Stronger tidal forces on a decrease in the pericentric distance lead to more star formation and an eventually greater increase in stellar mass.
    - The dwarf galaxy loses gas from the outer radius of the disc on approaching the pericentre. This decrease in gas mass increases in decreasing the pericentric distance.

- Effects of compactness:
  - In the case of a highly compact disc, the initial burst of star formation produces more stars compared to the case with low compactness. The increase in stellar mass on approaching the pericenter is similar for different compactness.
  - Decrease in the mass of the gas from the outer disc of the dwarf galaxy is more in the case of low compactness ($\lambda = 0.08$) after passing from the pericenter.
- Effects of gas mass:
  - The initial star-burst produces more stars for the case with higher gas mass. On approaching the pericenter, the increase in stellar mass is similar for all the cases.
  - The relative retention of gas by the dwarf galaxy is more in the case of the low gas mass.

We observe that gas retained by the dwarf galaxy depends on the trajectory as well as the intrinsic parameters of the galaxy. With more pericentric passage the dwarf galaxy will lose most of its own gas and continue to form stars using the gas accreted from the circumgalactic medium of the central galaxy. This study indicates that a merger of a dwarf galaxy with the large massive galaxy significantly affects the star-forming capability of the dwarf galaxy.

Chapter 6

Conclusions and Future Work

In this thesis, we used a variety of tools, analytical models, multi-wavelength observations, and hydrodynamical simulations to probe the effects of the large-scale environment on galaxy properties. We focused on two processes, namely ram pressure stripping (RPS) and minor mergers to study their effects on galaxy evolution. We also focused on large-scale filament environment and studied the properties of galaxies residing in them and compare hydrodynamical simulations with observations.

In Chapter 2, we used an analytical approach to study RPS with simple models for discs and distribution of halo gas to study the phenomenon in the cluster, group, and galaxy halos. We studied variations in RPS with the properties of the in-falling galaxy and host halos. We found that gas is stripped more easily for a less compact galaxy. The variation of the initial velocity of the infalling galaxy does not matter much over the full orbit, though it does make a difference at early stages. RPS is sub-dominant in the group environment as compared to clusters and is even less important in galaxy environments.

In Chapter 3, we used the arsenal of ultraviolet and optical data for galaxies in the Coma supercluster. We identify the different components of the cosmic-web: large-scale filaments and field. We showed that the position of a galaxy in the $NUV-r$ versus r colour-magnitude space and in the $FUV-NUV$ versus $NUV-r$ colour-colour space can be used to separate star-forming galaxies from the passively-evolving galaxies in all environments. We observed that dwarf galaxies are blue except in the dense interiors of the clusters and groups. Most of the giants in all the environments are red, but their fraction decreases with the environmental density. These trends are similar for the $FUV-NUV$and $NUV-r$ colour. We observed that galaxies become redder and emission in Hα declines with their distance from the nearest maximum in density. Galaxies become redder, and the median EW(Hα) declines within a radius of 1 Mpc to the spine of the filament. We showed that this effect in $g-r$, $FUV-NUV$, and Hα emission of galaxies is statistically significant, and points to the key role played by the large-scale filaments in shaping properties of galaxies. Our analysis supports the hypothesis that properties of galaxies are not just defined by its stellar mass and large-scale density, but also by the environmental processes resulting due to the intrafilament medium whose role in accelerating galaxy transformations needs to be investigated thoroughly using multi-wavelength data.

In Chapter 4 to study the large-scale filament environment in simulations, we used Evolution and Assembly of GaLaxies and their Environment (EAGLE; Schaye

et al., 2015). We used the largest available box in the EAGLE simulation of 100 Mpc h^{-1}. Using a similar technique mentioned above, we categorised the large-scale environments and performed a stacked analysis of various mock observations. We compared and contrasted our results with the observations. We showed that galaxies become redder and more passive closer to the central axis of the filaments. This trend is observed within a radius of 2 Mpc around the spine of the filament, thus providing an upper limit for the filaments' radius, which is in agreement with the results from various observations. We found that closer to the spine of the filaments, within 0.5 Mpc, the gas and stellar mass fractions of galaxies rise. Beyond 0.5 Mpc from the spine, the SMF remains constant while the GMF rises smoothly. We concluded that these observed trends are a consequence of increased gravitational interactions between filament galaxies closer to the spine of the filament due to increase in number density of galaxies. We showed that the morphology of galaxies on filaments is similar to their counterparts in field but statistically distinct from the ones in clusters.

To study the effects of galaxy interaction on a dwarf galaxy moving in the vicinity of a Milky-way type central galaxy, we perform hydrodynamical simulation using `RAMSES` code (Teyssier, 2002b). We vary various parameters related to the properties of the dwarf galaxy and its trajectory to study the effect on the gas, which gets stripped. We showed that the stellar mass increases on approaching the pericenter and this increase is greater for decreasing pericentric distance due to stronger tidal forces. The gas in the outer parts of the dwarf galaxy decreases on approaching the pericentre. This decrease in gas mass increases by decreasing the pericentric distance. We observed that a highly compact disc produces more stars compared to the case with low compactness in initial starburst and increase in stellar mass on approaching the pericenter is similar for different compactness. For dwarf galaxy having low compactness, there is more decrease in gas outer disc after passing from pericenter. By varying initial gas mass in the disc of the dwarf galaxy, we showed that although there is more star formation in the case of higher gas mass the increase in stellar mass is similar in all the cases. We observed that the disc with initially low gas mass is relatively able to retain more gas.

We are currently working on more analysis to be done in studying the filaments in simulations and effects on the central galaxy on interaction with dwarf galaxy in galactic interaction. The work in done as part of this thesis can be extended to further explore the effects of the environment on the galaxy properties. We will use the 2D slices obtained from EAGLE simulations in Chapter 4 to get mock x-ray observations and study the properties of intrafilamentary medium. The results will help in predicting the density profile of intrafilamentary and, if any, its variation. We will be able to study the metallicity gradients along and perpendicular to the spine of the filaments in the EAGLE simulation.

In Chapter 2, we showed that the inhomogeneity in the galactic disc helps to retain the gas more compared to a homogeneous disc. We will use a hydrodynamical simulation of an isolated galaxy, performed using `RAMSES` hydrodynamical code (Teyssier, 2002b), moving in a background density distribution. We propose a semi-analytical model based on our analytical model. The results of this work will shed light on cases where ram pressure is dominant for quenching star formation in environments. If the ram pressure plays a significant role in particular environments, it will have implications for long-standing issues like the missing satellite problem.

There may be undetected galaxies which have undergone stripping at an earlier time, and our current instruments are not sensitive enough to detect them.

Bibliography

Abadi M. G., Moore B., Bower R. G., 1999, MNRAS, 308, 947

Agertz O., et al., 2007, MNRAS, 380, 963

Akamatsu H., et al., 2017, A&A, 606, A1

Alam et. al. S., 2015, The Astrophysical Journal Supplement Series, 219, 12

Allen P. D., Driver S. P., Graham A. W., Cameron E., Liske J., de Propris R., 2006, MNRAS, 371, 2

Allen R. J., Kacprzak G. G., Glazebrook K., Tran K.-V. H., Spitler L. R., Straatman C. M. S., Cowley M., Nanayakkara T., 2016, ApJ, 826, 60

Alpaslan M., et al., 2015, MNRAS, 451, 3249

Alpaslan M., et al., 2016a, MNRAS, 457, 2287

Alpaslan M., et al., 2016b, MNRAS, 457, 2287

Ann H. B., Park C., Choi Y.-Y., 2008, MNRAS, 389, 86

Astropy Collaboration Price-Whelan A. M. e. a., 2018, AJ, 156, 123

Bagla J. S., 2002, Journal of Astrophysics and Astronomy, 23, 185

Bagla J. S., Ray S., 2005, MNRAS, 358, 1076

Bagla J. S., Prasad J., Khandai N., 2009, MNRAS, 395, 918

Bahé Y. M., McCarthy I. G., 2015, MNRAS, 447, 969

Baldry I. K., Balogh M. L., Bower R. G., Glazebrook K., Nichol R. C., Bamford S. P., Budavari T., 2006, MNRAS, 373, 469

Baldwin J. A., Phillips M. M., Terlevich R., 1981, Publications of the Astronomical Society of the Pacific, 93, 5

Balogh M. L., Navarro J. F., Morris S. L., 2000, ApJ, 540, 113

Balogh M. L., Christlein D., Zabludoff A. I., Zaritsky D., 2001, ApJ, 557, 117

Balogh M., et al., 2004, MNRAS, 348, 1355

Balsara D., Livio M., O'Dea C. P., 1994, ApJ, 437, 83

Bamford S., et al., 2009, MNRAS, 393, 1324

Barnes J. E., Hernquist L., 1992, Annual Review of Astronomy and Astrophysics, 30, 705

Barnes J. E., Hernquist L., 1996, ApJ, 471, 115

Barnes J., Hut P., 1986, Natur., 324, 446

Behroozi P. S., Wechsler R. H., Conroy C., 2013, ApJ, 770, 57

Berger M. J., Oliger J., 1984, Journal of Computational Physics, 53, 484

Bergin E. A., Tafalla M., 2007, Annual Review of Astronomy and Astrophysics, 45, 339

Bernstein G. M., Nichol R. C., Tyson J. A., Ulmer M. P., Wittman D., 1995, AJ, 110, 1507

Bianchi L., Herald J., Efremova B., Girardi L., Zabot A., Marigo P., Conti A., Shiao B., 2011, Ap&SS, 335, 161

Bianchi L., Conti A., Shiao B., 2014, Advances in Space Research, 53, 900

Binggeli B., Sandage A., Tammann G. A., 1988, ARA&A, 26, 509

Binney J., Tremaine S., 2008, Galactic Dynamics: Second Edition

Bischko J. C., Steinhauser D., Schindler S., 2015, A&A, 576, A76

Biviano A., Fadda D., Durret F., Edwards L. O. V., Marleau F., 2011, A&A, 532, A77

Blitz L., Robishaw T., 2000, ApJ, 541, 675

Bond J. R., Kofman L., Pogosyan D., 1996, Natur., 380, 603

Bonjean V., Aghanim N., Salomé P., Douspis M., Beelen A., 2018, A&A, 609, A49

Bonjean V., Aghanim N., Douspis M., Malavasi N., Tanimura H., 2019, arXiv e-prints, p. arXiv:1912.06559

Bösch B., et al., 2013, A&A, 549, A142

Boselli A., et al., 2005, ApJ, 629, L29

Boselli A., et al., 2014, A&A, 570, A69

Boselli A., et al., 2016, A&A, 596, A11

Boselli A., et al., 2018, A&A, 615, A114

Boué G., Durret F., Adami C., Mamon G. A., Ilbert O., Cayatte V., 2008, A&A, 489, 11

Bournaud F., Combes F., 2004, in Combes F., Barret D., Contini T., Meynadier F., Pagani L., eds, SF2A-2004: Semaine de l'Astrophysique Francaise. p. 645

Bournaud F., Jog C. J., Combes F., 2005, A&A, 437, 69

Bouwens R. J., et al., 2009, ApJ, 705, 936

Bravo-Alfaro H., Cayatte V., van Gorkom J. H., Balkowski C., 2000, AJ, 119, 580

Brown T., et al., 2017, MNRAS, 466, 1275

Bruzual G., Charlot S., 2003, MNRAS, 344, 1000

Budavári T., et al., 2009, ApJ, 694, 1281

Bundy K., Fukugita M., Ellis R. S., Targett T. A., Belli S., Kodama T., 2009, ApJ, 697, 1369

Burstein D., Bertola F., Buson L. M., Faber S. M., Lauer T. R., 1988, ApJ, 328, 440

Butcher H., Oemler A. J., 1978a, ApJ, 219, 18

Butcher H., Oemler A. J., 1978b, ApJ, 226, 559

Campello R. J. G. B., Moulavi D., Zimek A., Sander J., 2015, ACM Trans. Knowl. Discov. Data, 10, 5:1

Cardelli J. A., Clayton G. C., Mathis J. S., 1989, ApJ, 345, 245

Carroll S. M., Press W. H., Turner E. L., 1992, Annual Review of Astronomy and Astrophysics, 30, 499

Cautun M. C., van de Weygaert R., 2011, The DTFE public software: The Delaunay Tessellation Field Estimator code (ascl:1105.003)

Cavaliere A., Fusco-Femiano R., 1976, A&A, 500, 95

Cayatte V., Kotanyi C., Balkowski C., van Gorkom J. H., 1994, AJ, 107, 1003

Cen R., Ostriker J. P., 1999, ApJ, 514, 1

Chabrier G., 2003, Publications of the Astronomical Society of the Pacific, 115, 763

Chandrasekhar S., 1943, ApJ, 97, 255

Chen Y.-C., et al., 2017, MNRAS, 466, 1880

Chengalur J. N., Braun R., Wieringa M., 2001, A&A, 372, 768

Chilingarian I. V., Zolotukhin I. Y., 2012, MNRAS, 419, 1727

Chincarini G., Rood H. J., 1976, ApJ, 206, 30

Cibinel A., et al., 2013, ApJ, 776, 72

Close J. L., Pittard J. M., Hartquist T. W., Falle S. A. E. G., 2013, MNRAS, 436, 3021

Colella P., Woodward P. R., 1984, Journal of Computational Physics, 54, 174

Coppin K. E. K., et al., 2011, MNRAS, 416, 680

Coppin K. E. K., et al., 2012, ApJ, 749, L43

Cornett R. H., et al., 1998, AJ, 116, 44

Correa C. A., Schaye J., Clauwens B., Bower R. G., Crain R. A., Schaller M., Theuns T., Thob A. C. R., 2017, MNRAS, 472, L45

Cortese L., et al., 2005, ApJ, 623, L17

Cortese L., et al., 2007, MNRAS, 376, 157

Courant R., Friedrichs K., Lewy H., 1967, IBM Journal of Research and Development, 11, 215

Cowie L. L., Songaila A., 1977, Natur., 266, 501

Cox T. J., Dutta S. N., Di Matteo T., Hernquist L., Hopkins P. F., Robertson B., Springel V., 2006, ApJ, 650, 791

Crain R. A., et al., 2015, MNRAS, 450, 1937

Cresci G., Mannucci F., Curti M., 2019, A&A, 627, A42

Croft R. A. C., Di Matteo T., Davé R., Hernquist L., Katz N., Fardal M. A., Weinberg D. H., 2001, ApJ, 557, 67

Crone Odekon M., Hallenbeck G., Haynes M. P., Koopmann R. A., Phi A., Wolfe P.-F., 2018, ApJ, 852, 142

Cybulski R., Yun M. S., Fazio G. G., Gutermuth R. A., 2014, MNRAS, 439, 3564

Dalla Vecchia C., Schaye J., 2012, MNRAS, 426, 140

Darvish B., Sobral D., Mobasher B., Scoville N. Z., Best P., Sales L. V., Smail I., 2014, ApJ, 796, 51

Darvish B., Mobasher B., Sobral D., Hemmati S., Nayyeri H., Shivaei I., 2015, ApJ, 814, 84

De Rossi M. E., Bower R. G., Font A. S., Schaye J., Theuns T., 2017a, MNRAS, 472, 3354

De Rossi M. E., Bower R. G., Font A. S., Schaye J., Theuns T., 2017b, MNRAS, 472, 3354

Di Matteo P., Lehnert M. D., Qu Y., van Driel W., 2011, A&A, 525, L3

Dietrich J. P., Werner N., Clowe D., Finoguenov A., Kitching T., Miller L., Simionescu A., 2012, Natur., 487, 202

Doi M., et al., 2010, AJ, 139, 1628

Dolag K., Meneghetti M., Moscardini L., Rasia E., Bonaldi A., 2006, MNRAS, 370, 656

Dolag K., Borgani S., Murante G., Springel V., 2009, MNRAS, 399, 497

Donas J., Buat V., Milliard B., Laget M., 1990, A&A, 235, 60

Donas J., Milliard B., Laget M., 1995, A&A, 303, 661

Donoso E., O'Mill A., Lambas D. G., 2006, MNRAS, 369, 479

Dressler A., 1980, ApJ, 236, 351

Dressler A., et al., 1997, ApJ, 490, 577

Dubois Y., Teyssier R., 2008, A&A, 477, 79

Duffy A. R., Schaye J., Kay S. T., Dalla Vecchia C., 2008, MNRAS, 390, L64

Eckert D., et al., 2015, Natur., 528, 105

Edwards L. O. V., Fadda D., Frayer D. T., Lima Neto G. B., Durret F., 2010a, AJ, 140, 1891

Edwards L. O. V., Fadda D., Frayer D. T., 2010b, ApJ, 724, L143

Einasto J., Klypin A. A., Saar E., Shandarin S. F., 1984, MNRAS, 206, 529

Ellingson E., Lin H., Yee H. K. C., Carlberg R. G., 2001, ApJ, 547, 609

Erfanianfar et. al. 2014, MNRAS, 445, 2725

Ester M., Kriegel H.-P., Sander J., Xu X., 1996, in Proceedings of the Second International Conference on Knowledge Discovery and Data Mining. KDD'96. AAAI Press, pp 226–231, http://dl.acm.org/citation.cfm?id=3001460.3001507

Fadda D., Biviano A., Marleau F. R., Storrie-Lombardi L. J., Durret F., 2008a, ApJ, 672, L9

Fadda D., Biviano A., Marleau F. R., Storrie-Lombardi L. J., Durret F., 2008b, ApJL, 672, L9

Fakhouri O., Ma C.-P., 2009, MNRAS, 394, 1825

Fall S. M., Efstathiou G., 1980, MNRAS, 193, 189

Fillingham S. P., Cooper M. C., Pace A. B., Boylan-Kolchin M., Bullock J. S., Garrison-Kimmel S., Wheeler C., 2016, MNRAS, 463, 1916

Fontanelli P., 1984, A&A, 138, 85

Forman W., Kellogg E., Gursky H., Tananbaum H., Giacconi R., 1972, ApJ, 178, 309

Fraser-McKelvie A., Pimbblet K. A., Lazendic J. S., 2011, MNRAS, 415, 1961

Fromang S., Hennebelle P., Teyssier R., 2006, A&A, 457, 371

Fryxell B., et al., 2000, The Astrophysical Journal Supplement Series, 131, 273

Fukugita M., Peebles P. J. E., 2004, ApJ, 616, 643

Furlong M., et al., 2015, MNRAS, 450, 4486

Gallazzi A., et al., 2009, ApJ, 690, 1883

Garnett D. R., 2002, ApJ, 581, 1019

Gavazzi G., Boselli A., Cortese L., Arosio I., Gallazzi A., Pedotti P., Carrasco L., 2006, A&A, 446, 839

Gavazzi G., Fumagalli M., Cucciati O., Boselli A., 2010, A&A, 517, A73

Gavazzi G., et al., 2013, A&A, 553, A90

Gavazzi G., Consolandi G., Gutierrez M. L., Boselli A., Yoshida M., 2018, A&A, 618, A130

Gay C., Pichon C., Le Borgne D., Teyssier R., Sousbie T., Devriendt J., 2010, MNRAS, 404, 1801

Geach J. E., Ellis R. S., Smail I., Rawle T. D., Moran S. M., 2011, MNRAS, 413, 177

Génova-Santos R., Atrio-Barandela F., Kitaura F. S., Mücket J. P., 2015, ApJ, 806, 113

Gerritsen J. P. E., 1997, PhD thesis, -

Gheller C., Vazza F., Brüggen M., Alpaslan M., Holwerda B. W., Hopkins A. M., Liske J., 2016, MNRAS, 462, 448

Gil de Paz A., et al., 2007, The Astrophysical Journal Supplement Series, 173, 185

Giovanelli R., Haynes M. P., 1983, AJ, 88, 881

Giovanelli R., et al., 2005, AJ, 130, 2598

Gisler G. R., 1976, A&A, 51, 137

Godunov S., 1959, Math. Sbornik, 47 (89), 271

Gómez P. L., et al., 2003a, ApJ, 584, 210

Gómez P. L., et al., 2003b, ApJ, 584, 210

González R. E., Padilla N. D., 2009, MNRAS, 397, 1498

Goto M., Stecklum B., Linz H., Feldt M., Henning T., Pascucci I., Usuda T., 2006, ApJ, 649, 299

Gottlöber S., Klypin A., Kravtsov A. V., 2001a, Progress in Astronomy, 19, 58

Gottlöber S., Klypin A., Kravtsov A. V., 2001b, ApJ, 546, 223

Gregory S. A., Thompson L. A., 1978, ApJ, 222, 784

Guillet T., Teyssier R., 2011, Journal of Computational Physics, 230, 4756

Gunn J. E., Gott J. Richard I., 1972, ApJ, 176, 1

Guo Q., Tempel E., Libeskind N. I., 2015, ApJ, 800, 112

Haardt F., Madau P., 1996a, ApJ, 461, 20

Haardt F., Madau P., 1996b, ApJ, 461, 20

Haardt F., Madau P., 2001, in Neumann D. M., Tran J. T. V., eds, Clusters of Galaxies and the High Redshift Universe Observed in X-rays. p. 64 (arXiv:astro-ph/0106018)

Hahn C., Tinker J. L., Wetzel A., 2017, ApJ, 841, 6

Haines C. P., La Barbera F., Mercurio A., Merluzzi P., Busarello G., 2006, ApJL, 647, L21

Haines C. P., Gargiulo A., La Barbera F., Mercurio A., Merluzzi P., Busarello G., 2007, MNRAS, 381, 7

Haines C. P., Gargiulo A., Merluzzi P., 2008, MNRAS, 385, 1201

Haines C. P., Busarello G., Merluzzi P., Smith R. J., Raychaudhury S., Mercurio A., Smith G. P., 2011a, MNRAS, 412, 145

Haines C. P., Busarello G., Merluzzi P., Smith R. J., Raychaudhury S., Mercurio A., Smith G. P., 2011b, MNRAS, 412, 145

Hammer D., Hornschemeier A. E., Mobasher B., Miller N., Smith R., Arnouts S., Milliard B., Jenkins L., 2010, The Astrophysical Journal Supplement Series, 190, 43

Hammer D. M., Hornschemeier A. E., Salim S., Smith R., Jenkins L., Mobasher B., Miller N., Ferguson H., 2012, ApJ, 745, 177

Hansen S. M., Sheldon E. S., Wechsler R. H., Koester B. P., 2009, ApJ, 699, 1333

Harrison E. R., 1970, PhRvD, 1, 2726

Hennig et. al. 2017, MNRAS, 467, 4015

Hernquist L., Katz N., 1989, The Astrophysical Journal Supplement Series, 70, 419

Hernquist L., Mihos J. C., 1995, ApJ, 448, 41

Hester J. A., 2006, ApJ, 647, 910

Hewett P. C., Warren S. J., Leggett S. K., Hodgkin S. T., 2006, MNRAS, 367, 454

Heyer M. H., Terebey S., 1998, ApJ, 502, 265

Hicks A. K., Mushotzky R., 2005, ApJ, 635, L9

Hilbert D., 1891, Mathematische Annalen, 38, 459

Hockney R. W., Eastwood J. W., 1981, Computer Simulation Using Particles

Hogg D. W., et al., 2003, ApJ, 585, L5

Hogg D. W., et al., 2004, ApJ, 601, L29

Holmberg E., 1969, Arkiv for Astronomi, 5, 305

Hopkins A. M., 2004, ApJ, 615, 209

Hopkins P. F., Hernquist L., Cox T. J., Di Matteo T., Robertson B., Springel V., 2006, The Astrophysical Journal Supplement Series, 163, 1

Hopkins P. F., Hernquist L., Cox T. J., Kereš D., 2008, ApJS, 175, 356

Hopkins P. F., Cox T. J., Younger J. D., Hernquist L., 2009, ApJ, 691, 1168

Horii T., Asaba S., Hasegawa K., Tashiro H., 2017, Publications of the Astronomical Society of Japan, 69, 73

Hubble E. P., 1936, Realm of the Nebulae

Hughes T. M., Cortese L., Boselli A., Gavazzi G., Davies J. I., 2013, A&A, 550, A115

Humason M. L., 1936, ApJ, 83, 10

Ishiyama T., Fukushige T., Makino J., 2009, Publications of the Astronomical Society of Japan, 61, 1319

J. G. B. Campello R., Moulavi D., Zimek A., Sander J., 2013, Data Mining and Knowledge Discovery, 27

Jaffé Y. L., et al., 2018, MNRAS, 476, 4753

Jauzac M., et al., 2012, MNRAS, 426, 3369

Jones D. H., et al., 2009, MNRAS, 399, 683

Kampczyk et. al. 2013, ApJ, 762, 43

Kapferer W., Kronberger T., Ferrari C., Riser T., Schindler S., 2008, MNRAS, 389, 1405

Kapferer W., et al., 2009, A&A, 504, 719

Kauffmann G., Haehnelt M., 2000, MNRAS, 311, 576

Kauffmann G., et al., 2003, MNRAS, 341, 54

Kauffmann G., White S. D. M., Heckman T. M., Ménard B., Brinchmann J., Charlot S., Tremonti C., Brinkmann J., 2004, MNRAS, 353, 713

Kenney J. D. P., Koopmann R. A., 1999a, AJ, 117, 181

Kenney J. D. P., Koopmann R. A., 1999b, AJ, 117, 181

Kenney J. D. P., van Gorkom J. H., Vollmer B., 2004a, AJ, 127, 3361

Kenney J. D. P., Crowl H., van Gorkom J., Vollmer B., 2004b, in Duc P.-A., Braine J., Brinks E., eds, IAU Symposium Vol. 217, Recycling Intergalactic and Interstellar Matter. p. 370 (arXiv:astro-ph/0403129)

Kennicutt Robert C. J., 1989, ApJ, 344, 685

Kennicutt Robert C. J., 1998a, ApJ, 498, 541

Kennicutt Robert C. J., 1998b, ApJ, 498, 541

Kewley L. J., Dopita M. A., Sutherland R. S., Heisler C. A., Trevena J., 2001, ApJ, 556, 121

Kewley L. J., Geller M. J., Barton E. J., 2006, AJ, 131, 2004

Khandai N., Bagla J. S., 2009, Research in Astronomy and Astrophysics, 9, 861

Khokhlov A., 1998, Journal of Computational Physics, 143, 519

Kim K. T., Kronberg P. P., Giovannini G., Venturi T., 1989, Natur., 341, 720

Kim S., et al., 2016, ApJ, 833, 207

Kimm T., et al., 2009, MNRAS, 394, 1131

King I., 1962, AJ, 67, 471

Kleiner D., Pimbblet K. A., Jones D. H., Koribalski B. S., Serra P., 2017, MNRAS, 466, 4692

Koopmann R. A., Haynes M. P., Catinella B., 2006, AJ, 131, 716

Köppen J., Jáchym P., Taylor R., Palouš J., 2018, MNRAS, 479, 4367

Kormendy J., Kennicutt Robert C. J., 2004, ARA&A, 42, 603

Kraljic K., et al., 2018, MNRAS, 474, 547

Kravtsov A. V., Klypin A. A., Khokhlov A. M., 1997, The Astrophysical Journal Supplement Series, 111, 73

Kroupa P., 2001, MNRAS, 322, 231

Kruskal W. H., Wallis W. A., 1952, Journal of the American Statistical Association, 47, 583

Kuutma T., Tamm A., Tempel E., 2017, A&A, 600, L6

Lah P., et al., 2009, MNRAS, 399, 1447

Laigle C., et al., 2018a, MNRAS, 474, 5437

Laigle C., et al., 2018b, MNRAS, 474, 5437

Lambas D. G., Groth E. J., Peebles P. J. E., 1988, AJ, 95, 996

Larson R. B., Tinsley B. M., 1978, ApJ, 219, 46

Larson R. B., Tinsley B. M., Caldwell C. N., 1980a, ApJ, 237, 692

Larson R. B., Tinsley B. M., Caldwell C. N., 1980b, ApJ, 237, 692

Lee H., Skillman E. D., Cannon J. M., Jackson D. C., Gehrz R. D., Polomski E. F., Woodward C. E., 2006, ApJ, 647, 970

Lequeux J., Peimbert M., Rayo J. F., Serrano A., Torres-Peimbert S., 1979, A&A, 500, 145

Leroy A. K., Walter F., Brinks E., Bigiel F., de Blok W. J. G., Madore B., Thornley M. D., 2008, AJ, 136, 2782

Lewis I., et al., 2002, MNRAS, 334, 673

Liao S., Gao L., 2019, MNRAS, 485, 464

Libeskind N. I., et al., 2018, MNRAS, 473, 1195

Lin Y.-T., Mohr J. J., Stanford S. A., 2004, ApJ, 610, 745

Lin Y.-T., et al., 2017, ApJ, 851, 139

Luber N., van Gorkom J. H., Hess K. M., Pisano D. J., Fernández X., Momjian E., 2019, AJ, 157, 254

Luo Y., Kang X., Kauffmann G., Fu J., 2016, MNRAS, 458, 366

Madau P., Pozzetti L., Dickinson M., 1998, ApJ, 498, 106

Mahajan S., 2013, MNRAS, 431, L117

Mahajan S., Haines C. P., Raychaudhury S., 2010, MNRAS, 404, 1745

Mahajan S., Haines C. P., Raychaudhury S., 2011, MNRAS, 412, 1098

Mahajan S., Raychaudhury S., Pimbblet K. A., 2012a, MNRAS, 427, 1252

Mahajan S., Raychaudhury S., Pimbblet K. A., 2012b, MNRAS, 427, 1252

Mahajan S., Singh A., Shobhana D., 2018, MNRAS, 478, 4336

Malavasi N., et al., 2017, MNRAS, 465, 3817

Mannucci F., Cresci G., Maiolino R., Marconi A., Gnerucci A., 2010, MNRAS, 408, 2115

Marcolini A., Brighenti F., D'Ercole A., 2003, MNRAS, 345, 1329

Martin D. C., et al., 2005, ApJ, 619, L1

Martin G., Kaviraj S., Devriendt J. E. G., Dubois Y., Pichon C., 2018, MNRAS, 480, 2266

Martínez H. J., Muriel H., Coenda V., 2016, MNRAS, 455, 127

Martizzi D., et al., 2018, arXiv e-prints, p. arXiv:1810.01883

McAlpine S., et al., 2016, Astronomy and Computing, 15, 72

McClure R. D., van den Bergh S., 1968, AJ, 73, 1008

McInnes L., Healy J., Astels S., 2017, The Journal of Open Source Software, 2, 205

Mesa V., Duplancic F., Alonso S., Muñoz Jofré M. R., Coldwell G., Lambas D. G., 2018, A&A, 619, A24

Mihos J. C., Hernquist L., 1996, ApJ, 464, 641

Mo H., van den Bosch F. C., White S., 2010a, Galaxy Formation and Evolution

Mo H., van den Bosch F., White S., 2010b, Galaxy Formation and Evolution. Galaxy Formation and Evolution, Cambridge University Press, https://books.google.co.in/books?id=Zj7fDU3Z4wsC

Mobasher B., et al., 2003, ApJ, 587, 605

Monaghan J. J., Lattanzio J. C., 1985, A&A, 149, 135

Moore B., Katz N., Lake G., Dressler A., Oemler A., 1996, Natur., 379, 613

Moore B., Lake G., Katz N., 1998, ApJ, 495, 139

Muldrew S. I., et al., 2012, MNRAS, 419, 2670

Murray N., 2011, ApJ, 729, 133

Naab T., Burkert A., 2003, ApJ, 597, 893

Navarro J. F., Frenk C. S., White S. D. M., 1996, ApJ, 462, 563

O'Connell R. W., 1999, Annual Review of Astronomy and Astrophysics, 37, 603

O'Shea B. W., Bryan G., Bordner J., Norman M. L., Abel T., Harkness R., Kritsuk A., 2004, arXiv e-prints, pp astro–ph/0403044

Oemler Augustus J., 1974, ApJ, 194, 1

Ota N., Mitsuda K., 2002, ApJ, 567, L23

Pacaud et. al. 2016, A&A, 592, A2

Parekh V., Durret F., Padmanabh P., Pandge M. B., 2017, MNRAS, 470, 3742

Park C., Hwang H. S., 2009, ApJ, 699, 1595

Pasquali A., Smith R., Gallazzi A., De Lucia G., Zibetti S., Hirschmann M., Yi S. K., 2019, MNRAS, 484, 1702

Peano G., 1890, Mathematische Annalen, 36, 157

Peebles P. J. E., 1974, ApJ, 189, L51

Peebles P. J. E., 1980, The large-scale structure of the universe

Peebles P. J. E., 1993, Principles of Physical Cosmology

Peng Y.-j., Lilly S. J., Renzini A., Carollo M., 2012, ApJ, 757, 4

Perret V., 2016, DICE: Disk Initial Conditions Environment, Astrophysics Source Code Library (ascl:1607.002)

Perret V., Renaud F., Epinat B., Amram P., Bournaud F., Contini T., Teyssier R., Lambert J. C., 2014, A&A, 562, A1

Persic M., Salucci P., 1992, MNRAS, 258, 14P

Planck Collaboration 2016, A&A, 594, A1

Planck Collaboration et al., 2014, A&A, 571, A16

Poggianti B. M., et al., 2001, ApJ, 562, 689

Porter S. C., Raychaudhury S., 2007a, MNRAS, 375, 1409

Porter S. C., Raychaudhury S., 2007b, MNRAS, 375, 1409

Porter S. C., Raychaudhury S., Pimbblet K. A., Drinkwater M. J., 2008a, MNRAS, 388, 1152

Porter S. C., Raychaudhury S., Pimbblet K. A., Drinkwater M. J., 2008b, MNRAS, 388, 1152

Postman M., Geller M. J., 1984, ApJ, 281, 95

Quilis V., Moore B., Bower R., 2000, Science, 288, 1617

Quinn P. J., Hernquist L., Fullagar D. P., 1993, ApJ, 403, 74

Rasera Y., Teyssier R., Sizun P., Cassé M., Fayet P., Cordier B., Paul J., 2006, PhRvD, 73, 103518

Rines K., Geller M. J., Kurtz M. J., Diaferio A., 2005, AJ, 130, 1482

Rodriguez-Gomez V., et al., 2017, MNRAS, 467, 3083

Roe P. L., 1986, Annual Review of Fluid Mechanics, 18, 337

Roediger E., Brüggen M., 2007, MNRAS, 380, 1399

Roediger E., Hensler G., 2005, A&A, 433, 875

Rosdahl J., Schaye J., Dubois Y., Kimm T., Teyssier R., 2017a, MNRAS, 466, 11

Rosdahl J., Schaye J., Dubois Y., Kimm T., Teyssier R., 2017b, MNRAS, 466, 11

Roškar R., Teyssier R., Agertz O., Wetzstein M., Moore B., 2014, MNRAS, 444, 2837

Salpeter E. E., 1955, ApJ, 121, 161

Sarazin C. L., 1986, Reviews of Modern Physics, 58, 1

Schaap W. E., van de Weygaert R., 2000, A&A, 363, L29

Schawinski K., et al., 2007, The Astrophysical Journal Supplement Series, 173, 512

Schaye J., 2004, ApJ, 609, 667

Schaye J., Dalla Vecchia C., 2008, MNRAS, 383, 1210

Schaye J., et al., 2015, MNRAS, 446, 521

Schlegel D. J., Finkbeiner D. P., Davis M., 1998, ApJ, 500, 525

Schmidt M., 1959, ApJ, 129, 243

Schubert E., Sander J., Ester M., Kriegel H.-P., Xu X., 2017, ACM Trans. Database Syst., 42, 19:1

Schulz S., Struck C., 2001, MNRAS, 328, 185

Scott D., 2015, Multivariate Density Estimation: Theory, Practice, and Visualization. Wiley Series in Probability and Statistics, Wiley, https://books.google.co.in/books?id=pIAZBwAAQBAJ

Scoville N., et al., 2007, ApJS, 172, 1

Sharma P., McCourt M., Parrish I. J., Quataert E., 2012, MNRAS, 427, 1219

Shull J. M., Smith B. D., Danforth C. W., 2012, ApJ, 759, 23

Simpson C. M., Grand R. J. J., Gómez F. A., Marinacci F., Pakmor R., Springel V., Campbell D. J. R., Frenk C. S., 2018, MNRAS, 478, 548

Smith R. J., et al., 2010, MNRAS, 408, 1417

Smith R. J., Lucey J. R., Price J., Hudson M. J., Phillipps S., 2012, MNRAS, 419, 3167

Sobral D., Stroe A., Dawson W. A., Wittman D., Jee M. J., Röttgering H., van Weeren R. J., Brüggen M., 2015, MNRAS, 450, 630

Solanes J. M., Manrique A., García-Gómez C., González-Casado G., Giovanelli R., Haynes M. P., 2001, ApJ, 548, 97

Somerville R. S., Davé R., 2015, ARA&A, 53, 51

Sousbie T., 2011, MNRAS, 414, 350

Sousbie T., Pichon C., Kawahara H., 2011, MNRAS, 414, 384

Sousbieb T., 2011, MNRAS, 414, 350

Spitzer Lyman J., 1958, ApJ, 127, 17

Springel V., 2005, MNRAS, 364, 1105

Springel V., Hernquist L., 2003, MNRAS, 339, 289

Springel V., White S. D. M., Tormen G., Kauffmann G., 2001, MNRAS, 328, 726

Springel V., Di Matteo T., Hernquist L., 2005, MNRAS, 361, 776

Staveley-Smith L., Koribalski B. S., Stewart I., Putman M. E., Kilborn V. A., Webster R. L., 2000, in Mangum J. G., Radford S. J. E., eds, Astronomical Society of the Pacific Conference Series Vol. 217, Imaging at Radio through Submillimeter Wavelengths. p. 50

Stewart K. R., Bullock J. S., Wechsler R. H., Maller A. H., 2009, ApJ, 702, 307

Stinson G., Seth A., Katz N., Wadsley J., Governato F., Quinn T., 2006, MNRAS, 373, 1074

Strateva et. al. I., et al., 2001, AJ, 122, 1861

Stroe A., et al., 2015, MNRAS, 450, 646

Sun M., Donahue M., Roediger E., Nulsen P. E. J., Voit G. M., Sarazin C., Forman W., Jones C., 2010, ApJ, 708, 946

Tanimura H., et al., 2019, MNRAS, 483, 223

Tejos N., et al., 2016, MNRAS, 455, 2662

Tempel E., Stoica R. S., Martínez V. J., Liivamägi L. J., Castellan G., Saar E., 2014, MNRAS, 438, 3465

Teyssier R., 2002a, A&A, 385, 337

Teyssier R., 2002b, A&A, 385, 337

Teyssier R., Pontzen A., Dubois Y., Read J. I., 2013, MNRAS, 429, 3068

Thacker R. J., Couchman H. M. P., 2000, ApJ, 545, 728

Thob A. C. R., et al., 2019, MNRAS, 485, 972

Tinker J. L., Leauthaud A., Bundy K., George M. R., Behroozi P., Massey R., Rhodes J., Wechsler R. H., 2013, ApJ, 778, 93

Tiwari J., Mahajan S., Singh K. P., 2020, arXiv e-prints, p. arXiv:2005.02757

Tonnesen S., Bryan G. L., 2009, ApJ, 694, 789

Tonnesen S., Bryan G. L., van Gorkom J. H., 2007, ApJ, 671, 1434

Toomre A., Toomre J., 1972, ApJ, 178, 623

Tran K.-V. H., Saintonge A., Moustakas J., Bai L., Gonzalez A. H., Holden B. P., Zaritsky D., Kautsch S. J., 2009, ApJ, 705, 809

Trayford J. W., et al., 2015, MNRAS, 452, 2879

Trayford J. W., Theuns T., Bower R. G., Crain R. A., Lagos C. d. P., Schaller M., Schaye J., 2016, MNRAS, 460, 3925

Tremaine S., Weinberg M. D., 1984, MNRAS, 209, 729

Tremonti C. A., et al., 2004, ApJ, 613, 898

Treyer M., et al., 2018, MNRAS, 477, 2684

Truelove J. K., Klein R. I., McKee C. F., Holliman John H. I., Howell L. H., Greenough J. A., 1997, ApJL, 489, L179

Van Waerbeke L., Hinshaw G., Murray N., 2014, PhRvD, 89, 023508

Verdugo M., Ziegler B. L., Gerken B., 2008, A&A, 486, 9

Verdugo M., Lerchster M., Böhringer H., Hildebrand t H., Ziegler B. L., Erben T., Finoguenov A., Chon G., 2012, MNRAS, 421, 1949

Villalobos Á., Helmi A., 2008, MNRAS, 391, 1806

Villalobos Á., Helmi A., 2009, MNRAS, 399, 166

Villalobos Á., Kazantzidis S., Helmi A., 2010, ApJ, 718, 314

Vollmer B., Cayatte V., Balkowski C., Duschl W. J., 2001, ApJ, 561, 708

Vollmer B., Balkowski C., Cayatte V., van Driel W., Huchtmeier W., 2004, A&A, 419, 35

Vulcani B., et al., 2019, MNRAS, 487, 2278

Wang Q. D., Owen F., Ledlow M., 2004, ApJ, 611, 821

Weinberg M. D., 1986, ApJ, 300, 93

Weinberg M. D., 1989, MNRAS, 239, 549

Weinberg M. D., 2014, MNRAS, 438, 3007

Weinmann S. M., van den Bosch F. C., Yang X., Mo H. J., 2006a, MNRAS, 366, 2

Weinmann S. M., van den Bosch F. C., Yang X., Mo H. J., 2006b, MNRAS, 366, 2

Weinmann S. M., Kauffmann G., van den Bosch F. C., Pasquali A., McIntosh D. H., Mo H., Yang X., Guo Y., 2009, MNRAS, 394, 1213

Welch B. L., 1947, Biometrika, 34, 28

Wen Z. L., Han J. L., 2018, MNRAS, 481, 4158

Werner N., Finoguenov A., Kaastra J. S., Simionescu A., Dietrich J. P., Vink J., Böhringer H., 2008, A&A, 482, L29

Wetzel A. R., Tinker J. L., Conroy C., 2012, MNRAS, 424, 232

White S. D. M., Frenk C. S., 1991, ApJ, 379, 52

White S. D. M., Rees M. J., 1978, MNRAS, 183, 341

Wiersma R. P. C., Schaye J., Smith B. D., 2009a, MNRAS, 393, 99

Wiersma R. P. C., Schaye J., Theuns T., Dalla Vecchia C., Tornatore L., 2009b, MNRAS, 399, 574

Woo J., Carollo C. M., Faber S. M., Dekel A., Tacchella S., 2017, MNRAS, 464, 1077

Wright E. L., et al., 2010, AJ, 140, 1868

Wyder T. K., et al., 2007, The Astrophysical Journal Supplement Series, 173, 293

Yıldırım A., van den Bosch R. C. E., van de Ven G., Martín-Navarro I., Walsh J. L., Husemann B., Gültekin K., Gebhardt K., 2017, MNRAS, 468, 4216

Zabludoff A. I., Mulchaey J. S., 1998, ApJ, 496, 39

Zel'Dovich Y. B., 1970, A&A, 500, 13

Zeldovich I. B., Einasto J., Shandarin S. F., 1982, Natur., 300, 407

Zhang Y., Dietrich J. P., McKay T. A., Sheldon E. S., Nguyen A. T. Q., 2013, ApJ, 773, 115

Ziegler U., 2005, A&A, 435, 385

Zinger E., Dekel A., Kravtsov A. V., Nagai D., 2018, MNRAS, 475, 3654

Zwicky F., 1938, Publications of the Astronomical Society of the Pacific, 50, 218

Zwicky F., 1951, Publications of the Astronomical Society of the Pacific, 63, 61

de Avillez M. A., Breitschwerdt D., 2007, ApJ, 665, L35

de Vaucouleurs G., 1959, Handbuch der Physik, 53, 275

van Leer B., 1979, Journal of Computational Physics, 32, 101

van der Wel A., Bell E. F., Holden B. P., Skibba R. A., Rix H.-W., 2010, ApJ, 714, 1779

von der Linden A., Wild V., Kauffmann G., White S. D. M., Weinmann S., 2010, MNRAS, 404, 1231